The Mass Distribution of Protostellar and Starless Cores in Gould Belt Clouds

by

Sarah I. Sadavoy
B.Sc., York University, 2007

A Dissertation Submitted in Partial Fulfillment of the
Requirements for the Degree of

MASTER OF SCIENCE

in the Department of Physics and Astronomy

The Mass Distribution of Protostellar and Starless Cores in Gould Belt Clouds

by

Sarah I. Sadavoy
B.Sc., York University, 2007

Supervisory Committee

Dr. J. Di Francesco, Co-Supervisor
(Physics and Astronomy)

Dr. D. VandenBerg, Co-Supervisor
(Physics and Astronomy)

Dr. K. Venn, Departmental Member
(Physics and Astronomy)

Supervisory Committee

Dr. J. Di Francesco, Co-Supervisor
(Physics and Astronomy)

Dr. D. VandenBerg, Co-Supervisor
(Physics and Astronomy)

Dr. K. Venn, Departmental Member
(Physics and Astronomy)

ABSTRACT

Using data from the SCUBA Legacy Catalogue (850 μm) and Spitzer (3.6 - 70 μm), we explore dense cores in the Ophiuchus, Taurus, Perseus, Serpens, and Orion molecular clouds. In particular, we focus on identifying which cores host young stars while others remain starless. Understanding the nature of star formation and the influence of local environment will give us insight into several key properties, such as the origin of stellar mass. Here, we present starless and protostellar core mass functions (CMFs) for the five clouds. We develop a new method to discriminate starless from protostellar cores, using Spitzer colours and positions. We found best-fit slopes to the high-mass end of -1.26 ± 0.20, -1.22 ± 0.06, -0.95 ± 0.20, and -1.85 ± 0.53 for Ophiuchus, Taurus, Perseus, and Orion, respectively. We were unable to fit a slope to our fifth cloud, Serpens. Broadly, these slopes are consistent with the -1.35 power-law seen in the Salpeter IMF, but suggest some differences. We examined a variety of trends between these CMF shapes and their parent cloud properties, potentially finding a correlation between the high-mass slope and temperature. We also attempt to predict what future surveys with SCUBA-2 will detect in each of our clouds.

Contents

List of Tables

List of Figures

ACKNOWLEDGEMENTS

≁

My supervisor, James, a great big hand
and thanks for sharing in your expertise.
To Rachel and to Helen you were grand,
For coding help each time my brain would freeze.

For my whole clan at home to you I say
that having your support let me get by.
You helped me from afar along the way,
and gave me chocolate in great supply.

For making sure I took time off for rest,
I thank my fellow grads and all my friends.
Sylvain, Luisa, Tom, Melissa, Jes
I thank you all; your patience knows no end.

Although this work is hardly poetry,
I hope it benefits Astronomy!

≁

DEDICATION

To anyone and everyone who
nurtured my interest in Astronomy,
whether it was in the classroom
or in an observatory.

This thesis is because of you.

Chapter 1

Introduction

Stars form in very cold and dense regions of gas and dust, deeply embedded within molecular clouds. Dust in these clouds blocks light from background sources, effectively making the regions appear as dark voids in the sky (see Figure 1.1). The amount of light lost is known as extinction, and regions of higher visual extinction (A_V) are typically more dense. Figure 1.1 shows one small dense region of molecular gas and dust, Barnard 68, observed at visible and infrared wavelengths. Given typical dust grain sizes of ~ 1 μm, light is absorbed significantly at visible wavelengths but less so at longer wavelengths (Stahler and Palla 2005).

Molecular clouds are mostly composed of molecular hydrogen (H_2) gas organized within different density and size scales, such as small dense clumps along larger filaments (Williams et al. 2000). Stars, however, only form via gravitational collapse of the densest small-scale structures ($\sim$ 0.1 pc) within the larger clouds ($\sim$ 10 pc). These small-scale regions, or "cores", can have densities $\gtrsim 10^4$ particles cm^{-3}. Most of the cloud mass, however, is contained within the large-scale cloud structures with densities of $\sim$ 300 particles cm^{-3} (in comparison, the interstellar medium has a density of $<$ 1 particle cm^{-3}; Stahler and Palla 2005). Since most of the mass is locked in the bulk cloud, star formation is relatively inefficient (e.g., Enoch et al. 2008, Evans et al. 2009).

We have chosen to define our molecular cloud "cores" as small, dense structures of similar mass to the sun (where 1 $M_\odot$ = 1.99 x 10^{33} g) that would form a single star or a stellar system with a few stars (Di Francesco et al. 2007). These cores are also very cold. Dust in the outer layers of a molecular cloud shield the inner layers from the interstellar radiation field, which would otherwise heat the interior (Evans et al. 2001). Also, the molecular gas is efficient at cooling the cloud. Collisions excite

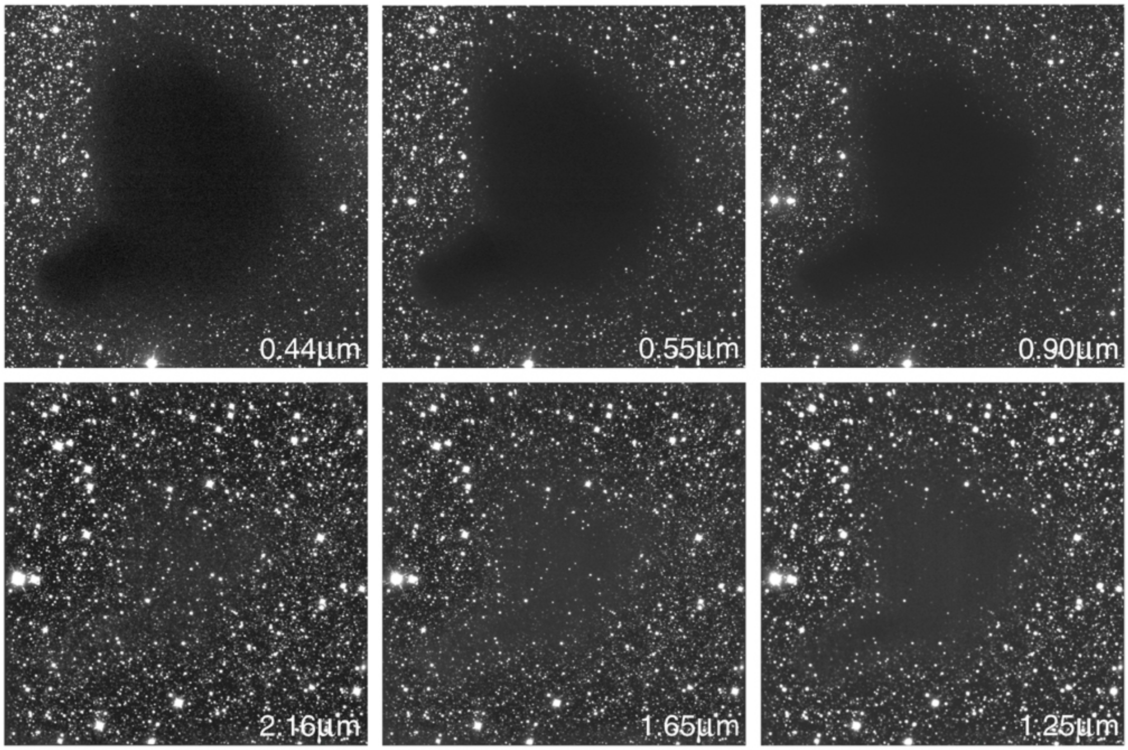

Figure 1.1 Barnard 68, a molecular cloud in the constellation Ophiuchus. With a mean density of $\sim 10^4$ cm^{-3} (Burkert and Alves 2009), Barnard 68 is opaque to background visible light (ie. wavelengths of 0.44 μm and 0.55 μm). At infrared wavelengths (bottom panels), background star light can pass through the dense cloud. This image was obtained from an ESO press release, http://www.eso.org/public/outreach/press-rel/pr-1999/phot-29-99.html

the gas molecules which radiate away the energy at long wavelengths, and these can escape the cloud easily. As a result, molecular clouds have temperatures < 50 K and drop to even cooler temperatures (~ 10 K) in the dense cores (Stahler and Palla 2005). After a star first forms within a core, the core can be heated internally, which will raise the local temperature (> 20 K).

Cold dust grains in molecular clouds emit thermal radiation with low energies, such as at far-infrared and millimetre wavelengths (ie., $100-3000$ μm). Direct observations of emission from the cold, dense cores is only achieved at these wavelengths. Figure 1.2 shows an 850 μm emission image (left) of the Horsehead Nebula taken from the SCUBA Legacy Catalogue, illustrating the clumpy small-scale structures (ie. cores) in the molecular cloud. For comparison, Figure 1.2 also includes an optical image (right) of the nebula. The 850 μm emission well traces the dark cloud seen in the optical.

If the temperature, dust opacity, and distance are known, optically thin, thermal

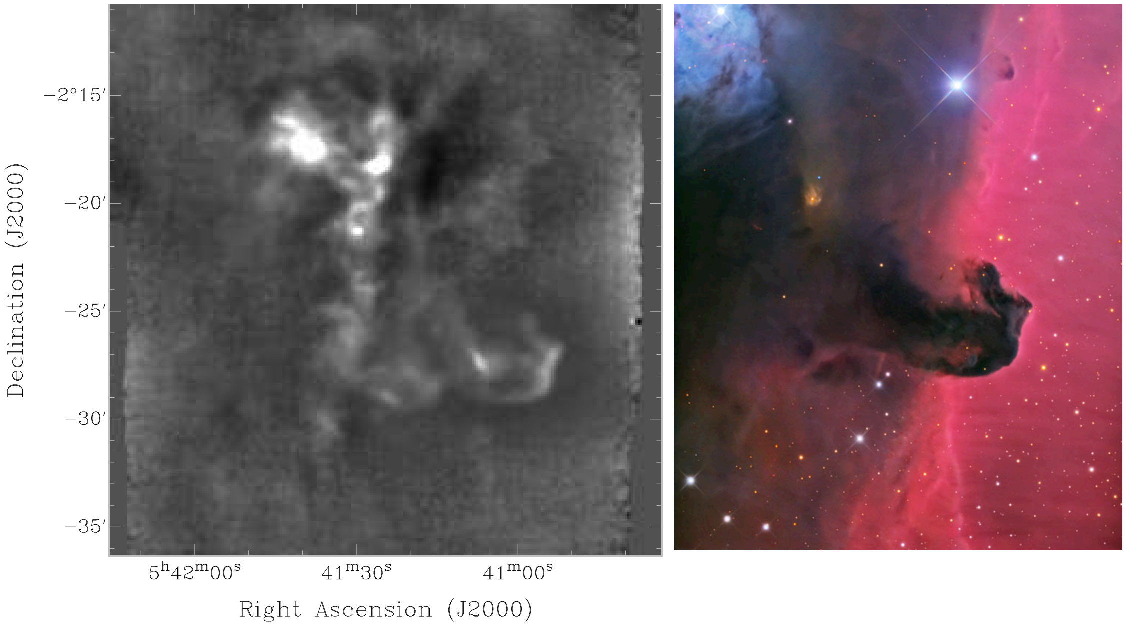

Figure 1.2 The Horsehead Nebula (Barnard 33) in the Orion molecular cloud. Left, a submillimetre (850 μm) continuum emission image from the SCUBA Legacy Catalogue. The submillimetre image shows emission from cold dust grains inside the dark cloud. Right, an optical image of the region illustrating the opaque cloud. The optical image is credited to Adam Block, Mt. Lemmon SkyCenter, and U. Arizona, and was taken from *Astronomy Picture of the Day*, http://antwrp.gsfc.nasa.gov/apod/ap081126.html.

continuum emission at submillimetre wavelengths can provide an estimate of the core mass (Di Francesco et al. 2007). The masses of molecular cloud cores are important probes to the initial conditions of star formation, and the relationships between these cores and any stellar products may be key to understanding the origin of stellar mass (Enoch et al. 2008).

Indeed, the most fundamental property of a star is arguably its mass. It determines a star's evolutionary path, chemical enrichment and ultimate fate. The origin of stellar mass, however, is not well understood. Studies of stellar populations have revealed many more low-mass stars than high-mass ones (e.g., Salpeter 1955, Miller and Scalo 1979, Kroupa 2002, Chabrier 2003). This observed distribution over three orders of magnitude in mass is known as the Initial Mass Function (IMF) and the origin of its shape, a roughly lognormal distribution with a power-law slope ($dN/dM = M^{-\alpha}$) at M $>$ 0.3 $M_\odot$, is not known (Williams et al. 2000). A better understanding of star formation will result from understanding the origin of stellar mass and the IMF.

Populations of molecular cloud cores seem to have a mass distribution with a power-law slope at higher masses that resembles the power-law slope in the IMF, (for examples, see Motte et al. 1998, Johnstone et al. 2000, Ward-Thompson et al. 2007a), suggesting that stellar mass is related to how material in molecular clouds is organized first into stellar precursors (ie., cores). The dominant mechanisms behind this organization, however, remain unclear. Swift and Williams (2008) tested outcomes from applying different evolutionary factors (ie., different star formation efficiencies or prescriptions for core fragmentation) on a simulated population of cores. They found that each of these evolutionary models resulted in a stellar mass distribution that resembled the observed IMF. This suggests that we need to better understand the properties and production of cores, themselves, to distinguish between different evolution scenarios.

Generally, only small samples of star-forming cores in a few clouds have been used to compute core mass distributions. More complete samples of core populations are needed to determine just how similar the core mass function (CMF) is to the IMF and how evolution will proceed. Indeed, the relationship between the CMF and IMF is likely very complex and should involve a variety of factors, such as fragmentation (e.g., Dobbs et al. 2005), competitive accretion (e.g., Bonnell et al. 2004), turbulence (e.g., Elmegreen 2002), magnetic fields (e.g., Shu et al. 2004), and radiative feedback (e.g., Offner et al. 2009).

Observations of core masses present the cumulative result of whatever physical processes organize cloud mass on small scales. Indeed, different clouds may have different CMFs due to differences in their characteristics and environments. For example, differences (if any) in the CMFs between clouds could reflect differences in the production and evolution of the cores, and presumably the origin of stellar mass. Unfortunately, an unbiased CMF can be difficult to determine. Observations of dense cores over the last decade have revealed populations of cores with and without embedded young stars (Di Francesco et al. 2007). Cores that contain a young stellar object (YSO) will have lost some of the surrounding material to accretion onto the central body or to outflows (Myers 2008). Also, their intrinsic temperatures may differ, distorting estimates of their masses. For cores that contain a central YSO, these processes will result in a biased estimate of the core mass. Thus, to obtain an accurate CMF, starless cores must be differentiated from those containing YSOs.

We have defined cores without a central luminous body as “starless”. Cores with a central luminous source are considered “protostellar”. Distinguishing between protostellar and starless cores depends on detecting a faint luminous source within the core. This distinction can be difficult to make given that these sources are embedded in dense material ($A_V \gtrsim 50$ magnitudes). For example, in Figure 1.3, the optical image (left) of L1014, shows a dark core in the constellation of Cygnus. This core was considered starless until recent infrared observations (right image) revealed a young protostellar source embedded within the core (Young et al. 2004). Not all infrared sources observed in molecular clouds are physically associated with that cloud, however. For example, many observed infrared sources are background active galaxies or bright giant stars in our own galaxy. Therefore, it is important to obtain data at a variety of wavelengths to determine the nature of the infrared source and its association with the cloud. Using infrared data from Spitzer such as these shown in Figure 1.3, techniques have been previously developed to distinguish between starless and protostellar cores (e.g., Jørgensen et al. 2007, Enoch et al. 2009, Evans et al. 2009).

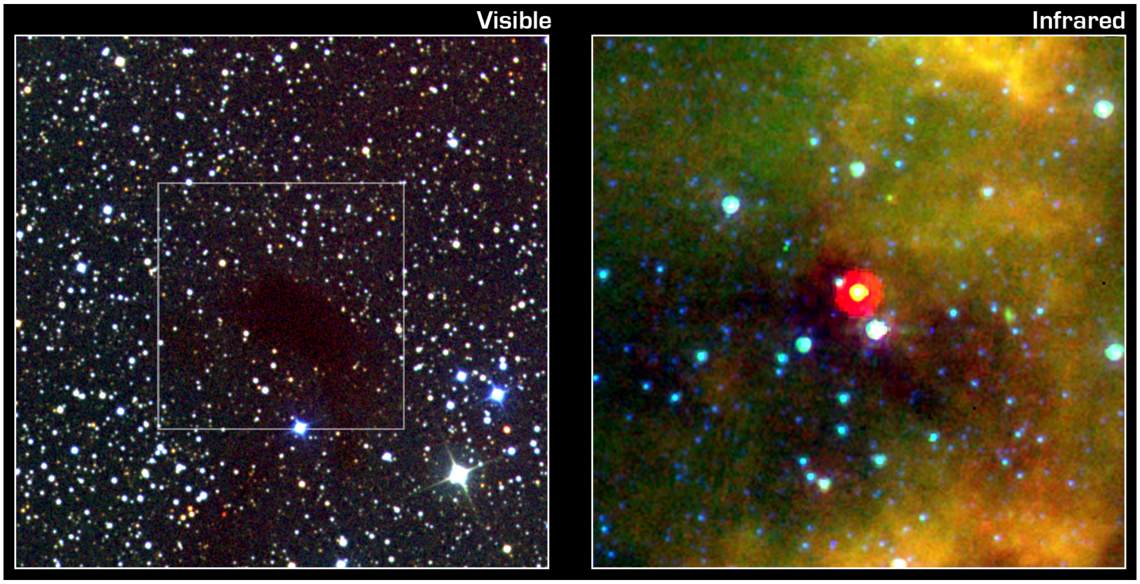

Figure 1.3 Comparing an optical and infrared image of L1014, a dark cloud in Cygnus. The cloud is opaque in the optical image (left), but an infrared image (right) taken by the Spitzer Space Telescope of the boxed region (see left panel) reveals an embedded protostar. The optical image is credited to DSS. The Spitzer image is credited to NASA, JPL-Caltech, and Neal Evans, and were taken from the Spitzer homepage, http://www.spitzer.caltech.edu/Media/releases/ssc2004-20/ssc2004-20a.shtml.

Not only do starless cores represent the initial conditions for star formation in a given cloud, but comparisons between populations of starless cores and populations of protostellar cores can reveal information on the evolutionary timescales, formation efficiencies, and the processes which drive core production in clouds (Enoch et al. 2008). For this thesis, we obtained data from large surveys (ie. the SCUBA Legacy Catalogue and just-released Spitzer data) to produce consistent CMFs across five different star-forming clouds. Using common techniques for analysis, including our own method for classifying cores as starless or protostellar, we examined similarities and differences between the CMFs of the five clouds in our sample.

In §2, we discuss our sample choices, including the target clouds and the infrared and submillimetre data used in this study. In §3, we discuss the individual core populations and selection criteria. We also discuss our new classification technique as well as two other previously developed methods. In §4, we examine the CMFs produced from our own classification method, and we compare these to standard formulations of the IMF. Also, we examine trends in the CMFs between the clouds, compare core properties with their surrounding environments, and make predictions as to what forthcoming instruments will detect.

Chapter 2

Clouds

2.1 Cloud Properties

Our analysis focused on the Ophiuchus, Taurus, Perseus, Serpens, and Orion molecular clouds. These clouds are associated with the Gould Belt, a band across the sky where many local star forming regions are located (Herschel 1847, Gould 1879). Gould Belt molecular clouds are good targets since many have been well surveyed using a variety of instruments (e.g., Bolocam, SCUBA, IRAC, MIPS) over several wavelengths, so their YSO populations and diffuse gas have been relatively well characterized (e.g., Kirk et al. 2006, Jørgensen et al. 2007). In addition, since Gould Belt clouds are relatively close (< 500 pc), we can map them with good linear resolution. Such small scale observations are necessary to resolve cores from each other as well as to probe the physical properties and structure inside cores (Ward-Thompson et al. 2007a).

The five clouds studied here represent a variety of physical environments. For example, the Taurus cloud is undergoing only low-mass star formation (Hartmann 2000) whereas the Orion cloud has several complexes of OB associations (Peterson and Megeath 2008). For Taurus, the mean N_2H^+ (1-0) line width is 0.3 km s^{-1} (Tatematsu et al. 2004), but for Orion, the mean N_2H^+ (1-0) line widths is ~ 2 km s^{-1} (Tatematsu et al. 2008). Similar observations in Ophiuchus, Perseus, and Serpens have revealed mean N_2H^+ (1-0) line widths of 0.5, 0.8, and 1.0 km s^{-1} (Friesen et al. 2009, Kirk et al. 2007, Williams and Myers 1999), respectively. Molecules of N_2H^+ trace the very dense (ie., $\sim 10^5$ cm^{-3}), very cold (ie., ~ 10 K) small-scale structures within clouds.

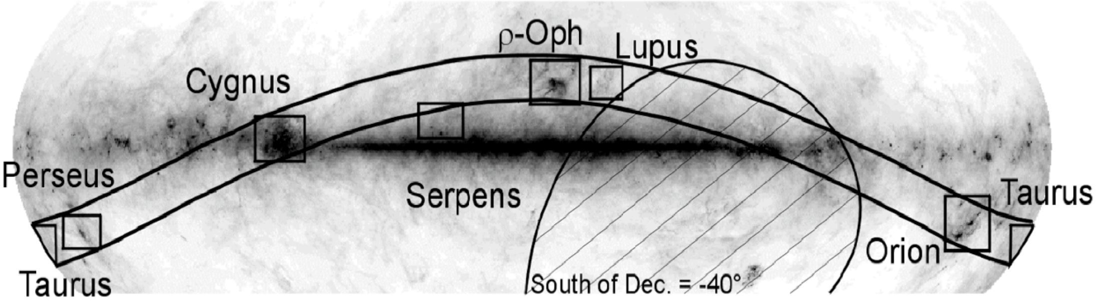

Figure 2.1 . Location of some molecular clouds with respect to the plane of our galaxy. The two black arches illustrate the Gould Belt region. The background image is an emission map at 100 μm from IRAS. This image was obtained from the JCMT Gould's Belt Legacy Survey webpage, http://www.jach.hawaii.edu/JCMT/surveys/gb/

Our five clouds also extend over a range of distances. The Ophiuchus and Taurus clouds are closest to the Sun and cover a wide angular extent in the sky. For Ophiuchus, a mass of 1 x 10^4 $M_\odot$ over 550 deg^2 was found by de Geus et al. (1990) using a distance of 125 pc. For Taurus, Ungerechts and Thaddeus (1987) found a mass of 3 x 10^4 $M_\odot$ within $\sim$ 200 deg^2 and assuming a distance of 140 pc. For Perseus, Ungerechts and Thaddeus (1987) found a mass of $>$ 1 x 10^5 $M_\odot$ with a distance of 350 pc. Kirk et al. (2006), however, using a more recent distance determination of 250 pc, found a mass of 1.9 x 10^4 $M_\odot$. The Perseus cloud is considerably smaller on the sky than Taurus and Ophiuchus, covering $\sim$ 21 deg^2. For the core region of the Serpens cloud, $\sim$ 0.005 deg^2, White et al. (1995) measured a mass of $\sim$ 1.5 x 10^3 $M_\odot$ assuming a distance of 311 pc. Using our more current distance of 260 pc, this mass would decrease by a factor of 1.4 ($\sim$ 1 x 10^3 $M_\odot$). For Orion, masses of 1 x 10^5 $M_\odot$ and 8 x 10^4 $M_\odot$ were found by Maddalena et al. (1986) for the Orion A and Orion B complexes, respectively, assuming a distance of 500 pc. Although the Orion cloud is significantly further than the others in this study, it still extends over a large region of the sky. Orion A and Orion B subtend areas of $\sim$ 29 deg^2 and $\sim$ 19 deg^2, respectively.

2.2 Core Properties

We used 850 μm continuum maps from SCUBA to identify cores (see §2.3.1). For each cloud, we assumed the dust in the cores had constant temperatures, T_d, and constant 850 μm opacities, κ_{850}. Temperatures and opacities of core dust probably deviate within a given cloud due to different circumstances, such as extinction levels within a cloud or the proximity of a core to an embedded cluster. Table 2.1 lists the assumed values for T_d, and distance for each cloud.

Table 2.1 Assumed Properties

Cloud	T_d (K)	Reference	D (pc)	Reference
Ophiuchus	15	Friesen et al. 2009	125	Enoch et al. 2009
Taurus	13	André et al. 2000	140	Goldsmith et al. 2008
Perseus	11	Rosolowsky et al. 2008	250	Enoch et al. 2009
Serpens	17	Schnee et al. 2005	260	Enoch et al. 2009
Orion	30	Johnstone et al. 2001	450	Peterson and Megeath 2008

We note that the temperatures listed in Table 2.1 were drawn from different techniques. Friesen et al. (2009) and Rosolowsky et al. (2008) derived kinetic temperatures, T_K, of dense gas in Ophiuchus and Perseus, respectively, using ammonia hyperfine structure lines. For the Ophiuchus and Perseus clouds, we consider a dust temperature equal to the mean kinetic temperature of the entire cloud, assuming that the kinetic temperature traces the dust temperature. This may not be the case as the dust can be colder than the gas (Friesen et al. 2009), but densities of dense cores are expected to be high enough for the temperatures to be similar (Goldsmith 2001). For the L1544 region in Taurus, André et al. (2000) used SED fitting from ISO, SCUBA, and IRAM observations to obtain $T_d = 13$ K. As part of the COMPLETE[1] survey, Schnee et al. (2005) used the 60μm/100μm flux density ratio for Serpens (see their Figure 5) to estimate a dust temperature. For Orion, Johnstone et al. (2001) assumed a dust temperature of 30 K for their analysis. While this temperature was not derived, Bonnor-Ebert sphere models at 30 K appeared to agree with their data. Clearly a common origin of T_d would be preferable for this study, but note that the masses of cores in the CMFs will scale with T_d and to first order the CMF shape will not depend on T_d (see §4 for further discussion). We assume a 30 % uncertainty in T_d to derive uncertainties in our masses and CMFs. Self-consistent determinations of T_d for cores in these clouds will soon be possible through SED fitting of $75 - 500$ μm data from the Herschel Gould Belt Survey (Ward-Thompson et al. 2007b).

---

[1] http://www.cfa.harvard.edu/COMPLETE/

2.3 Data

We obtained our data from large-scale surveys and included wavelengths from the submillimetre (850 μm) to the infrared (~ 2 μm to 70 μm). We used the submillimetre data to probe the densest regions of each cloud and the infrared data to study embedded protostars through emission and the extended cloud structure through extinction. We discuss each of these data sets in turn below.

2.3.1 SCUBA Maps

Dense cores are very cold (see Table 2.1), and as such, they can be observed in emission only at relatively long wavelengths (100 - 1000 μm). For example, a black body at a temperature of 10 K will have a peak intensity at ~ 0.3 mm. This makes submillimetre observations ideal probes of the cold, dense cores inside molecular clouds.

We obtained our submillimetre data from the SCUBA Legacy Catalogue (SLC)[2]. These data utilized the Submillimetre Common User Bolometer Array (SCUBA) on the James Clerk Maxwell Telescope (JCMT[3]) to map, in a piecemeal fashion, various molecular clouds at 850 μm and 450 μm. The SLC is a collection of all archived data, similarly reduced. The effective FWHM of the SLC data at 850 μm is $22.9''$, but the beam consists of a narrow component of $\sim 20''$ and a wide error beam of $40''$ FWHM. Submillimetre observations like those with SCUBA are ideal for locating small scale structures like cores, but are unable to provide much information on the large-scale structure of the clouds due to chopping.

For ground-based observations in the submillimetre, it is very important to accurately correct for the atmosphere. As such, the SLC includes two sub-catalogues: the Fundamental Catalogue, which contains only objects identified from data with high quality atmospheric corrections (consisting of ~ 78 % of map data with an areal coverage of ~ 19.6 deg^2), and the Extended Catalogue, which includes all the data regardless of quality (areal coverage of ~ 29.3 deg^2). Since we are more interested in accurate core fluxes (to make CMFs) than wide areal coverage of the clouds, we drew our sample from the Fundamental Catalogue. In addition, we used only the 850 μm data, since the 450 μm observations have a greater absolute flux uncertainty than the

---

[2] http://www1.cadc-ccda.hia-iha.nrc-cnrc.gc.ca/community/scubalegacy/

[3] The James Clerk Maxwell Telescope is operated by The Joint Astronomy Centre on behalf of the Science and Technology Facilities Council of the United Kingdom, the Netherlands Organisation for Scientific Research, and the National Research Council of Canada.

850 μm data by over a factor of two (Di Francesco et al. 2008). Table 2.2 lists the areal coverage mapped by SCUBA towards the five clouds studied here.

Table 2.2 Area Observed by Each Survey

Cloud	SCUBA (pc^2)	Spitzer (pc^2)	2MASS[a] (pc^2)
Ophiuchus	11.5	31.4[b]	486
Taurus	5.59	262[c]	1960
Perseus	52.0	73.6[b]	1920
Serpens	1.02	17.5[b]	252
Orion	85.9	800[d]	14252

---

[a] Areas of the entire 2MASS maps. For Ophiuchus and Orion, the 2MASS maps were edited to remove the Scorpius and Monoceros clouds, respectively (see Figure 2.3).

[b] Area with both MIPS and IRAC data (Evans et al. 2009).

[c] Area with only IRAC data according to the Delivery Document (see Padgett et al. 2008, http://ssc.spitzer.caltech.edu/legacy/taurushistory.html)

[d] Area with complete 4-band IRAC coverage (Megeath et al. in prep).

The SLC used the 2D Clumpfind algorithm (Williams et al. 1994) to identify structures in the continuum emission. First, Clumpfind identifies flux peaks over a certain noise level (ie., 5 σ) and then uses closed flux contours at lower flux levels to assign boundaries. The boundaries of clumps are defined when either the clump flux contours extend into another clump or the emission level reaches some minimum threshold. This threshold is a relatively arbitrary value, and different threshold levels could result in different core populations (Williams et al. 1994, Kirk et al. 2006, Di Francesco et al. 2008). For object identification, the SLC used a Clumpfind threshold level of 3 times the noise level of each map (Di Francesco et al. 2008).

For each object in the SLC, there are two different flux and size measurements. The first set is defined by the area inside the contour level that is a factor of 3 above the local noise level in a given map. The second set, labeled the "alternative" flux and radius, takes the same cores as the first set but defines the boundary by a common Clumpfind threshold of 90 mJy beam^{-1}, which is a factor 3 larger than the typical 850 μm noise level of all SLC maps, 30 mJy beam^{-1}. For example, Figure 2.2 illustrates the 90 mJy beam^{-1} contour around three submillimetre cores identified in Taurus. The effective radius, in either case, was defined as $r = \sqrt{A/\pi}$, where A is the area of each core determined from Clumpfind (Di Francesco et al. 2008). We used the alternative flux and radius to provide a consistent mass sensitivity for all the cores in a given cloud. Generally, the two flux and size measurements were quite similar.

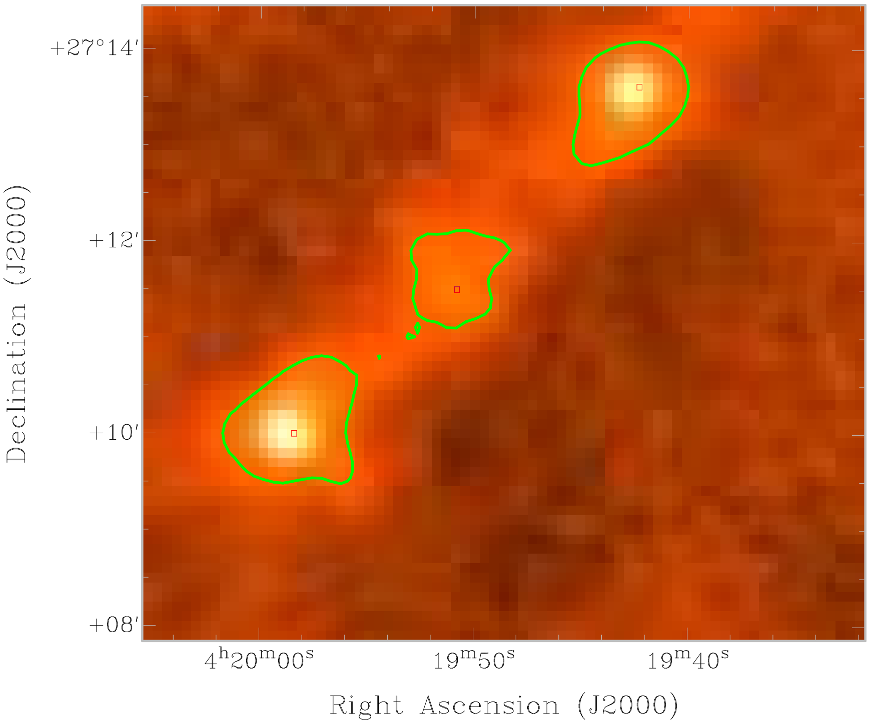

Figure 2.2 Three submillimetre cores in Taurus identified with Clumpfind. The red boxes represent the location of the peak fluxes in the cores and the green contours indicate the 90 mJy beam^{-1} flux levels.

2.3.2 Spitzer Space Telescope Maps

Emission in the mid- to far-infrared can reveal very young stars or protostars still embedded in cores. These YSOs are difficult to observe at optical wavelengths due to the high extinction levels of the associated material. Protostellar cores (ie. cores with embedded protostars) may have temperatures that are still quite low, only a few degrees more than starless cores, and their spectral energy distributions (SEDs) can still peak at long wavelengths. As such, protostars can be identified by infrared excesses and a number of colour criteria have been proposed in the literature (e.g., see Harvey et al. 2006, Evans et al. 2009, and Megeath et al. 2009).

Onboard the Spitzer Space Telescope[4] are two instruments that observe mid- and far-infrared wavelengths: IRAC (Infrared Array Camera) at $3.6 - 8.0$ μm and MIPS

---

[4] This work is based [in part] on observations made with the Spitzer Space Telescope, which is operated by the Jet Propulsion Laboratory, California Institute of Technology under a contract with NASA.

(Multiband Imaging Photometer for SIRTF) at $24 - 160$ μm. With the high infrared sensitivity provided by Spitzer, these cameras provided excellent data for determining the presence of a protostar within highly extincted regions like cores.

To separate the populations of protostellar and starless cores, we used mid- and far- infrared data from the Spitzer "Molecular Cores to Planet Forming Disks" (c2d) Legacy Project[5] for the Ophiuchus, Perseus and Serpens molecular clouds (see Padgett et al. 2008, Jørgensen et al. 2006, and Harvey et al. 2006, respectively). In addition, we also used Guest Observer (GO) observations for Taurus (L. Rebull priv. communication) and Guaranteed Time Observations (GTO) for Orion (S. T. Megeath priv. communication). Table 2.3 lists the source of Spitzer data for each cloud.

Observations with MIPS and IRAC did not cover identical areas. In general, MIPS observed more of a given cloud due to faster scan modes than IRAC. For c2d, the MIPS integration times were 3 seconds per sky pointing, with a given position observed 5 times for a total of 15 seconds. While the 24 μm and 70 μm bands covered roughly the same area of the sky, the 24 μm scans had longer total integration time (30 seconds) than the 70 μm scans (15 seconds) from a second sweep of the cloud roughly 6 hours after the first observations (Young et al. 2005). Observations at 160 μm were not included in the final c2d catalogues, since these data were affected by saturation and a large beam size (Evans et al. 2009). Similar to MIPS, IRAC observed each cloud twice, first in a high dynamic range mode, which involved alternating between short and long exposures, and then in a full array mode, which took one short exposure and several long exposures. The integration time per pointing with IRAC was 12 seconds (Porras et al. 2007). The sensitivities, for a 24 second total time, are 18.0, 17.3, 15.6, 14.6, 9.8, and 5.7 magnitudes for the 3.6, 4.5, 5.8, 8.0, 24, and 70 μm bands, respectively (Evans et al. 2003).

Due to different sensitivities (e.g., 3.6 and 4.5 μm are the most sensitive bands) and different areal coverages between the bands, there are a number of sources in the c2d catalogue that were detected at only a few wavelengths. Thus, the c2d team employed "bandfilling," a technique used to estimate the flux at any non-detected wavelengths using a wavelength appropriate point spread function (PSF), e.g., if a source was well detected in at least one of the IRAC bands or the 24 μm band. Such "bandfilled" sources were given an image type flag of "-2" in the catalogues. This process, however, sometimes resulted in negative band-filled fluxes. We remove the majority of these sources (see §3.2.1). For more information, see the *Final Delivery*

---

[5] http://ssc.spitzer.caltech.edu/legacy/

Table 2.3 References for IRAC and MIPS Data

Cloud	Observations	Reference[a]
Ophiuchus	c2d survey	Evans et al. 2009, (1)
Taurus	Guest Observer	D. Padgett, priv. comm.
Perseus	c2d survey	Evans et al. 2009, (1)
Serpens	c2d survey	Evans et al. 2009, (1)
Orion	Guaranteed Time	S. T. Megeath, priv. comm.

---

[a] Reference for the data and information: (1) http://ssc.spitzer.caltech.edu/legacy/.

Document for IRAC and MIPS data (Evans et al. 2007[6]).

The GO observations for Taurus were initiated by Padgett et al. and consisted of shallow observations over a very large region. MIPS observed each region over two epochs with fast scans and covered $\sim$ 48 deg^2. The Taurus observations, however, included many asteroids that could not be removed from the co-added MIPS observations. Thus, the Taurus data were analyzed from single epoch maps, limiting the depth of the observations. The IRAC observations were also relatively shallow. IRAC scans are slower than MIPS making it difficult to efficiently produce large, deep maps. IRAC observed $\sim$ 44 deg^2 of Taurus in high dynamic range mode only (see Delivery Document, Padgett et al. 2008[7]). The Taurus data were not bandfilled (L. Rebull priv. communication).

Orion was observed as a combination of IRAC and MIPS instrument team GTO time. MIPS cross scans were taken in slow (2.6 ″/sec), medium (6.5 ″/sec), and fast (17 ″/sec) modes for integration times of 30 - 40 seconds per cross scan. IRAC surveyed $\sim$ 9.3 deg^2 in Orion A and $\sim$ 3.7 deg^2 in Orion B in all four bands over two epochs using an average frame time of 10.4 seconds in high dynamic range mode (Megeath et al. in prep).

We converted all infrared fluxes into magnitudes using the standard Spitzer zero-point fluxes given in Table 2.4 (see Reach et al. 2005), via:

$$m_\lambda = 2.5 \log \left(S_0/S_\lambda\right) \tag{2.1}$$

where S_0 is the zero point flux and S_λ is the observed flux.

---

[6] http://ssc.spitzer.caltech.edu/legacy/c2dhistory.html

[7] http://ssc.spitzer.caltech.edu/legacy/taurushistory.html

Table 2.4 Spitzer Zero Point Fluxes

Instrument	λ (μm)	S_0 (Jy)
IRAC	3.6	280.9
IRAC	4.5	179.7
IRAC	5.8	115.0
IRAC	8.0	64.13
MIPS	24	7.17[a]
MIPS	70	0.778

---

[a] For Taurus, the zero-point flux was given as 7.14 Jy (based on observations of Vega).

2.3.3 2MASS Extinction Maps

Molecular clouds are dense regions and inferring their extinction structure can be difficult. An early technique, developed by Bok and Cordwell (1973), was to count the number of background stars. This method becomes increasingly difficult with fewer stars (e.g., at higher densities). Alternatively, infrared observations can probe column density by tracing the colour of reddened background sources through a cloud. This method can measure extinction levels an order of magnitude larger than extinction levels derived from optical star counts (Lombardi et al. 2006).

Reddening of stars can be used to estimate the total line-of-sight column density of dust. In particular, stars located beyond a molecular cloud have deeply reddened colours from the high column densities of dust in that cloud. Thus, the reddening of these stars can indicate the amount of dust (or A_V) in the direction of the stars (Lada et al. 1994). Typically, the average reddening of stars is measured using the near-infrared bands (e.g., J, H, and K).

Extinction maps for each of our five clouds were created by S. Bontemps using archived 2-Micron All Sky Survey (2MASS[8]) catalogues of point sources. The extinction itself was calculated from taking the average reddening of stars similar to the methods described in Lada et al. (1994), Lombardi and Alves (2001), and Cambrésy et al. (2002).

First, individual extinction values were obtained from a weighted average of the J-H and H-K colours of individual stars, assuming the average intrinsic colours were

---

[8] This publication makes use of data products from the Two Micron All Sky Survey, which is a joint project of the University of Massachusetts and the Infrared Processing and Analysis Center/California Institute of Technology, funded by the National Aeronautics and Space Administration and the National Science Foundation.

$(J\text{-}K)_0 = 0.45 \pm 0.15$ and $(H\text{-}K)_0 = 0.12 \pm 0.05$ as derived from stellar population models and typical dispersions of Galactic stars (see Robin et al. 2003[9]). Second, galactic models were used to predict the frequency of foreground stars in the 2MASS bands at the distance of each cloud. The expected number of foreground stars was removed from the least reddened 2MASS sources in each element of resolution. Finally, a Gaussian weighting function was applied to the local averages of individual A_V values. This weighting determined the resolution of the final map and was adapted so that $\gtrsim 10$ stars would significantly contribute to the extinction (S. Bontemp priv. communcation). Table 2.5 lists the pixel size for each extinction map. The resolution is roughly on the order of 3-5′ (Ridge et al. 2006).

Table 2.5 Extinction Map Properties

Cloud	Pixel Size (arcmin)
Ophiuchus	1.2
Taurus	1.6
Perseus	1.77
Serpens	1.25
Orion	2.0

2.3.4 Submillimetre - Infrared Coverage

Molecular clouds that are close to the Sun (< 500 pc) can subtend wide areas on the sky. Hence, relatively large time allocations have been required to map them to high sensitivity. As an all-sky survey, 2MASS data necessarily encompassed the full extent of all 5 clouds in this study. The Spitzer coverages of these clouds were quite large, but generally restricted to areas of $A_V \geq 3$. SCUBA was used to map large regions only rarely (see Johnstone et al. 2004, Hatchell et al. 2005, Kirk et al. 2006) given its limited sensitivity. Observations with SCUBA typically focused on regions of known star formation within the clouds. As Figure 2.3 shows, much of these clouds remain unmapped in the submillimetre, including some regions of high extinction. Table 2.2 lists the cloud area observed by each of the surveys. Physical distances quoted in Table 2.2 used the distances in Table 2.1.

---

[9] http://www.obs-besancon.fr/

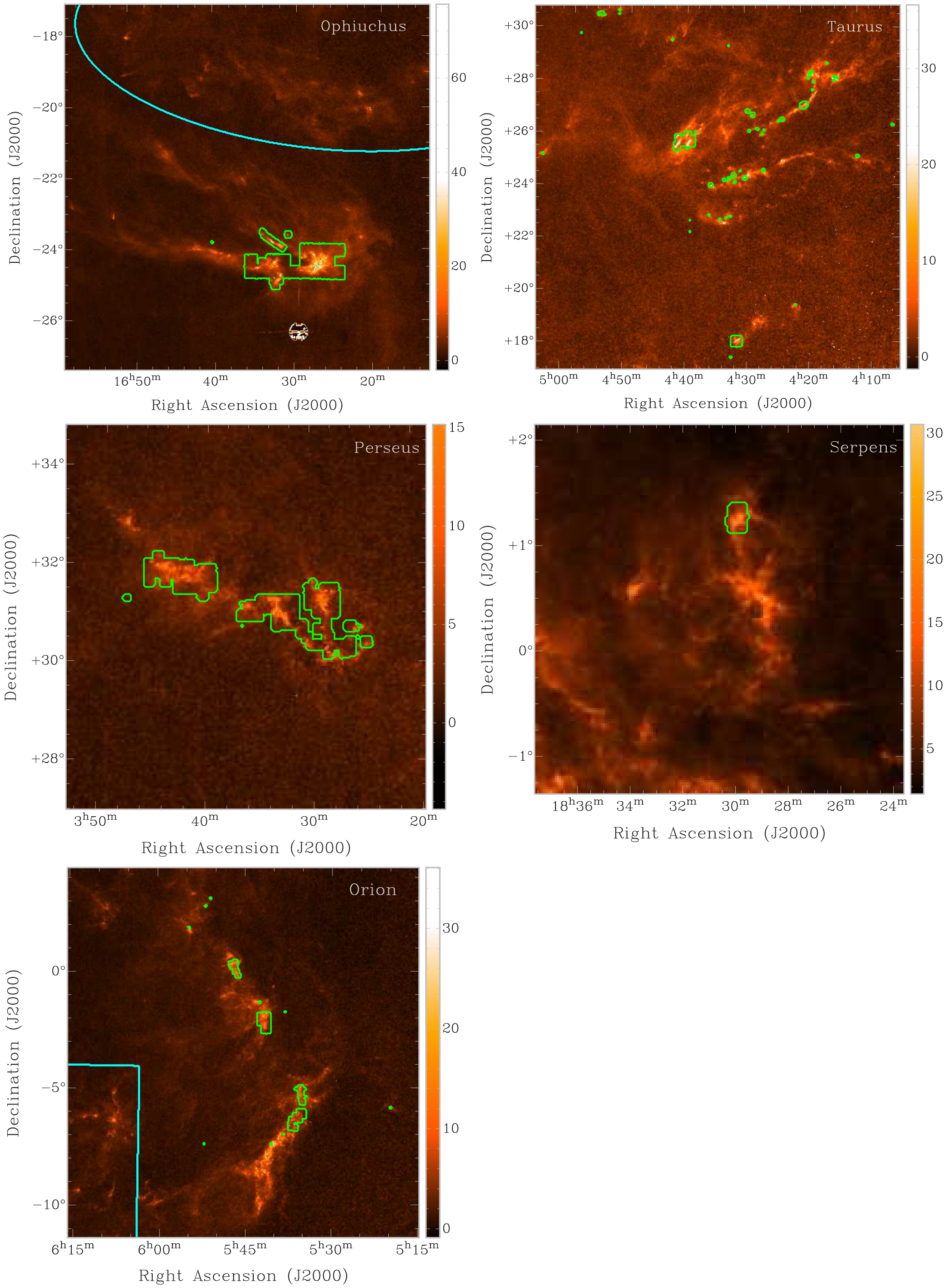

Figure 2.3 SLC Funamental Catalogue observations (green contours) with 2MASS extinction maps (background images) for all five clouds in this study. Cyan lines mark the rough boundary between the Scorpius and Monoceros clouds with Ophiuchus and Orion, respectively.

2.4 Identifying Cores within Clouds

As described before, we define “cores” as compact structures in molecular clouds that could produce one star or stellar systems of a few stars (Williams et al. 1994, Di Francesco et al. 2008). Small scale structures in the SLC were identified with the Clumpfind algorithm using two different threshold levels. We chose to use the alternative flux, thereby defining our cores down to a common threshold of 90 mJy beam^{-1}. Some of these objects are likely false detections, such as artifacts of imperfect flat fielding or chopping, and need to be removed. Also, we want to remove sources that were poorly detected and ones that appear too diffuse to be a *dense* core.

2.4.1 Associating Cores with Cloud Extinction Levels

We used the local extinction from the 2MASS data to determine the core locations within the large-scale structure of their parent clouds. We estimated the extinction at the position of each core by identifying the pixel that is nearest to the core centre. The nearest A_V pixels were found by projecting the SCUBA core positions in the sky onto the 2MASS extinction maps.

Figure 2.4 shows the distribution of extinction in the cores of each cloud following our selection critieria outlined below in §2.4.2. We use extinction bins of $\Delta A_V = 4$ to ensure each bin is well populated. For Ophiuchus, Taurus, Perseus, and Orion, there are clear peaks in the extinction distributions at $A_V \sim 25, 13, 9$, and 8, respectively. There is no such peak in the Serpens distribution, likely due to the low number of cores (i.e., only 15).

2.4.2 Preliminary Cuts

For this study, we required that cores be located in a cloud region of $A_V \geq 3$. We also removed all submillimetre sources that had alternative fluxes of $S_{850} = -99.99$, which indictated that they did not have peak intensities ≥ 90 mJy beam^{-1}. We visually inspected all remaining objects and removed those from the ensembles that were likely artifacts of flat-fielding or which appeared too diffuse to be cores. Finally, to ensure we had good detections, we removed all objects with peak fluxes less than 5 σ, where σ is the noise level of 30 mJy beam^{-1}. Table 2.6 summarizes all the cuts made to the objects extracted from the SLC Fundamental Catalogue. The initial object count for each cloud indicates the number of submillimetre cores that fell within the RA and

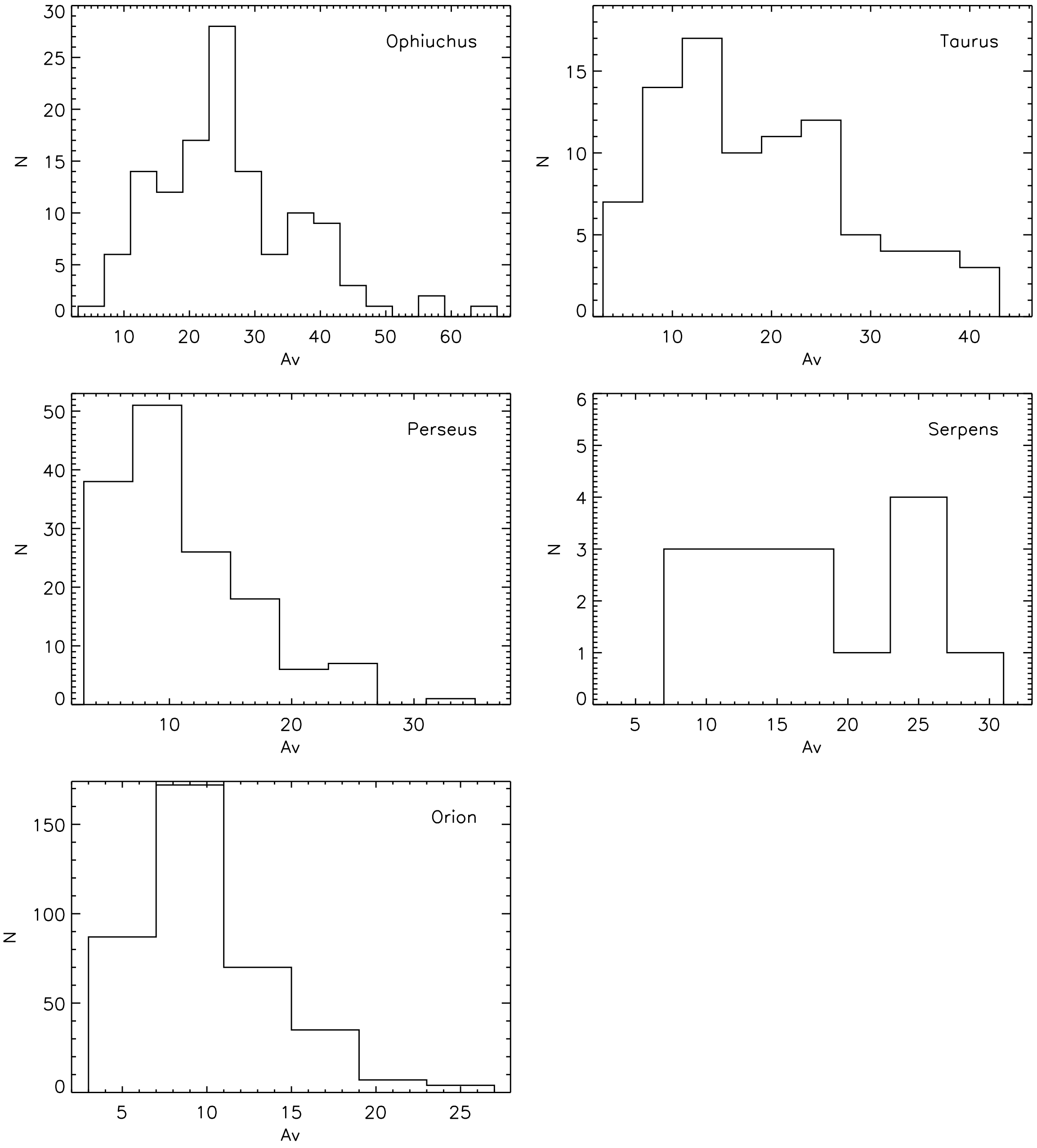

Figure 2.4 Visual extinction distribution for cores in Ophiuchus, Taurus, Perseus, Serpens, and Orion. The histograms are binned to $\Delta A_V = 4$ for all five clouds. This distribution does not distinguish between starless and protostellar cores.

DEC range of the clouds. For Serpens, only one relatively small region of ~ 1 pc^2 was observed with SCUBA, resulting in far fewer core numbers relative to the other clouds.

Table 2.6 Summary of Cuts to the SCUBA Object List

Cloud	Initial	$A_V < 3$	$S_{850} = -99.99$	Visual	$S_{peak} > 0.15$	Remaining
Ophiuchus	151	1	0	16	10	124
Taurus	172	10	15	30	30	87
Perseus	246	14	1	57	27	147
Serpens	19	0	0	4	0	15
Orion	448	12	5	39	17	375

2.4.3 Angular Separation

Our ability to resolves cores will vary with distance, and the five clouds in our sample clouds are located at $125 - 450$ pc (see Table 2.1). As such, cores that are resolved in more nearby clouds (ie., Ophiuchus at 125 pc) may be blended in clouds at greater distances (ie., Orion at 450 pc). Resolution will have a significant effect on detecting specific cores in crowded regions.

We calculated the projected separation between each core in our sample to all other cores in a given cloud using the positions of the 850 μm flux peaks. Most cores had a nearest neighbour (or minimum separation) < 0.5 pc. Table 2.7 lists the average of those minimum separations with their standard deviations. When calculating the standard deviation, we considered only nearest neighbours < 1 pc since outlying cores increased our uncertainties well beyond the scale of the mean value.

Table 2.7 Mean Minimum Separations Between SCUBA Cores

Cloud	Cores	Separation (deg)	Separation (pc)
Ophiuchus	124	0.03 ± 0.042	0.066 ± 0.094
Taurus	87	0.143 ± 0.064	0.350 ± 0.155
Perseus	147	0.026 ± 0.032	0.112 ± 0.140
Serpens	15	0.015 ± 0.007	0.069 ± 0.032
Orion	375	0.026 ± 0.012	0.203 ± 0.094

The mean minimum separations (in parsecs) are actually fairly similar in spite of differences in distance, suggesting we are resolving cores. Figure 2.5 compares the mean core radius with the average minimum separation. We used the alternative radius, which is defined as $r = \sqrt{A/\pi}$ where A is the area within the 90 mJy beam^{-1} contour. With the exception of Orion, there is a possible negative correlation between core size and minimum separation, which suggests that crowded regions have larger core sizes than less populated regions. We would expect that cores in crowded regions are more likely to be blended together, thus increasing their observed size. Orion, at almost twice the distance than any other cloud studied here, has the largest mean core size but not the smallest mean minimum separation. Orion is much further than the other clouds, making its cores more difficult to resolve, particularly in crowded regions. This effect could result in fewer cores with nearby neighbours and thereby increase the average minimum separation. In general, we examine populations from each cloud individually, and do not combine results from different clouds.

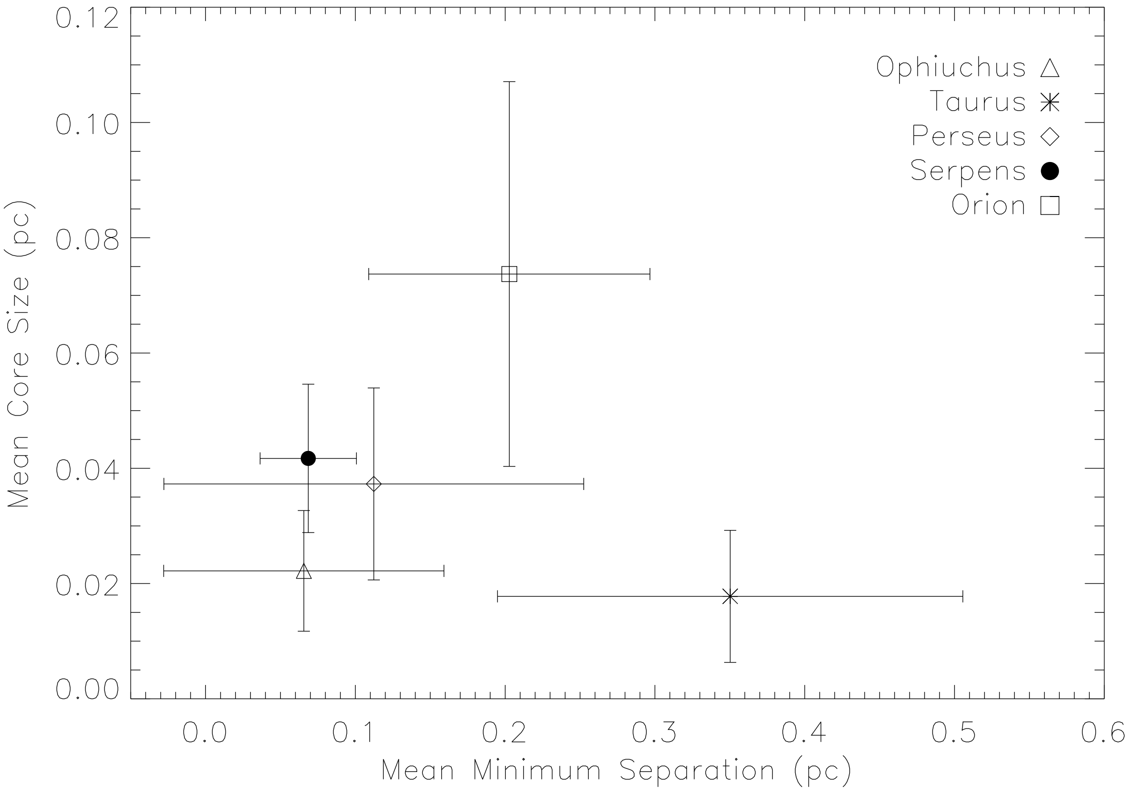

Figure 2.5 Comparison of mean core size and the average minimum separation between all cores in each cloud. We used the alternative SCUBA radius to estimate the core size and calculated minimum separations between cores using the position of the flux peak. Uncertainties were determined from taking the standard deviation from the mean, however we did not include largely isolated cores (separations > 1 pc) in calculating the error for the minimum separation because those cores greatly affected the deviation.

Chapter 3

Results

In this section, we summarize the methodology used to classify cores as starless or protostellar. In §3.1, we give an overview of two earlier methods to core classification, and using the cores identified in §2.4 we compare their results. We outline our new core classification technique in §3.2.

3.1 Separating Starless and Protostellar Cores

In compiling samples of cores observed in each cloud, we did not distinguish between different stages in core evolution, such as those that are starless (lacking a luminous object in the centre) or those that are protostellar (containing a young stellar object, YSO). These populations must be separated to explore properly the relationship between the IMF and CMF. For example, the CMF should be ideally populated with only starless cores (Ward-Thompson et al. 2007b). YSOs themselves can be further divided into a class system developed by Lada and Wilking (1984) based on the shape and peak of their SED. For example, Class 0/I describes sources with collapsing envelopes, Flat describes sources in the process of losing envelope mass due to outflows, Class II describes sources that are accreting from a disk, while Class III describes sources that have lost most of their outer circumstellar material (White et al. 2007).

Previous efforts have attempted to separate the starless and protostellar core populations in molecular clouds by comparing Spitzer or 2MASS data with (sub)millimetre continuum data. Slightly different methodologies were used, however, to accomplish this separation. To compare these methodologies, we derived starless and protostellar core populations for the SLC and Spitzer data using the methods described by Jørgensen et al. (2006, 2007, 2008; hereafter J06, J07 and J08, respectively) and Enoch et al. (2008, 2009; hereafter E08 and E09, respectively). Both methods required identifying Spitzer sources in close proximity to dense submillimetre cores. We discuss differences between these two techniques in §3.1.3.

3.1.1 Jørgensen Method

The Jørgensen method is outlined in J06, J07, and J08, and used Spitzer c2d data and non-SLC SCUBA observations for Perseus (J06) and Ophiuchus (J07). Qualitatively, their process of identifying protostars had two approaches. First, cores were identified as protostellar if a MIPS source was found within 15″ (i.e., 1 FWHM of the unsmoothed, non-SLC SCUBA beam) of the core centres. Second, IRAC/MIPS sources are identified as protostars by their red colours. The former criterion focused on protostars specifically associated with cores, while the latter was not so restricted. Quantitatively, their criteria to classify objects as protostars or protostellar cores is:

1) high quality 24 μm or 70 μm sources within 15″ from a SCUBA core, or

2) high quality 24 μm or 70 μm sources detected in all four IRAC bands with

$$\begin{aligned} [3.6]-[4.5] &> 1 \text{ and} \\ [8.0]-[24] &> 4.5. \end{aligned}$$

High-quality Spitzer sources were defined as those with a signal-to-noise level $(S/N) \geq 5$. Sources with non-detections or within 2 pixels of the mosaic edge (flag of “N”) in any IRAC band were removed.

J06 and J07 included a third parameter, the concentration of the SCUBA core. Core concentration measures the brightness distribution, where a high concentration indicates that the flux is centrally peaked. This criterion was added for cases where the 24 μm flux was saturated. After sampling Perseus, however, J07 found that many low concentration cores contained embedded protostars and concluded that concentration was not a good assessment for identifying YSOs (see also J08).

We do not consider the core concentration in our analysis. We also do not consider the red colours identified in the Jørgensen method. We are interested in only classifying SCUBA cores as starless or protostellar to produce unbiased CMFs. The red sources identified by the Jørgensen method are not constrained to the submillimetre cores, making their associations with the detected submillimetre objects unclear.

3.1.2 Enoch Method

To separate starless from protostellar cores, E08 and E09 used 1.1 mm data obtained with the Bolocam 1 mm continuum mapping array on the Caltech Submillimeter Observatory (CSO) and Spitzer c2d data for the Ophiuchus, Perseus, and Serpens clouds. For reference, the Bolocam 1 mm beam is $\sim 40''$. E09 used several criteria to optimize the infrared source list for protostars. Qualitatively, the Enoch method focused on red objects that are suitably bright. For a Bolocam core to be considered protostellar with this technique, a red, bright Spitzer source must fall within 1 intrinsic core FWHM of the core centre. The FWHM is given in E08 as the deconvolved core radius (θ_{dec}). Quantitatively, E09 used the following criteria to identify cores as protostellar:

1) non-bandfilled 24 μm objects with S/N ≥ 7, and
    - $S_{24} > 3$ mJy, and
    - $\nu_{24} S_{24} > \nu_8 S_8$, and
    - "class", as identified by c2d, began with "YSOc" or was "red", and
    - $S_{24} > 5\alpha + 8$ mJy, or
2) strong S_{70} source (ie. $S_{70} > 400$ mJy) that isn't a galaxy candidate

where bandfilling is represented by a flag of "-2" in column 118 of the c2d catalogue and α is the spectral index. For the case of strong 70 μm emission, a limiting flux of 400 mJy was used in this analysis, but E09 used a slightly different approach (M. Enoch, priv. communication).

3.1.3 Method Comparisons

Table 3.1 compares the number of protostellar and starless cores recovered by the Jørgensen and Enoch methods from their respective source data and the fraction of cores identified as protostellar. Since these methods used the c2d catalogue, only Ophiuchus, Perseus, and Serpens are listed. The protostars enumerated in Table 3.1 for the Jørgsensen method are only those that were identified using the $15''$ distance criterion (we did not adjust this distance to account for the larger beam with the SLC data), to ensure that the objects counted are those with a detected, associated submillimetre core. Recall that the Jørgensen method used cores identified with SCUBA ($15''$ FWHM) while the Enoch method used cores identified with Bolocam

(40″ FWHM) for their respective analyses, and so the core numbers, locations and sizes from each sample will differ. Regardless of these differences, the resulting protostar fractions given in the literature are quite similar, with $\sim 50\%$ for Perseus and $\sim 40\%$ for Ophiuchus. Note that Serpens was not examined by Jørgensen et al. unlike E09.

To emphasize the differences between each technique, we also applied both methods to our list of SCUBA cores (see §2.4). These results are given in Table 3.1. Using our SLC data, we found that many cores had multiple infrared sources associated with them, particularly with the Enoch method. The Enoch method also had several cases where multiple cores were associated with a single IR source. We represent such cases in Table 3.1 by listing upper limits to the actual protostellar counts using the Enoch method. We did not conduct a visual inspection to remove this multiplicity as there was no prescription for this in E09. If we could account for the multiplicity, we might find better agreement between the number of protostars identified by the two methods for Ophiuchus and Perseus.

Table 3.1 Protostar Numbers Found in the Literature and Our Core Lists

		Literature			Our Core List		
Cloud	Method	Cores[a]	Proto[b]	fraction	Cores[c]	Proto[d]	fraction
Ophiuchus	Jørgensen	66	24	0.36	124	25	0.20
	Enoch	43	17	0.40	124	<33	<0.27
Perseus	Jørgensen	72	39	0.54	147	42	0.29
	Enoch	122	55	0.45	147	<49	<0.33
Serpens	Jørgensen	⋯	⋯	⋯	15	8	0.53
	Enoch	35	20	0.57	15	7	0.46

---

[a] Cores found using either non-SLC SCUBA 850 μm (J07) or Bolocam 1.1 mm (E08) observations. Ophiuchus results are found in J08 whereas Perseus results are found in J07.

[b] Refers to protostellar objects. The Jørgensen et al. objects listed here are the protostars embedded in cores only (these do not include Spitzer sources with their red colours).

[c] Refers to our SLC-derived core list (see §2.4).

[d] Same as note "b", with an upper limit to the E09 technique protostellar cores due to several cases where multiple cores were associated with a single infrared source.

Even with the multiplicity removed, the two methods would not entirely agree, likely in part due to their treatments of infrared sources. Different infrared critieria result in very different initial infrared source lists. In one case, a Spitzer source within 15″ from a submillimetre core in Ophiuchus was designated as a galaxy candidate in the c2d catalogue. Using the Jørgensen method, this core was considered protostellar, but using the Enoch method, which removes objects with undesirable c2d designations, this core was considered starless. There were also a few cases where both methods identified a core as protostellar using different infrared sources.

While both methods yield similar protostellar core counts using our core lists for the three Clouds (see last column of Table 3.1), the protostar fractions are dissimilar from what the respective authors obtained using their own data (see middle of Table 3.1). With our core lists, we find a factor $\lesssim 1.9$ decrease in the protostar fraction from what is quoted by each group. Serpens aside, our core lists are generally larger (by factors of $\sim 1.2 - 3$), but our protostar fractions do not reflect the increased number of cores. This is likely related to the differences in our submillimetre sources. Enoch et al. based their method on Bolocam sources detected at a longer wavelength (1.1 mm) and with a larger beam size than our SCUBA cores. For E09, their 1.1 mm Bolocam observations have a resolution of $\sim 40''$ and may sample cooler, more extended material than what was sampled by SCUBA.

Our sources are also different from those used by Jørgensen et al., who used slightly different 850 μm data than the SLC. First, the Jørgensen et al. data had a larger areal coverage than the SLC Fundamental Catalogue. For Ophiuchus and Perseus, Jørgensen et al. obtained data from archives and the literature (Johnstone et al. 2004 and Kirk et al. 2006, respectively) for a total areal coverage of ~ 4.6 deg^2 in Ophiuchus and ~ 3.6 deg^2 in Perseus. The SLC Fundamental Catalogue has ~ 2.4 deg^2 in Ophiuchus and ~ 2.7 deg^2 in Perseus. Second, Jørgensen et al. reduced their data following Kirk et al. (2006), using a threshold of 3 times the mean pixel noise with Clumpfind, whereas we measured core properties using the alternative flux, which demands a Clumpfind threshold of 90 mJy beam^{-1} (3 times the average noise of all maps). The number and size of cores identified by Clumpfind is very dependent on the minimum threshold chosen. A lower threshold will result in more cores identified (Kirk et al. 2006). Third, the Jørgensen et al. maps had a pixel resolution of $3''$ and a beam angular resolution $\sim 15''$, whereas the SLC has a pixel resolution of $6''$ and a smoothed beam angular resolution $\sim 23''$. This difference may bias our results towards larger, fluffier cores. Such objects may be relatively less evolved and hence less likely to contain a protostar, possibly explaining why our larger core list does not include a proportional number of protostellar cores. This conclusion is unclear, however, since J07 found several examples of protostellar cores with low concentrations.

In addition to different cores lists, structure-finding algorithms (ie. Clumpfind) are very sensitive to the input parameters, and different techniques for identifying cores could result in very different populations. For example, Hatchell et al. (2005) found 91 cores in Perseus where Kirk et al. (2006), using a higher Clumpfind threshold, found 58 cores. Thus, differences in Clumpfind or similar algorithms could result in different definitions of what was identified as a core and may further explain why our core lists differ from those in the literature.

A major difference between the methods is how the protostellar cores are themselves identified. The Jørgensen method defined cores as protostellar if an infrared source was within $15''$ of their peak submillimetre positions. For small cores, however, $15''$ may extend beyond the respective boundaries of the cores, e.g., when a core has an effective radius that is less than $15''$[1] or is very elongated. Also, an angular radius of $15''$ covers a different physical scale at 250 pc (Perseus) than at 125 pc (Ophiuchus). In contrast, the Enoch method used the effective angular size of the cores themselves, which can be quite large ($\sim 50''$), and a larger search area has a greater intrinsic chance of coincidence with a nearby infrared source. This definition may explain why there are several cases where an infrared source is associated with multiple cores when using the Enoch method. E09 mitigated against these problems by applying additional criteria based on colours, but it is difficult to remove the issue entirely. In particular, removing infrared sources with undesirable c2d designations may be too biased. The mechanism for source designation was developed using a small region in Serpens observed with the c2d integration times. The same process may not apply to other regions, particulary those observed differently, ie., Taurus (see §2.3.2; L. Rebull, priv. communication).

One common obstacle for the Jørgensen and Enoch methods is that cores are not typically circular (in projection on the sky), so looking for infrared sources within a specified radius (independent of position angle) does not take the core shape into account. A robust protostellar core identification technique should ensure that an infrared source with protostellar colours is directly associated with a compact source of millimetre emission. Such a challenge must take into account not only the properties of the infrared source (e.g., its colours), but also the irregular shape of the core. In addition the classification method should also be applicable to clouds at various distances. By creating such a robust classification technique, properties of core properties in different environments can be compared without biases introduced

---

[1] The SLC constrains cores to a minimum area of 8 pixels, a limit given by the effective beam. This means $R_{eff} \geq 9.6''$ (from $A = \pi R_{eff}^2$) for pixel sizes of $6''$x$6''$.

from tailoring the method to each cloud.

3.2 A New Classification Technique

There are many possible approaches to identifying protostellar cores. In the previous section, we described the Jørgensen method and Enoch method, which differently use the proximity of an infrared source to a millimetre core, but one could also use the shape of the SED (Hatchell et al. 2007, Evans et al. 2009) or the infrared colours (Harvey et al. 2006, Kirk et al. 2009, Megeath et al. 2009). Hatchell et al. (2007) compiled source SEDs from a variety of wavelengths (1 μm to 1100 μm) and classified cores based on their bolometric temperature, luminosity ratios, and flux ratios. The c2d survey team (Evans et al. 2009) measured bolometric temperatures and spectral indices from source SEDs to classify their Spitzer sources and plotted them in colour-colour diagrams to determine trends. Harvey et al. (2006), Kirk et al. (2009), and Megeath et al. (2009) used specific colour requirements to remove contaminants and keep very red objects. For example, Megeath et al. (2009) used models developed by Allen et al. (2004) to determine protostellar colour conditions.

But which approach to use? All of these methods are subject to uncertainties from unknown reddening levels and possible chance coincidences. We compared the Jørgensen and Enoch methods in §3.1.3 and found that there was a general agreement in the number of protostellar cores identified, but not necessarily with the same cores. Overall, a core can be accurately classified by its SED, but this requires a wealth of high-resolution data at a variety of wavelengths, which is observationally expensive. In addition, the problem of using different wavelengths to associate objects at different resolutions still remains.

Combining colour and spatial co-location criteria would be least biased to particular data sets such as those with high resolution or large spectral coverage. Accordingly, we synthesize a new core identification scheme in §3.2.1 and §3.2.2.

3.2.1 Colour Criteria

To produce a starless CMF, one must identify and omit sources that have lost some of their surrounding envelope (ie., contain an embedded protostar that is accreting or ejecting its surrounding material). This task is complicated because additional sources of infrared emission that are not associated with the cloud, e.g., galaxies and background stars, may be along the line of sight. Thus, several authors have published colour or magnitude limits for identifying interlopers that are external and unrelated to clouds. Table 3.2 lists some of the conditions used by several authors to identify non-YSO contaminants. In general, extragalactic sources are often very faint or have unique colours (Gutermuth et al. 2008) whereas stellar sources are more likely to have flat spectra (Harvey et al. 2006). The most likely candidates for stellar contamination are evolved AGB stars, which are naturally redder in colour and bright enough to be seen at $\sim$ 10 kpc scales (Harvey et al. 2007). Unlike extragalactic sources, however, stellar contaminants will not be distributed uniformly across the sky. Clouds coincident with the Galactic plane, however, will have more stellar contaminants (Gutermuth et al. 2008).

Table 3.2 Previous Criteria to Distinguish YSOs from Interlopers

Condition	Interloper	Reference
$[4.5] - [8.0] > 1$	AGB star	Harvey et al. 2006
$[8.0] < 14 - ([4.5] - [8.0])$	Galaxy	Harvey et al. 2006
$[24] < 12 - ([8.0] - [24])$	Galaxy	Harvey et al. 2006
$[24] < 10$	Galaxy	Harvey et al. 2007
$[24] < 8.46$	Galaxy	E09
$[24] \leq 9.15$	Galaxy	Megeath et al. 2009
$[8.0] < 13 - ([4.5] - [8.0])$	Galaxy	Kirk et al. 2009

In addition to the non-YSO identification techniques listed in Table 3.2, Gutermuth et al. (2008) suggested further steps for removing contamination from star-forming galaxies and active galactic nuclei (AGN). Star-forming galaxies and narrow-line AGN have particular spectral signatures due to strong polycyclic aromatic hydrocarbon (PAH) emission, causing an increased infrared excess at 5.8 μm and 8.0 μm. Broad-line AGN, however, have infrared colours that are very similar to YSOs and thus, are more difficult to identify and remove. As such, broad-line AGN must be removed according to magnitude (Gutermuth et al. 2008).

Actual protostars should have red colours that will distinguish them from stellar sources. Several studies have been recently conducted to separate embedded protostars from false detections. Many use IRAC and MIPS colours (e.g., Harvey et al. 2006, J07) and sometimes 2MASS colours (e.g., Hatchell et al. 2007). Other still use SEDs and the spectral index (e.g., E09, Kirk et al. 2009) or the bolometric temperature (e.g.,Evans et al. 2009) to help classify objects and then develop colour criteria based on clustering in colour-colour space. Table 3.3 lists colour criteria from these studies that were used to identify embedded protostars (e.g., Class 0/I).

Table 3.3 Previously Published YSO Colour Criteria

Condition	Reference
$[4.5] - [8.0] > 1.4$	Harvey et al. 2007
H - K > 0.8	Hatchell et al. 2007
$[3.6] - [4.5] > 1$	J07
$[8.0] - [24] > 4.5$	J07
$[3.6] - [5.8] > 1.5$	Evans et al. 2009
$[8.0] - [24] > 3.5$	Evans et al. 2009
$[3.6] - [4.5] \geq 0.652$	Megeath et al. 2009
$[4.5] - [24] \geq 4.761$	Megeath et al. 2009

Even with the criteria presented in Tables 3.2 and 3.3, there is no perfect method to identify protostellar cores through colour. Colour conditions are made on a best effort basis to select objects that are most likely to be protostellar. Given the scatter and overlap of various objects in colour or magnitude, there will be some objects that are not selected, and conversely, not all contaminants will be removed. In addition, excesses in some bands could be the result of different physical processes. For example, emission at shorter wavelengths is more influenced by dust reddening than longer wavelength emission (Evans et al. 2009), though this effect should be minor as the reddening law is generally flat within the IRAC bands and rises in the $\lesssim 3$ μm regime (Nishiyama et al. 2009). Still, this reddening could complicate the interpretation of 3.6 μm and 2MASS emission, particularly in cases of embedded clusters. As well, shocks from outflows interacting with the molecular cloud can result in strong 4.5 μm emission due to shocked H_2 gas, affecting colour excesses involving 4.5 μm (Gutermuth et al. 2008). A recent study of Perseus by Hatchell and Dunham (2009) found several instances where shocked H_2 gas from outflows was initially classified as protostellar. Such detections make the 4.5 μm band a less reliable indicator of a protostar. For the longer IRAC bands, lower sensitivities can also limit protostellar core detections (Megeath et al. 2009), though this problem appears more apparent in outflow rich locations (e.g., Orion). In these particular regions, the shorter wavelengths may be more reliable (S. T. Megeath priv. communication).

Considering previous studies regarding contaminants (Table 3.2) and YSO colours (Table 3.3), we adopted colour criteria based on the results from the c2d catalogue (Evans et al. 2009). The c2d-overview study by Evans et al. (2009) contained a very large sample of YSOs (1024 over 5 clouds) classified using SEDs from the c2d catalogue. They based their colour limits on clustering trends of Class 0/I, Flat, Class II, and Class III objects in colour-colour diagrams (see their Figure 11) and so, the colours reflect the different classes (ie., they reflect the degree to which sources are embedded). When combined with bolometric temperatures or YSO models, infrared colours have less ambiguity.

To identify all embedded protostellar cores in our core list, we must find young protostars still embedded in a dusty envelope (Class 0, Class I and Flat spectral source types). We have modified the Class 0/I boundary from Figure 11 of Evans et al. (2009) to include objects with Flat spectral classes, which should include objects still fairly embedded (J08, Myers 2008). If a particular object was not detected in MIPS, then we included an IRAC criterion using the $[4.5]-[8.0]$ colour from Harvey et al. (2007). Objects with 24 μm emission that fail to meet our revised c2d colour criterion are not considered protostellar. In addition to this, we removed star forming galaxies using the technique from Gutermuth et al. (2008).

Our complete colour criteria (CC) for identifying protostellar objects is listed below:

CC 1. source 24 μm or 70 μm flux has a $S/N \geq 5$, and

CC 2. neither source 24 μm nor 70 μm fluxes are bandfilled (if applicable), and

CC 3. source colours are dissimilar to star-forming galaxies (see Gutermuth et al. 2008),

$$\begin{aligned}
[4.5]-[5.8] &< \frac{1.05}{1.2}([5.8]-[8.0]-1), \text{ and} \\
[4.5]-[5.8] &< 1.05, \text{ and} \\
[5.8]-[8.0] &> 1, \text{ and}
\end{aligned}$$

CC 4a. if detected at 24 μm, source has colours $[8.0]-[24] > 2.25$ and $[3.6]-[5.8] > -0.28([8.0]-[24]) + 1.88$, or

CC 4b. if not detected in 24 μm, source has colours $[3.6]-[5.8] > 1.25$ and $[4.5]-[8.0] > 1.4$

CC1 and CC2 exclude infrared sources that were not well detected, such as from bandfilling in the MIPS bands. As discussed before (see §2.3.2) bandfilling uses a

PSF to determine an upper limit flux for a previously undetected wavelength. For example, data from the shorter wavelength bands from IRAC are more sensitive than those from 24 μm or 70 μm wavelengths, so often the longer wavelengths are bandfilled to obtain an upper limit. The IRAC bands, however, have a higher resolution than the MIPS bands, and so the band-filled MIPS fluxes may be contaminated by wings of bright nearby sources (E09). This possibility makes such fluxes from the 24 μm and 70 μm bands unreliable. Therefore, we remove sources with such fluxes from our protostellar lists. For Orion and Taurus, we have no bandfilling information or 70 μm data. As such, we modified CC1 and CC2 and identified sources based on the signal-to-noise for 24 μm and 8.0 μm, rather than using 70 μm. We chose the 8.0 μm band since the sensitivity at the highest IRAC bands is most similar to the sensitivity for the MIPS bands, and we do not have the original maps to determine a better level.

CC3 excludes star-forming galaxies based on the prescription developed by Gutermuth et al. (2008), which detects a growing infrared excess at 5.8 μm and 8.0 μm due to strong PAH emission. In the past, few YSOs have shown strong PAH emission, ensuring that extragalactic sources are identified rather than protostellar sources. We do not include any sources identified as a star-forming galaxy using the prescription from Gutermuth et al. (2008) in our infrared source lists.

CC4a and CC4b select Class 0, I and Flat spectrum sources based on red colours (effectively removing stellar contaminants). If the source in question was well detected at 24 μm then CC4a is used, otherwise we use the IRAC only colours outlined in CC4b, which uses the limit for $[3.6]-[5.8]$ where $[8.0]-[24]=2.25$ (see CC4a) and the $[4.5]-[8.0]$ colour given by Harvey et al. (2007). CC4b does not necessarily select Flat spectrum sources, so we prefer criterion CC4a and use CC4b only when there is no reliable 24 μm flux.

Infrared sources that do not meet all our colour criteria are removed from our infrared source list. The remaining sources in our infrared lists are objects that have good quality detections (CC1 and CC2), have colours dissimilar from star-forming galaxies (CC3), and have suitably red colours (either CC4a or CC4b).

We also attempted to remove broad-line AGN contaminants, using colours outlined in Gutermuth et al. (2008), but found that known young protostars were frequently labeled as AGN by the criteria and were removed from our sample. For example, after using the the prescription from Gutermuth et al. (2008) for the Perseus infrared sources, we misidentified the Class 0 objects HH 211, IC 348 MM, and N1333

IRAS 4B (Froebrich 2005) as AGN, and their respective cores were labeled as starless. Several authors have instead suggested applying a magnitude cut to the infrared sources to remove faint extragalactic contaminants. This cut, however, would vary with cloud properties (ie., extinction) and we want to design a technique without such biases. As such, we have not removed possible broad-line AGNs directly from our sample using the criteria.

Table 3.4 lists the number of infrared sources remaining after we applied our colour criteria. In order to limit the size of our initial infrared source lists, we also determined the SCUBA flux coincident with each infrared source and removed sources that fell outside our submillimetre observations or would otherwise not be associated with a core (that is, $S_{850} < 90$ mJy beam^{-1} at the source position. See §3.2.2 below). Our final source list may still include some galaxy candidates and other suspect objects (we do not apply a c2d designation cut as in the Enoch method). Extragalactic sources, however, are randomly distributed in the sky, and so, are relatively unlikely to be coincident with a SCUBA core. This argument is discussed further in the next section.

Table 3.4 Remaining Objects After Each Cut

Cloud	CC1-2[a]	$S_{850} > 90$	CC3	CC4a-b
Ophiuchus	3474	146	116	73
Taurus	123682	209	198	49
Perseus	3429	159	133	99
Serpens	1443	34	32	25
Orion	23192	902	851	266

---

[a] Quality IR for Ophiuchus, Perseus and Serpens included $S/N \geq 5$ for either 24 or 70 μm and that neither were bandfilled. For Orion and Taurus, we were not given any bandfilling information, nor were we given 70 μm information. For Orion and Taurus, we used $S/N \geq 5$ for the 24 μm and 8.0 μm.

Figure 3.1 shows Spitzer colour-colour diagrams with our infrared sources, following different cuts made to the lists. Again, all sources in Figure 3.1 for Ophiuchus, Perseus, and Serpens were not bandfilled and had a $S/N \geq 5$ at 24 or 70 μm. For Orion and Taurus, the sources had a $S/N \geq 5$ for 8.0 or 24 μm. The solid lines give our MIPS-based colour criteria. The small grey circles represent the cut infrared sources with $S_{850} < 90$ mJy beam^{-1}. The blue crosses represent the infrared sources identified as star-forming galaxies with PAH emission (CC3). The red diamonds represent our final set of infrared sources. From Figure 3.1, it is clear that some star-forming galaxies have [3.6] − [5.8] and [8.0] − [24] colours that match our criteria for protostellar cores. This stresses the importance of removing extragalactic sources as well as the difficulty in identifying them. Although star-forming galaxies have PAH emission in their spectra, there is some overlap using our choice of colours.

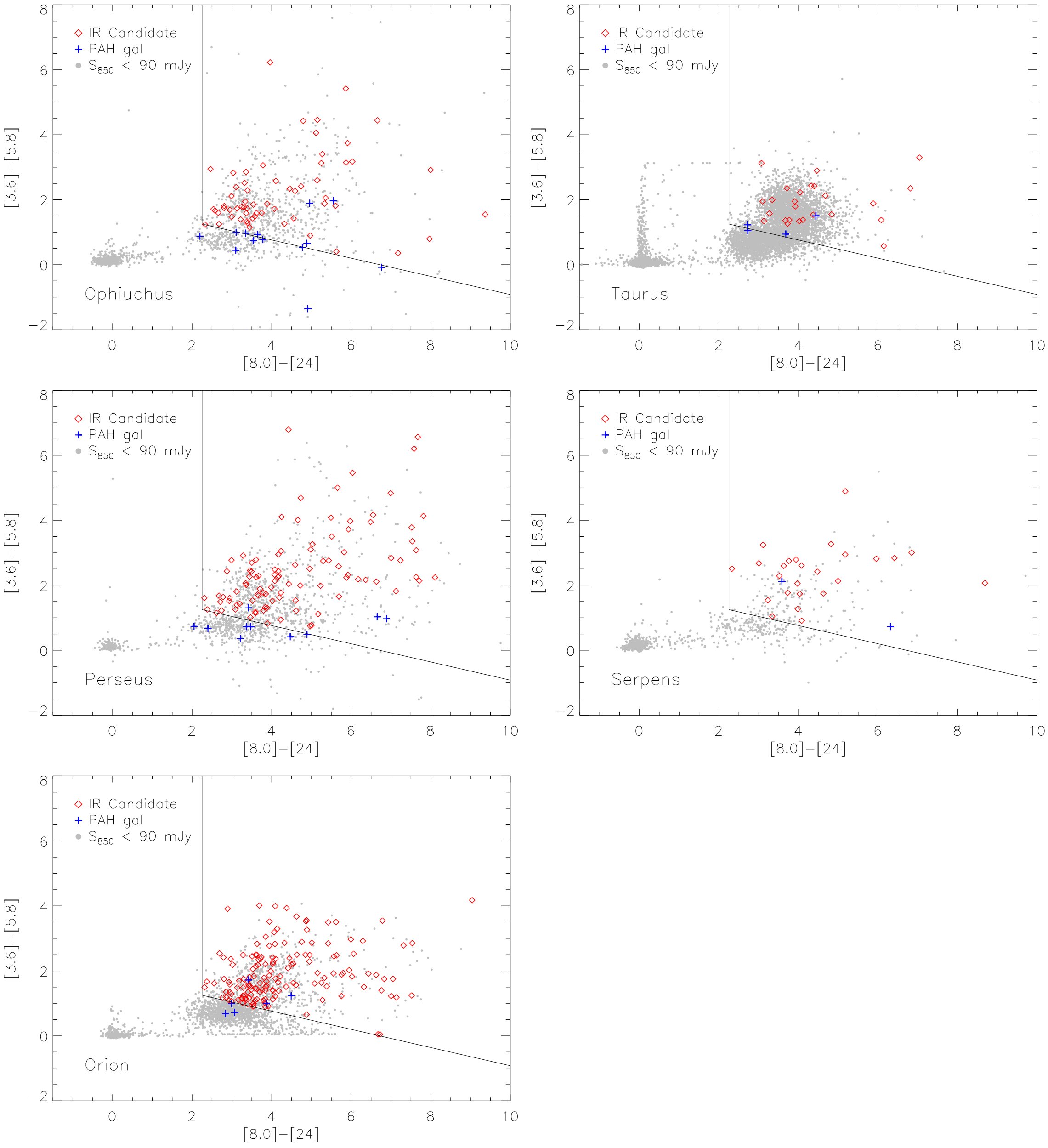

Figure 3.1 colour-colour diagrams for the Spitzer objects in our sample. The red diamonds show the infrared objects that met all our colour criteria. The grey circles are objects that passed the high quality conditions but with $S_{850} < 90$ mJy beam^{-1}. The blue crosses are objects with $S_{850} > 90$ mJy beam^{-1} but also met the colours of a star-forming PAH galaxy.

Our protostar classification technique includes emission at the longer IRAC bands, which are less sensitive and less reliable in regions with many outflows, such as Orion (S. T. Megeath priv. communication). We still believe, however, that the colour criteria given by CC4a and CC4b, which include the 8.0 μm band, well represent young protostellar cores. We tested the reliability of using 8.0 μm emission over 4.5 μm emission in Orion. Using $[4.5] - [8.0] > 1.4$ (from Harvey et al. 2007), we re-defined CC4a as $[4.5] - [24] > 3.65$ and $[3.6] - [5.8] > -0.28([4.5] - [24]) + 2.272$ and then applied these colours to our own Spitzer source list (including the other cuts outlined above) and a protostar list provided by S. T. Megeath (priv. communication). Within the regions observed by SCUBA, we found that there was a $\lesssim 10\%$ variation when using 8.0 μm over 4.5 μm with the protostar list from S. T. Megeath and a $\lesssim 5\%$ variation with our own source list. For the same colours, the two source lists generally differed by $\lesssim 28\%$, which indicates that the main source of uncertainty is from the other cuts to the infrared sources and not the colour choice. For example, S. T. Megeath removed all sources with low S/N at 4.5 μm and potential galaxy contaminants by faint 24 μm magnitudes. For our source list, we removed all sources with low S/N at 8.0 μm and 24 μm and star-forming galaxies using the criteria from Gutermuth et al. (2008).

3.2.2 Flux Contours

One of the main conclusions of J07 was that protostars are found very close to the peaks of submillimetre emission (see Figure 3.2), indicating that the motion of protostars relative to their natal cores is likely small. Figure 3.2 compares the positional offset between infrared sources that met all our colour criteria (see §3.2.1) to their nearest submillimetre core in Perseus. We only considered the nearest infrared source for each core and normalized the separation by the effective radius of that core. We find that the majority of our infrared sources are clustered within the inner half of R_{eff}.

Therefore, it may be superior to consider a given core to be protostellar only if an infrared source is found relatively close to the peak intensity. It is certainly reasonable to assume, for the most part, that protostars will form in the highly concentrated parts of cores which are generally associated with the peak submillimetre flux location (such as $15''$ as given in the Jørgensen method). This could become problematic in instances when many small cores are blended together, at which point, the peak value could be

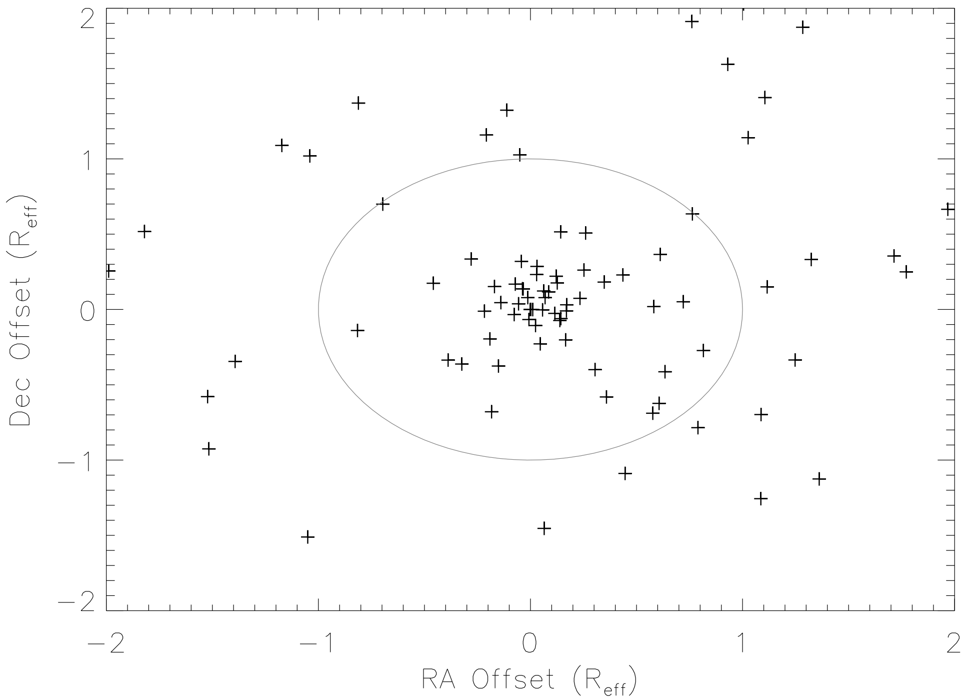

Figure 3.2 Proximity of our infrared sources to the nearest submillimetre core in Perseus. All offsets are normalized to the respective core effective radius (illustrated by the grey circle). We consider only the infrared sources that met our colour criteria (see §3.2.1) and cores that met our submillimetre criteria (see §2.4).

off-centre from all of the individual cores. As well, identifying a core as protostellar using a set angular distance from the peak flux is fairly biased. A fixed physical scale is also a poor choice, because it depends on the cloud distance.

Another important consideration is that cores are typically not circular in projection. For example, the 90 mJy beam^{-1} contour used to define the flux boundary of our SCUBA cores can be very irregular in shape (see Figure 2.2). A circular approximation of the core extent by using its "effective" radius could probe beyond the core in some regions and extend into adjacent cores. This would result in multiple cores that are associated with a single infrared source, as seen with the Enoch method (see §3.1.3).

To ensure that the observed size and shape of the core are considered, we suggest a scheme where the object location is compared to a percentage of the *difference* between the peak intensity and the boundary intensity (90 mJy beam^{-1}). This simple approach (see Equation 3.1) ensures that not only must the infrared source fall within the core boundary, but the source will also be within a certain proximity to the core peak and far enough from the outer edge of the core so that uncertainties in core boundaries are not a factor. This proximity, parameterized by ϵ, will represent a fraction of the core size and will also consider the core shape. Figure 3.3 demonstrates such an implementation, where

$$S_{limit} = S_{peak} - \epsilon(S_{peak} - 90 \text{ mJy}). \tag{3.1}$$

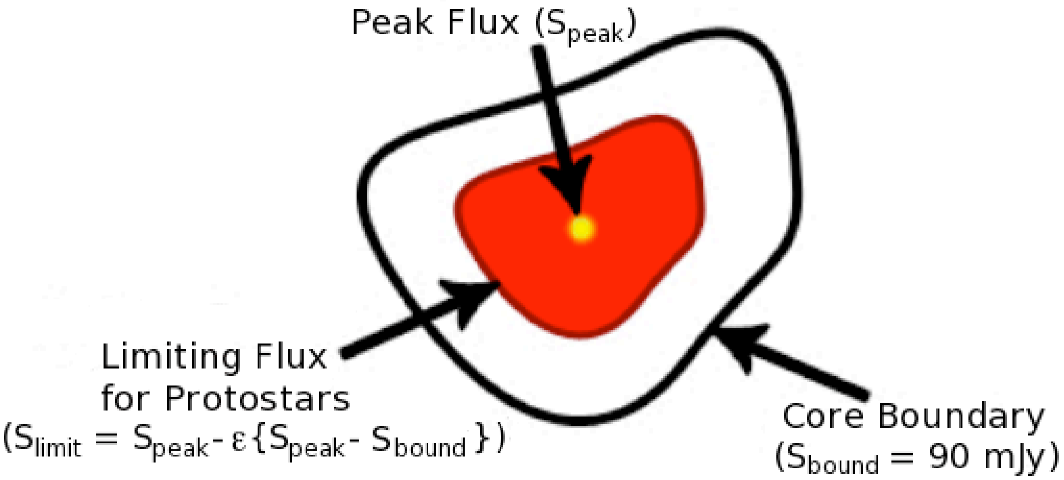

Figure 3.3 Schematic of our classification technique for protostellar cores. An infrared source is considered to be protostellar if it meets the colour requirements outlined by in §3.2.1 and it falls within the red-shaded region illustrated in this figure. The black contours represent the sensitivity boundary of the core (90 mJy beam^{-1}) and yellow circle represents the peak intensity. The dark red contour represents the maximum distance from the central peak for the protostar classification (as given by Equation 3.1).

We set $\epsilon = 0.25, 0.50$, and 0.75 to examine the distribution of infrared sources with flux limit. To reduce the sample to a manageable number, we considered only the cases where a Spitzer source fell within 2R$_{eff}$ of a SCUBA core. We use 2R$_{eff}$ rather than R$_{eff}$ to account for elongated cores, since R$_{eff}$ is essentially an average radial size. For example, a very elongated core may have an infrared source within $\epsilon = 0.75$ along the semi-major axis, which is beyond R$_{eff}$ but in practice not 2R$_{eff}$. Using 2R$_{eff}$ does mean we will initially have a large number of false associations, particularly for larger cores. With this preselection, Ophiuchus had 53 protostellar core candidates (out of 124 submillimetre cores), Taurus had 26 candidates (out of 87), Perseus had 82 candidates (out of 147), Serpens had 11 candidates (out of 15), and Orion had 161 candidates (out of 375).

Each infrared source location was compared to the $\epsilon = 0.25, 0.50, 0.75$ contour levels first using a code and then visually inspected. Cores that did not have an infrared source within the $\epsilon = 0.75$ contour were relabeled as starless. Table 3.5 breaks down how many cores were found when applying the flux contour criteria at each level of ϵ. Unlike Table 3.4, which lists the infrared sources that met our qualitative criteria, Table 3.5 reflects the actual protostellar cores with an infrared source within $2R_{eff}$ of the peak and are considered as *protostellar candidates*. Only cores with an unique infrared source interior to the $\epsilon = 0.75$ are considered protostellar, however.

Identifying unique sources within the $\epsilon = 0.75$ contour was not always clear. For example, some protostellar core candidates were located in filamentary structures or in crowded regions which made the surrounding flux levels much higher (see Figure 3.4). As such, there were several cases where an infrared source fell within the 75% difference contour of two cores. For infrared sources associated with multiple cores, we assigned the source to the nearest core. For cores with multiple infrared sources, we assigned to the core a single, unique infrared source using either the proximity of the source to the peak submillimetre flux or the reddest one.

Table 3.5 Breakdown of Protostellar Core Candidates

Cloud	Candidates	$\epsilon \leq 0.25$	$\epsilon \leq 0.50$	$\epsilon \leq 0.75$	relabeled[a]
Ophiuchus	53	16	25	27	26
Taurus	26	12	17	18	8
Perseus	82	30	41	46	36
Serpens	11	5	7	11	0
Orion	161	45	69	83	78

---

[a] These are the objects that did not meet the positional criteria to be considered protostellar and were subsequently relabeled as starless.

Table 3.6 compares the numbers of protostellar cores identified with either the Jørgensen method, the Enoch method, or our own technique using our SLC-derived core lists. These numbers can be compared to the protostellar core counts given by the respective authors, with their own data, as listed in Table 3.1.

In comparing the results of the classification techniques in various clouds, we find results from our technique are in reasonable agreement with those obtained from the Jørgensen and Enoch methods on the same data. For Ophiuchus and Perseus, our protostellar core numbers fall between those obtained with the other two methods, with the Enoch method finding slightly more and Jørgensen method classifying slightly less. This is not entirely unexpected since we are considering Spitzer sources

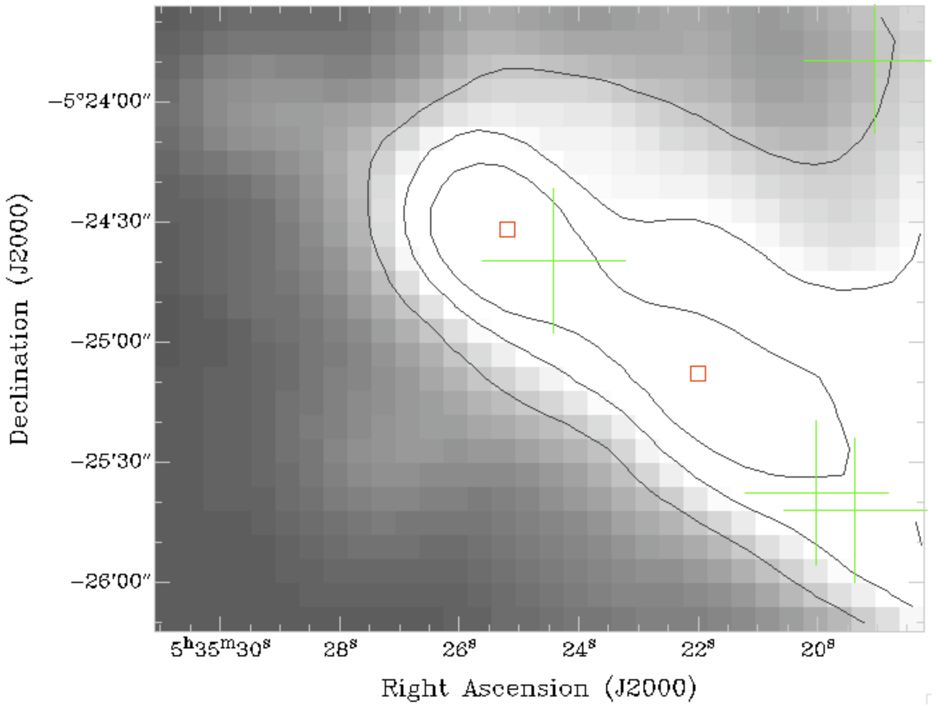

Figure 3.4 Two bright cores in the Orion OMC-1 cloud are given by red squares and three infrared sources within $2R_{eff}$ are shown as green crosses. The contours represent the $\epsilon = 0.25, 0.5, 0.75$ for J053522.0-052508, which has a peak flux 4.47 Jy beam^{-1}. The contours levels are 3.38, 2.28 and 1.19 Jy beam^{-1}. Due to the bright background from other nearby cores, the contours around J053522.0-052508 are elongated along the north-east, south-west direction. Had these contours not been elongated, the two infrared sources would not be contained within $\epsilon = 0.5$. As such, we have identified J053522.0-052508 as starless. The second core (J053525.2-052432) is called protostellar.

over a larger area than Jørgensen et al. used and over a smaller area than Enoch et al. used. For Serpens, it is difficult to compare the results of the three techniques with only 15 cores. Two of the 11 protostellar cores in Serpens identified using our classification scheme are located on a filamentary-like structure and have elongated flux contours. Their infrared sources are located in the elongated regions and may not be associated with the core itself. Filaments and clustered regions will have more extended emission that can affect the contour test.

Although the numbers listed in Table 3.6 are very similar, not all cores are similarly classified as protostellar by each method. Between our method and the Jørgensen and Enoch methods, the number of protostellar cores that match in Perseus are 38 and 39 (out of 46 cores), respectively, and only 18 and 17 match, respectively in Ophiuchus (out of 27 cores). The reasons for these discrepancies were generally related to the infrared selection criteria. For example, in Perseus, J033217.6+304947 was considered protostellar by both the Jørgensen and Enoch methods, but was labeled starless

Table 3.6 Comparison of Protostellar and Starless Core Numbers

Cloud	Method	Protostellar	Starless
Ophiuchus	Jørgensen	25	99
	Enoch	33	91
	this work	27	97
Taurus	this work	18	69
Perseus	Jørgensen	42	105
	Enoch	49	98
	this work	46	101
Serpens	Jørgensen	8	7
	Enoch	7	8
	this work	11	4
Orion	this work	83	292

---

[a] The Orion and Taurus data were not part of the c2d survey and the data given did not include class designations or S/N levels. We could not use the Enoch method, which requires c2d class designations, and so, chose not to do the Jørgensen method for consistency.

with our technique because the associated infrared source (SST033218.0+304947) was identified as a star-forming galaxy.

While our protostellar cores are not in complete agreement with the other two techniques, we believe our technique is still robust. Unlike the Enoch method, we did not select objects with specific c2d designations and instead, we focused on removing sources we believed to be contaminants (e.g., PAH galaxies) using colours. Following our colour and distance criteria, most of our protostellar cores have infrared sources with c2d designations of "YSO candidates" (YSOc) or "red", suggesting that our method is capable of identifying protostellar sources without relying on the c2d designations. This consistency allows us to apply our technique to data observed differently from the c2d clouds (Taurus and Orion).

There are, however, two protostellar cores with c2d designations of "galaxy candidates" (Galc) in Perseus and one each in Ophiuchus and Serpens (for a complete explanation of the c2d designations, see the Final Delivery of Data from the c2d Legacy Project[2]). The Jørgensen method also identifies protostellar cores with infrared sources of unusual designations, though it is more likely in our method. J07 found that the chance of a random encounter was small (only a few in a sample of 100) using an angular size of 15″. With our technique, the angular scale used to iden-

---

[2] http://ssc.spitzer.caltech.edu/legacy/c2dhistory.html

tify objects not only varies (depends on the peak flux value) but is generally larger than 15″. At the SLC pixel scale, 15″ is less than 3 pixels and our contours generally extend to larger angular distances, meaning that the chance of random coincidence from background contaminants is higher for our dataset than for J07's.

3.2.3 Comparison to Other Protostar Lists

Froebrich (2005) compiled a database of young protostars from the literature, and used all available photometry between 1 μm and 3.5 mm to build SEDs and re-classify the sources under a consistent system. This sample includes two objects in Ophiuchus and Taurus, ten objects in Perseus, and eighteen in Orion. For the most part, we identified objects in common as protostellar. Some protostars listed by Froebrich (2005), however, have no corresponding submillimetre core in the SLC Fundamental Catalogue. For example, the known protostar VLA 1623, which is located $\sim 0.5'$ southwest of the bright and very crowded Oph A filament in Ophiuchus, does not have a submillimetre core in the Fundamental Catalogue. This core is listed in the Extended Catalogue, which we do not consider (see §2.3.1). Similarly, four protostars given by Froebrich (2005) for Orion have no associated cores in the Fundamental Catalogue. Such objects may have submillimetre fluxes below our 90 mJy beam^{-1} criteria or their submillimetre flux may be erroneously associated with an adjacent source.

In addition, some known young protostars were misidentified as starless due to no or poor infrared detections with Spitzer. For example, two protostars in Perseus, IRAS 03255+3103 and IRAS 03258+3104, are considered starless with our technique because the corresponding Spitzer source failed to be high quality (failed CC1 or CC2). Two additional protostars in Perseus, SVS 13B and NGC 1333 IRAS 4A, had negative detections in IRAC from bandfilling and thus, failed our colour criteria. In Orion, HH 111 is identified as starless because no Spitzer infrared sources were detected toward it. Two other protostars in Orion, L1641 SMS IV and NGC 2023 MM1, were classified as starless because of non-detections in the IRAC bands. As we only consider Spitzer data for our protostar classification, any non- or poor quality detections by Spitzer are lost to us.

It is clear that even the Spitzer data used for this study were unable to detect all embedded Class 0 objects. Using embedded infrared emission, however, is not the only method of determining protostellar cores. Other signs include outflows, cm wavelength emission or masers (Di Francesco et al. 2007). Knee and Sandell (2000) examined outflows in NGC 1333, identifying five possible Class 0 sources including IRAS 03258+3104 and NGC 1333 IRAS 4A, both discussed before. The remaining three outflows have been properly identified as protostellar.

All of these comparisons suggest that our technique is robust and capable of identifying protostellar cores, provided that Spitzer was able to detect the source. Indeed, we are limited in our ability to classify our SCUBA cores by the areal coverage of Spitzer. To be as unbiased as possible, we did not alter our lists to include known protostellar cores that were labeled starless with our technique. We will consider separately the samples of starless and protostellar cores in the next chapter.

Chapter 4

Discussion

One of the main goals of our work is to examine core mass functions (CMFs) for a variety of nearby clouds. It is preferable to use a common core classification technique for all clouds, although each cloud will have different intrinsic properties (ie., temperature or distance) which may affect observed fluxes at different wavelengths. Using multiple core classification methods, however, may introduce different biases into the CMFs, obscuring possible evolutionary or structural differences between clouds and making comparisons between clouds inaccurate. In the previous chapter, we applied our own classification technique to the five clouds of this study. We will examine here the different properties of the starless and protostellar cores.

4.1 Flux to Mass

To produce the CMFs, we must first estimate the mass contained within the cores. The mass of a SCUBA object can be estimated from its 850 μm flux, temperature, opacity and distance using the formula (Johnstone et al. 2000):

$$M_{clump} = 0.19\ S_{850} \left[\exp\left(\frac{17\ K}{T_d} \right) - 1 \right] \left(\frac{\kappa_{850}}{0.01\ \mathrm{cm}^2\ \mathrm{g}^{-1}} \right)^{-1} \left(\frac{D}{160\ \mathrm{pc}} \right)^{2} M_{\odot} \qquad (4.1)$$

To estimate the dust opacity, we used the mass absorption coefficient at 850 μm (1 cm^2 g^{-1}) from Henning et al. (1995, see their Figure 1). Assuming a dust-to-gas ratio of 100, we obtain $\kappa_{850} = 0.01$ cm^2 g^{-1}. We use this value of κ_{850} for all cores in each cloud, though the opacity can vary by a factor of two (Henning et al. 1995). The dust temperatures and cloud distances used are listed in Table 2.1.

As temperature distributions of cores in these clouds are not yet well known, we assumed a single uniform temperature for all cores in a given cloud. Note, however, that dust temperatures in starless cores should decrease from core edge to core centre as external heating from the interstellar radiation field is increasingly damped (Di Francesco et al. 2007). Protostellar cores, however, may have internal heating which will affect the radial temperature variations, such as a warm centre, cool middle and warm edges. Assuming a constant value of T_d for all cores in a cloud is only a reasonable first approximation until better data are available.

4.2 Starless CMFs

Figure 4.1 shows the starless CMFs for the Ophiuchus, Taurus, Perseus, Serpens, and Orion clouds. These starless cores were identified using our classification scheme outlined in §3.2. To estimate the errors, we varied the temperature in steps of ±1 K up to a 30% uncertainty in T_d, and found the standard deviation across the mass bins generated from the CMFs at these temperatures. We found such standard deviations were similar in magnitude to errors expected from Poisson statistics. In each panel of Figure 4.1, a power-law relationship with a Salpeter slope ($\alpha = -1.35$, see §4.2.1) is shown as the dotted line and seems to trace reasonably well the higher mass ends of the CMFs.

Since we use the same classification scheme for all five clouds, differences in the CMFs should reflect differences between core populations in the clouds. For example, Perseus and Orion contain more massive starless cores than Ophiuchus or Taurus, though many of the highest mass cores in Orion could be misidentifications associated with OMC-1 (see below). Conversely, Ophiuchus and Taurus contain some very low-mass cores. This could be related to cloud distance, as Ophiuchus (125 pc) and Taurus (140 pc) are much closer than the other clouds, but a similar difference is not seen between Perseus (250 pc) and Orion (450 pc).

In terms of overall CMF shape, the Taurus, Perseus, and Orion CMFs show a similar steady increase in from the high-mass end towards a peak and then a steady decrease. Ophiuchus, however, has both a sharp increase and a flatter profile near the peak. In general (but excluding Serpens), the CMFs have a similar “lognormal” appearance, with some differences between them. The Serpens CMF has a very small sample, and we cannot make the same conclusions or comparisons.

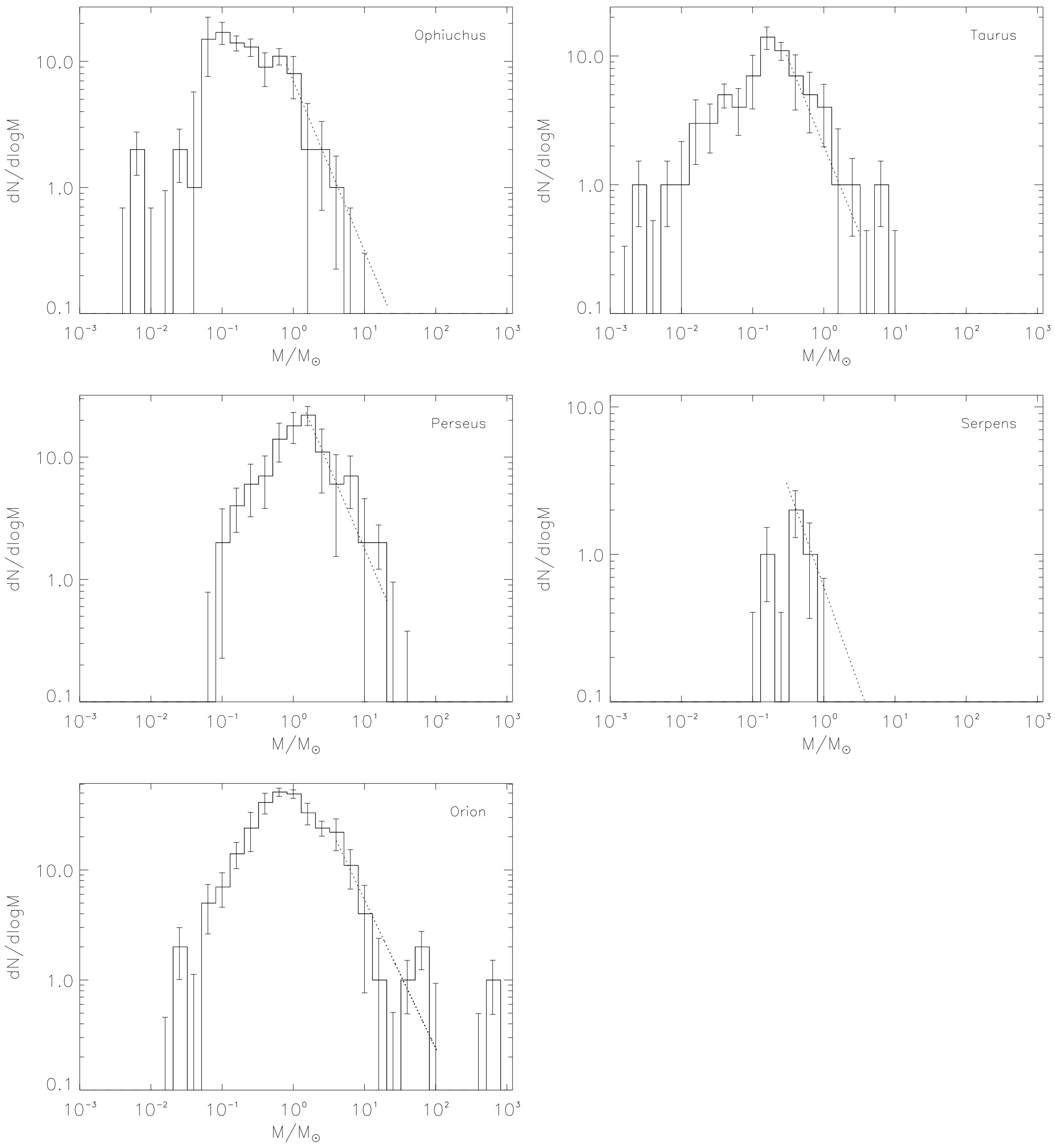

Figure 4.1 CMFs for Ophiuchus, Taurus, Perseus, Serpens, and Orion with Salpeter power-law slopes $dN/d(\log m) \propto m^{-1.35}$. Uncertainties were determined from varying the temperature (see text). Starless cores were identified using our classification technique outlined in §3.2.

For Ophiuchus, Taurus, Perseus, and Orion, the CMF peaks are at roughly 0.1 M$_\odot$, 0.2 M$_\odot$, 1.6 M$_\odot$, and 0.6 M$_\odot$, respectively. The actual peak in the CMF of Ophiuchus and Orion are not as clearly defined as the other clouds. Of these four clouds, Perseus shows the narrowest distribution. Orion has the widest distribution, due to the extreme high-mass extent. With masses on order of $\sim 10^{2-3}$ M$_\odot$, these objects may be too large to be considered a "core" (ie., these objects may be molecular "clumps", which are larger scale structures than cores and form stellar clusters rather than small systems).

Several of the most massive cores in Orion are associated with the OMC-1 cloud, which is the very brightest and most complex region in all 5 clouds studied here. It is possible that a large number of these cores have been misidentified as starless or that these structures are too massive to fall under our definition of a core. Recall that we have defined a core as a dense, compact structure that could form a single star or a small stellar system (ie., binary stars). Figure 4.2 shows the Orion CMF after cores specifically associated with OMC-1 are removed. All cores with a right ascension between $[5^h35^m00^s, 5^h35^m32^s]$ and declination between $[-5°29'00'', -5°17'00'']$ were cut from the sample, resulting in a loss of 12 starless cores from the original Orion CMF. The CMF became thinner and all the high-mass objects ($M > 15$ M$_\odot$) have been removed. It is possible that we are under-estimating the temperature (30 K) in the more active regions of the Orion cloud (like OMC-1). Increasing the temperature of a core by a factor of 2 reduces the mass by a factor of 2.33.

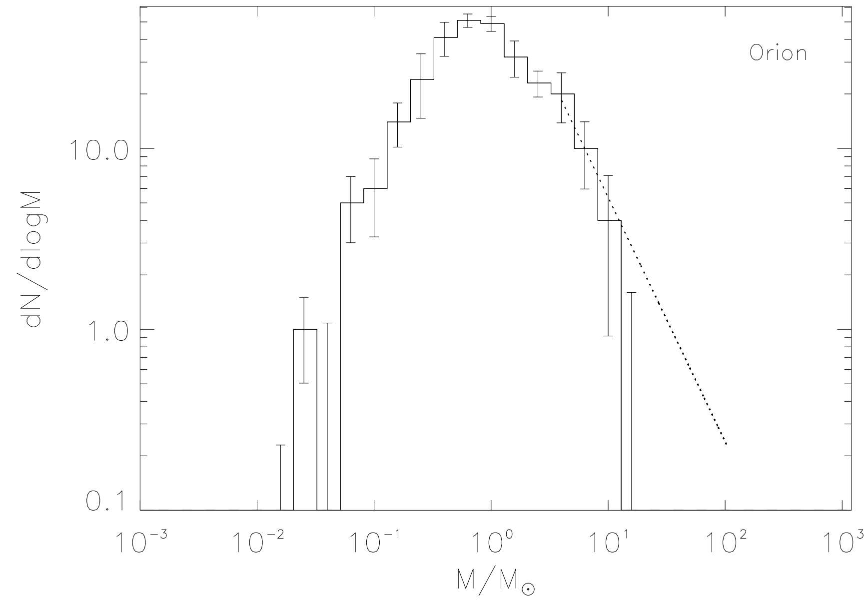

Figure 4.2 Same as Orion in Figure 4.1 but with cores towards OMC-1 removed. We used coordinates of $[5^h35^m00^s, 5^h35^m32^s]$ in right ascension and $[-5°29'00'', -5°17'00'']$ in declination as our boundary for OMC-1.

We have discussed the variety of techniques in classifying a core as protostellar (see §3.1.3 and §3.2.1) and each of these techniques results in a slightly different CMF. Figures 4.3 and 4.4 compare our starless CMFs for Ophiuchus and Perseus, respectively, with the starless CMFs obtained from classifying cores with the Jørgensen and Enoch methods. The high-mass end of the CMF appears the most affected by the classification technique. Note that the Enoch method tends to classify the most massive cores as protostellar. Indeed, a similar result by E08 led them to conclude that higher mass cores evolve more quickly than lower-mass cores. This result is not as apparent with the other two techniques.

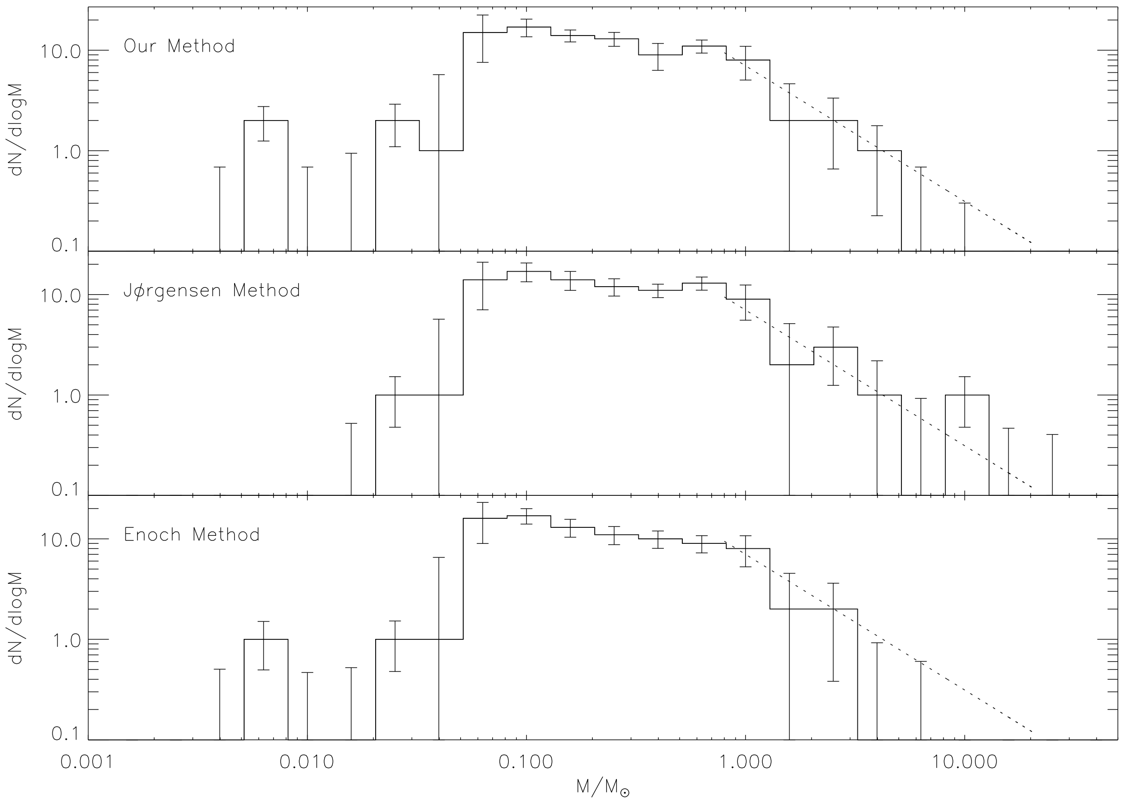

Figure 4.3 Comparison of the resulting CMFs from applying the E08, J07 and our own core classification techniques for Ophiuchus. The dotted line represents a Salpeter power-law slope. Uncertainties were determined by varying the temperature by $\sim$ 30%.

4.2.1 Relation to the IMF

Using an observed luminosity function for nearby stars, Salpeter (1955) found that the "original" mass function (or initial mass function, IMF) was a smoothly varying function that seemed to obey a power-law distribution, $\xi(m) \propto m^{-1.35}$ for 0.4 M$_\odot$ $\lesssim$ M $\lesssim$ 10 M$_\odot$. Here, $\xi(m)$ is defined as $dN = \xi(m) d \log m$, where dN is the number of

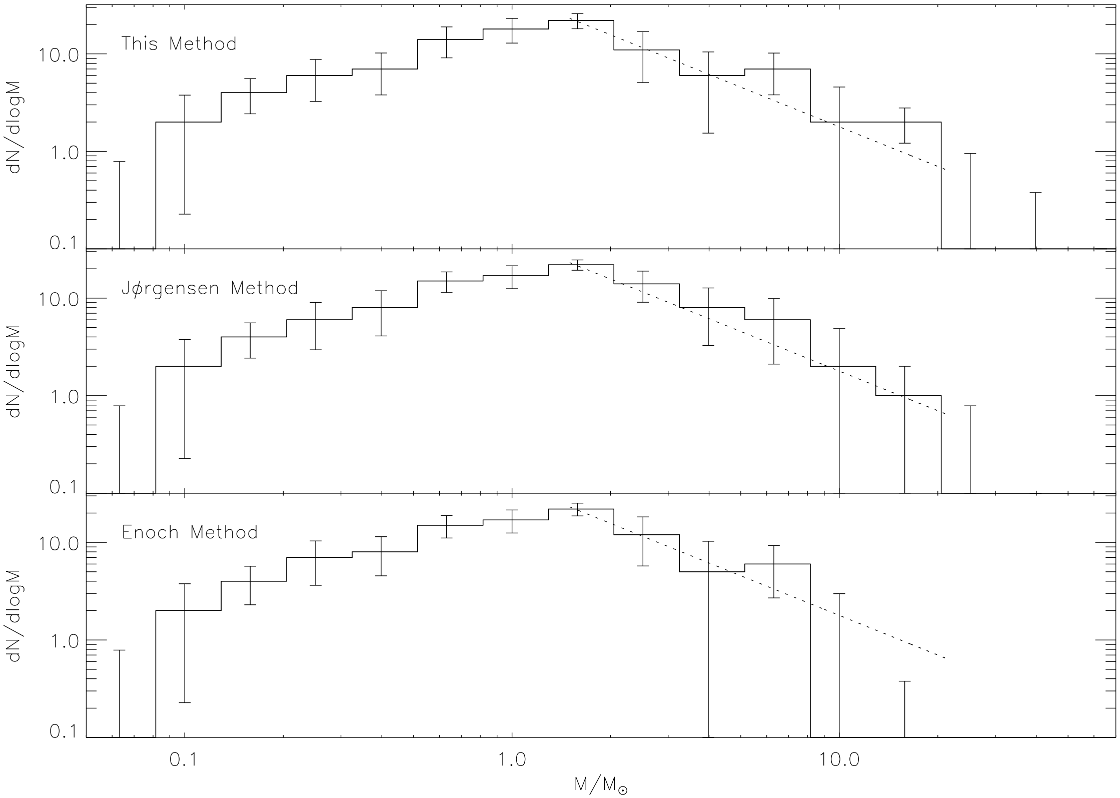

Figure 4.4 Same as Figure 4.3 but for Perseus.

stars of mass m lying between m and $m + dm$ (Warner 1961). Thus,

$$\frac{dN}{d\log m} \propto m^{-1.35} \qquad \text{or} \tag{4.2}$$

$$\frac{dN}{dm} \propto m^{-2.35} \tag{4.3}$$

In Figure 4.1, the Salpeter power-law slope seems to agree with the cloud CMFs. To test this relationship more quantitatively, we determined the best-fit to the high-mass end of each CMF weighing each bin by its uncertainties (weight = $1/\sigma^2$). The resulting best-fits are shown as solid lines in Figure 4.5, where the dotted lines indicate the mass range used for the best-fit. We initially calculated the best-fit parameters using 3 different values of the lower mass limit and then took an average. The upper mass limit is restricted by our uncertainties. Since there are fewer high-mass cores, the measured uncertainties from varying the temperature will produce smaller errors in these bins than more populated mass bins. As a result, the high-mass end is weighed more heavily than bins at mid-mass, which biases our best-fit to steeper slopes. As a result, we chose to use the highest mass bin when $\sigma \sim 1$. For Orion, there is a slight increase in cores at very high masses. We believe this result to be mainly associated with OMC-1 (see Figure 4.2) and so, we do not consider these very high-mass cores in our best-fit slopes in Orion. The Serpens CMF had too few mass bins to calculate a best-fit slope.

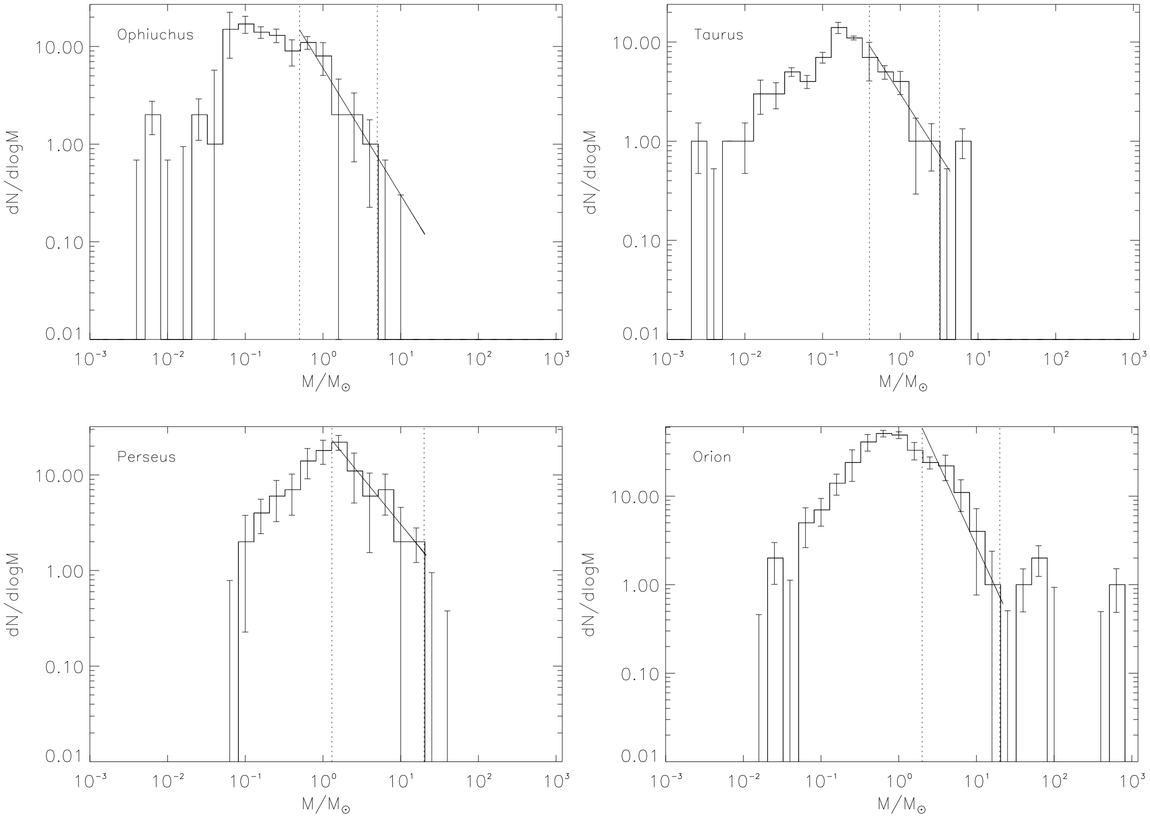

Figure 4.5 Best-fit slopes from ordinary least squares regression. The dotted lines indicate the mass range used to calculate the slope (see Table 4.1).

In determining the best-fit, we calculated six different slopes from six different linear regressions (ordinary least squares Y vs. X, ordinary least squares X vs. Y, ordinary least squares bisector, orthogonal reduced major axis, reduced major-axis, and mean ordinary least squares) using the IDL code from Isobe et al. (1990). For the rest of this thesis, we will consider ordinary least squares Y vs. X, unless specified otherwise. Table 4.1 gives the average best-fit for all clouds except Serpens. For Ophiuchus, Perseus, and Orion, all six regression techniques gave nearly the same values. For Taurus, the six techniques had less agreement. For example, in the range of $0.3 < M/M_\odot < 3$ in Taurus, ordinary least squares regression (Y vs. X) gave a best-fit slope of -1.21 ± 0.08 and the ordinary least squares bisector regression gave a best-fit slope of -1.30 ± 0.11, which is more consistent with a Salpeter power-law.

To be consistent with the other clouds, we list the ordinary least squares (Y vs. X) results for Taurus in Table 4.1.

Table 4.1 Mean Best-Fit Slope

Cloud	Slopes[a]
Ophiuchus	-1.26 ± 0.20
Taurus	-1.22 ± 0.06
Perseus	-0.95 ± 0.20
Orion	-1.85 ± 0.53

---

[a] We constrained our average slope to consider only best-fits with at least 4 mass bins. This resulted in averages from 2 different mass ranges for Taurus and Orion, and 3 different mass ranges for Ophiuchus and Perseus. Serpens is not included because there were not enough mass bins to calculate a least squares fit. The slopes quoted for the clouds were calculated from ordinary linear regression. See text for more details.

While our best-fit slopes tend to fall near the Salpeter value (i.e., within a few σ), some clouds are more Salpeter-like than others. For example, Ophiuchus agrees with a Salpeter power-law within 0.5 σ, whereas Perseus prefers a shallower slope and only agrees within $\sim 1.5\ \sigma$. This means that Perseus deviates from a Salpeter power-law within a confidence of 86.6 % (value of 1.5 σ). A larger, more sensitive set of observations would significantly improve our results.

We also used the Kolmogorov-Smirnov (KS) Test to determine the likelihood that our CMFs were drawn from the same distribution as a Salpeter power-law. Using IDL, we generated a random distribution of masses within the ranges used for the best-fit slopes and compared that to the observed distributions from each cloud over the same range. Unfortunately, the likelihood varied significantly with mass range, suggesting that our samples are too small for testing against a random distribution. A larger and more complete sample is necessary to use the KS test and explore the relationship between the observed CMFs and a Salpeter power-law distribution.

4.2.2 Trends with the CMFs

Our five clouds represent a variety of environments and have very different properties (see §2). Any trends between these properties with the starless CMFs could reveal information about star formation across these environments. We compared the CMF peak mass and the best-fit slope against cloud distance, cloud mass, cloud extinction peak, core line widths, core temperature, core extinction peak, and number of cores in the sample. We found very few correlations, in spite of our range of cloud properties. Figure 4.6 shows six of the fourteen trends that we examined.

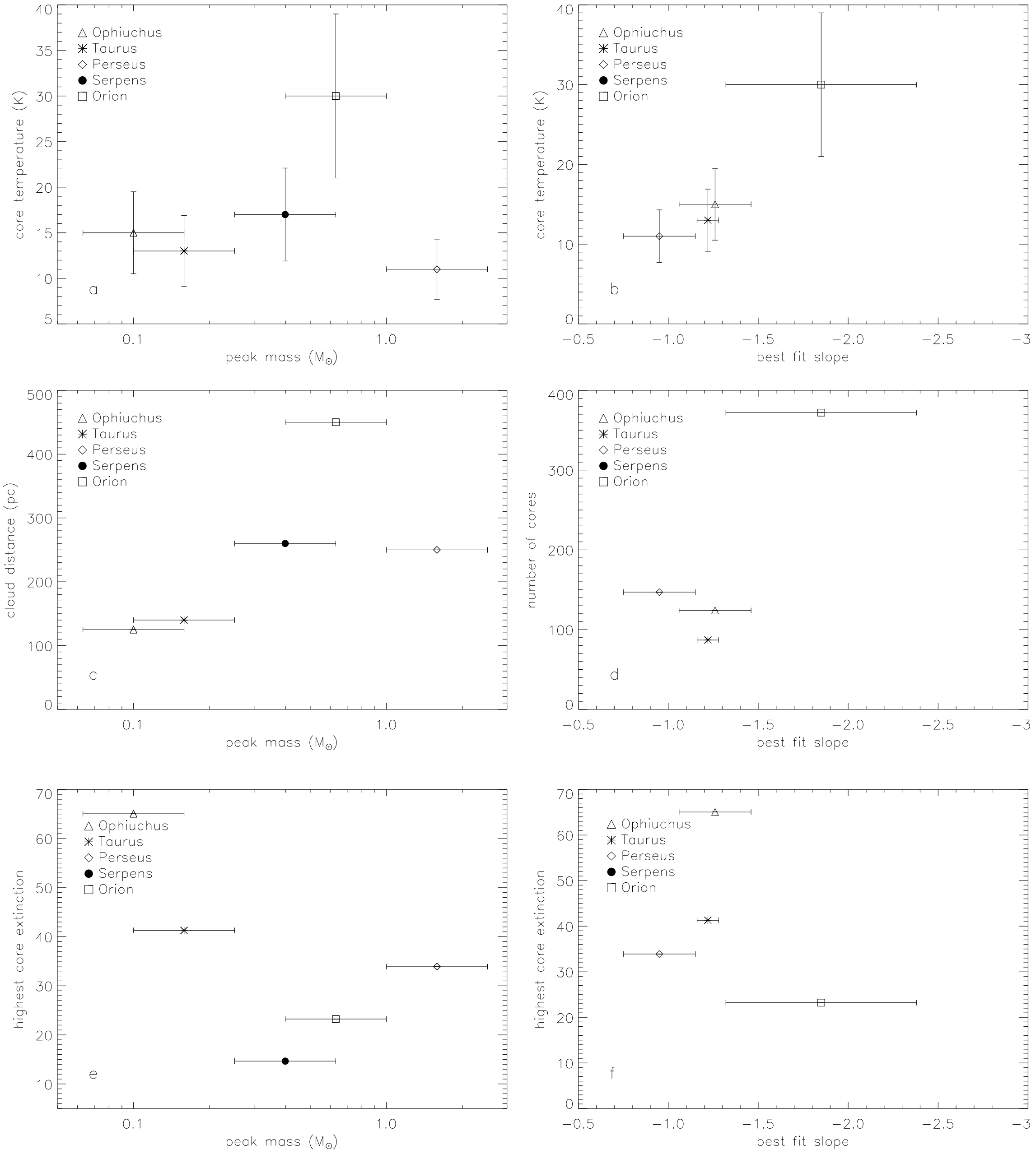

Figure 4.6 Examples of the fourteen comparisons between cloud or core properties with CMF properties. Peak mass was defined as the most populated mass bin in the starless CMF. The best-fit slope is given in Table 4.1. Serpens had too few points to determine a linear best-fit slope.

For example, Figure 4.6a shows no correlation between core temperature and peak mass, whereas Figure 4.6b (core temperature with best-fit slope) shows the strongest case for a potential trend. The correlation in Figure 4.6b, however, depends greatly on the slope of Orion, which has the largest measured uncertainty. A trend between core temperature and best-fit slope would imply that there is no universal, constant power-law distribution for CMFs. A more extensive study with more clouds is necessary to test this relationship.

Figure 4.6c shows a possible trend between cloud distance and CMF peak mass. A slight positive relation between these properties may reflect our imposed threshold of 90 mJy beam^{-1}. The mass contained within 90 mJy beam^{-1} should vary with distance and temperature (see Equation 4.1), however, there is no strong correlation with temperature (Figure 4.6a). A weak trend in Figure 4.6c could also result from unresolved lower mass cores appearing as higher mass cores in more distant clouds. This would suggest, however, a shallower best-fit slope with distance, which we do not observe.

Figure 4.6d shows no correlation between best-fit slope and the number of cores, however, it appears that the uncertainties in the best-fit slopes seem to increase with the number of cores. With a larger sample, we would expect the uncertainties to decrease with number. The uncertainties are based on temperature variations and not Poisson statistics. Figures 4.6e and 4.6f show no obvious trends of either peak mass or best-fit slope with the highest extinction level.

4.3 Protostellar CMFs

In identifying starless cores with our classification technique, we also identify the protostellar core population. Figure 4.7 shows the protostellar CMFs for each cloud and their relation to the high-mass IMF slope. The protostellar cores in Figure 4.7 were identified using our classification technique. We initially assumed the same temperatures as with the starless CMFs. Uncertainties in the protostellar CMFs were measured in the same manner as the starless CMFs.

The protostellar CMFs do not show quite the same "lognormal" shape as the starless CMFs, though there are fewer numbers of protostellar cores than starless. Also, all protostellar CMFs seem to be systematically shifted to slightly higher masses than the starless CMFs. The Orion and Perseus protostellar CMFs peak at nearly the same mass (~ 2.5 M$_\odot$ for the protostellar CMFs and ~ 1 M$_\odot$ for the starless CMFs). The Ophiuchus and Taurus protostellar CMFs also peak at higher masses (~ 0.5 M$_\odot$ for both) than their starless distributions, though at lower masses than the CMF peaks of Perseus and Orion.

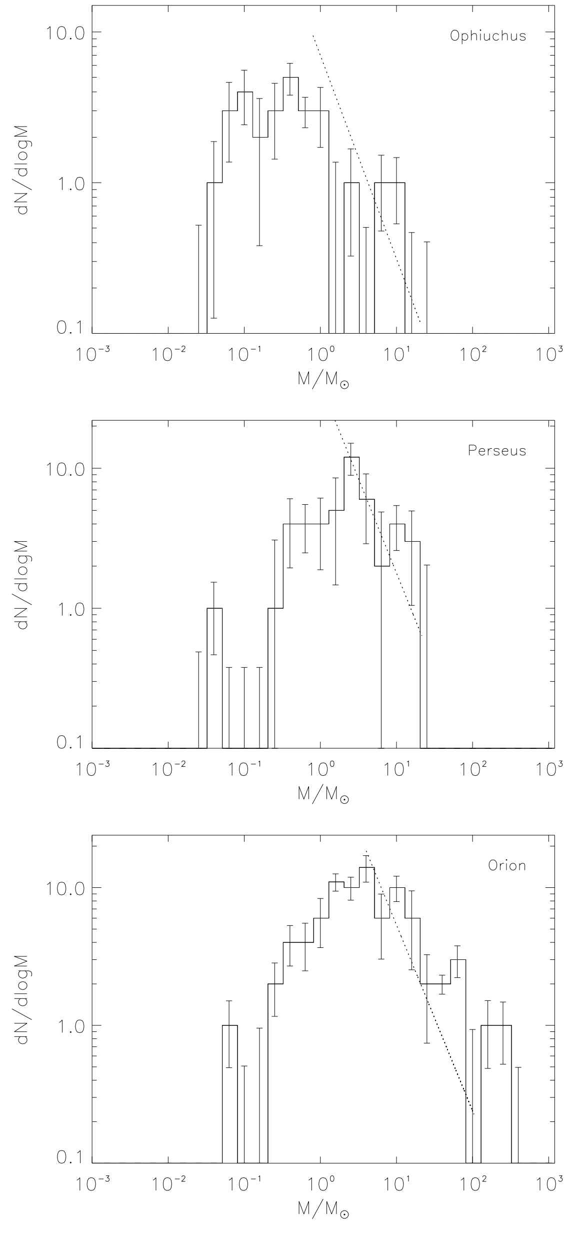

Figure 4.7 Protostellar CMFs for all five clouds with Salpeter power-law slopes $dN/d\log m \propto m^{-1.35}$. Uncertainties were determined from varying the temperature up to 30%. We assume the same temperature as the starless cores.

Are protostellar cores intrinsically more massive than starless cores? In Figure 4.7, we assumed that the protostellar cores have identical dust temperatures to the starless cores. The protostellar cores, however, may be heated internally and thus, have slightly higher temperatures (e.g., see E08). A higher protostellar core temperature will reduce the core mass and possibly remove the apparent discrepancy between the starless and protostellar CMFs. Indeed, for dust temperatures of 15 K, an increase of 1 K would reduce the mass by a factor of ~ 1.2.

We tested the effect on the protostellar CMFs by raising the temperature in steps of $\Delta T_d = 1$ K. We determined our final protostellar core temperature based on fitting the width and peak of the protostellar CMF to the starless CMF. Raising the temperature in this way assumes an insignificant mass loss from the envelope to the protostar and that the protostellar and starless CMFs should extend over the same mass ranges. In the end, we found that a protostellar core temperature of 20 ± 2 K was a good fit for Ophiuchus and 17 ± 2 for Taurus, 15 ± 1 K for Perseus, 67 ± 3 K for Serpens, and 59 ± 3 K for Orion. Thus, the protostellar core temperatures in Ophiuchus, Taurus, and Perseus should increase by a factor of ~ 1.3, the temperatures in Serpens should increase by a factor of ~ 4, and the temperatures in Orion should increase by a factor of ~ 2.

The substantial increase in protostellar temperature for Orion (59 K over 30 K) could be attributed to an underestimation of the starless core temperature. Unlike the Ophiuchus, Perseus, Serpens, and Taurus clouds, the Orion molecular cloud is undergoing massive star formation, which is often associated with “hot” cores (Kurtz et al. 2000). Hot cores are very dense and can have temperatures of > 50 K (Cesaroni et al. 1994). Figure 4.2 shows the Orion CMF with the high-mass star forming OMC-1 region removed. The resulting CMF is considerably more “lognormal” and consistent with the other clouds. This suggests that the cores in OMC-1 may be of unusually high-mass or at a higher temperature. The similar increase in temperature for Serpens (67 K over 17 K), however, may reflect merely the small number of starless cores in our sample.

Figure 4.8 illustrates the protostellar CMFs at their new temperatures in relation to the starless CMFs. For each protostellar CMF in Figure 4.8, with these temperature changes, we find no over abundance in protostellar cores at higher masses relative to starless cores, suggesting that higher mass cores do not necessarily evolve more quickly than lower mass cores.

For the rest of our analysis, we will compare protostellar and starless core properties using the same dust temperatures (see Table 2.1) and not the increased temperatures shown in Figure 4.8.

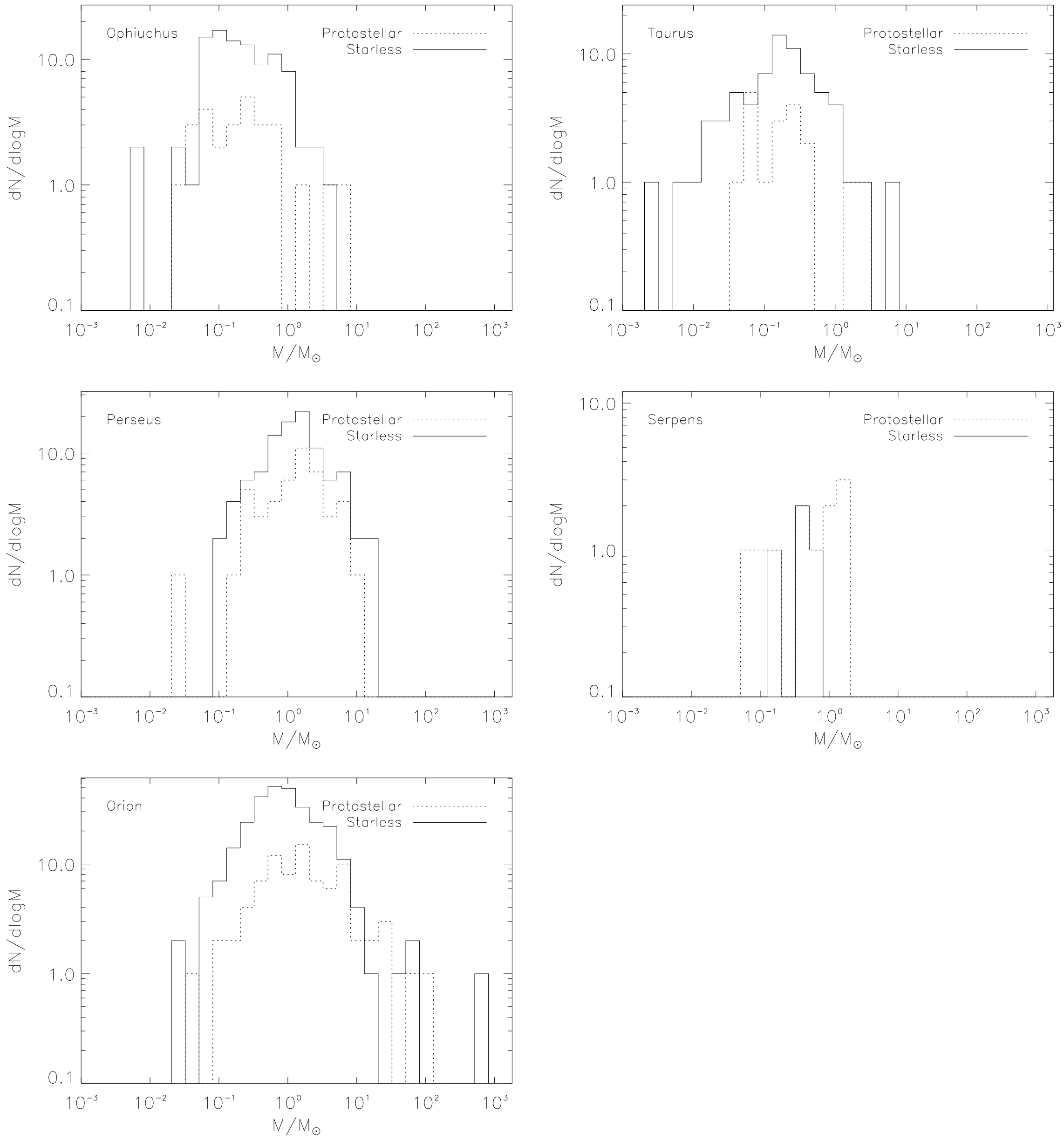

Figure 4.8 Protostellar (dotted) and starless (solid) CMFs for all five clouds. The temperatures for the protostellar CMFs have been adjusted to match the width and peak of the starless CMF. The temperatures used are 20 K, 17 K, 15 K, 67 K, and 59 K for Ophiuchus, Taurus, Perseus, Serpens, and Orion, respectively. The respective starless core temperatures are 15 K, 13 K, 11 K, 17 K, and 30 K.

4.4 Core Environments

Figure 4.9 compares the masses and sizes of the cores in our five clouds. The radii used in Figure 4.9 are the observed sizes, which are the true sizes convolved with the SLC beam (and then truncated according to the 90 mJy beam^{-1} threshold). The

SLC beam is approximated as a Gaussian with a FWHM of $\theta_b = 22.9''$ (Di Francesco et al. 2008). Due to this finite resolution, all cores will have smaller true sizes than observed, with less extended cores more affected than more extended ones. We have not deconvolved the sizes of our cores in Figure 4.9.

For all the clouds in our sample, core mass and radius are well correlated with a positive trend. For Serpens, the protostellar cores appear to have higher masses and larger sizes than the starless cores. This trend, however, may be a reflection of the small sample, since the other clouds do not show the same results. Though the range of masses for cores of a given size is quite restricted due to sensitivity (dot-dashed line), we note interesting departures in Figure 4.9 at high masses, where mass begins to increase faster than size.

In Figure 4.9, the sensitivity limit (dot-dashed line) is from the 90 mJy beam^{-1} threshold. The SCUBA observations are limited by the detector sensitivity, resulting in a minimum observed mass in a beam. For a constant surface density, the limiting mass is $\mathrm{M} = \pi R^2 \sigma$, where σ is the mass surface density in units of $\mathrm{M}_\odot$ AU^{-2} (converted from 90 mJy beam^{-1}). In log-space, this becomes:

$$\log M = 2 \log R + \log(\pi\sigma) \tag{4.4}$$

The coefficients for the threshold equation are listed in Table 4.2 for each cloud. The surface density, σ, is only dependent on the dust temperature as any distance dependence falls out during the conversion to physical units. In Figure 4.9 most of the points sit very close to the threshold sensitivity for the observations (represented by the dot-dashed lines) and detected cores should not go below this boundary.

Table 4.2 Threshold Functions[a]

Cloud	Slope	Intercept
Ophiuchus	2.000	- 8.129
Taurus	2.000	- 8.021
Perseus	2.000	- 7.885
Serpens	2.000	- 8.217
Orion	2.000	- 8.570

---

[a] Functions are in the form of $\log M = a \log R + b$, where a is the slope and b is the intercept ($\log \pi\sigma$).

Figure 4.10 gives the distributions with A_V for the five clouds, separated in terms

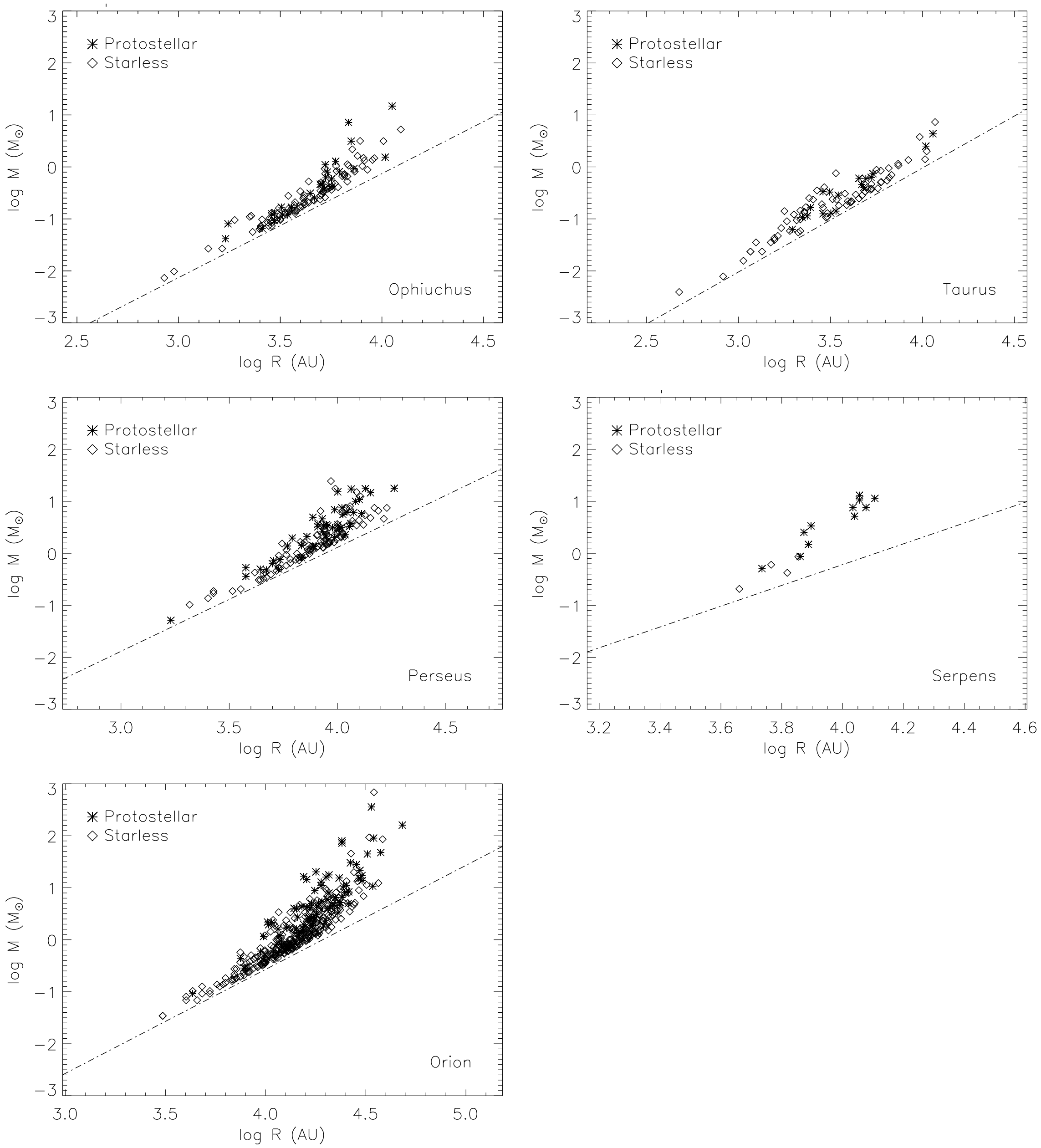

Figure 4.9 Comparison of core radius and core mass for the five clouds in our sample. Protostellar cores were classified using our technique outlined in §3.2. We assume a constant dust temperature (see Table 2.1) for cores within each cloud regardless of whether the cores are protostars or starless. The threshold sensitivity of 90 mJy beam^{-1} is shown as a dot-dashed line.

of protostellar (solid lines) and starless (dashed lines) cores. The histograms are binned to $\Delta A_V = 4$ for all five clouds to ensure all bins are well populated. In general, the distributions are broadly similar. Note that for Ophiuchus and Taurus, all the cores with the highest extinction are starless. This result could be due to the observational difficulty in detecting the most highly embedded protostars, though we are likely insensitive to the highest extinctions in the more distant clouds. For Orion and Perseus, some protostellar cores are found in their highest extinction regions and for Serpens, all high extinction cores are protostellar. Many of these objects are also high in mass (see Figure 4.11), particularly those cores associated with OMC-1. Also note that the low extinction cores in Ophiuchus are exclusively starless, and in the other clouds the majority of low extinction cores are starless.

As can be seen in Figure 4.10, the protostellar and starless core distributions peak at similar A_V. For example, the protostellar and starless core A_V distributions peak at $A_V \sim 25$ magnitudes for Ophiuchus. This is significantly higher then the peaks of these distributions in the other clouds, though this could be related to distance. Again, due to lower resolution, it is more difficult to measure high extinctions in more distant clouds like Orion than in closer clouds like Ophiuchus. Table 4.3 compares the starless and protostellar core extinction peaks separately for the five clouds in our sample. Serpens is the only exception to the similar peaks in A_V, though that is likely related to its small sample size.

Table 4.3 Extinction Peaks for Starless and Protostellar Cores

Cloud	A_V Distribution Peak (mag)	
	Starless	Protostellar
Ophiuchus	25	25
Taurus	13	8
Perseus	8	11
Serpens	12	25
Orion	8	8

Figures 4.11 and 4.12 compare extinction with core mass and extinction with core size, respectively. The two distributions are scattered for Ophiuchus, Taurus, Perseus, and Orion, with no strong trends seen. Serpens may show trends of increasing mass and size with extinction and evolutionary state (ie., starless to protostellar), though the other clouds with larger samples do not reveal the same. For the other clouds, the protostellar and starless cores have wide ranges of mass and size and these are

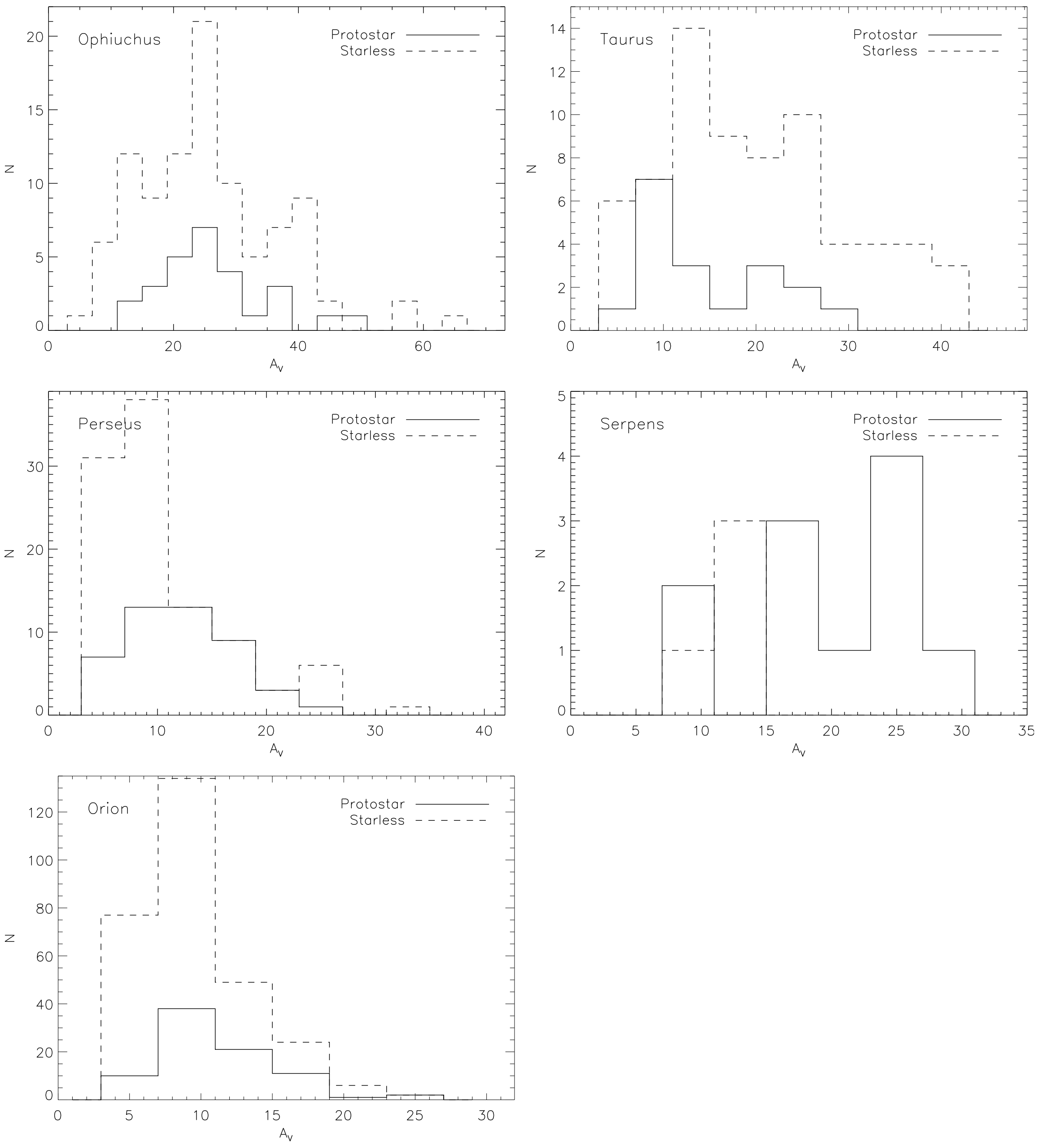

Figure 4.10 Distribution of extinction for each core in our five clouds. Cores were classified into starless or protostellar using the technique we developed (see §3.2). Cores were binned to $\Delta A_V = 4$.

found at all extinctions. While there is a strong correlation between core size and mass (see Figure 4.9) for all five clouds, no obvious relations of these quantities with extinction are seen given a good sample size.

4.5 Predicted CMFs

While a revolutionary instrument, SCUBA was limited in its ability to sample the dense core populations in nearby star-forming clouds. Typically, SCUBA observed previously known regions of active star formation (e.g., L1688, Johnstone et al. 2000). In general, these regions were located in high extinction levels within the cloud (e.g., Johnstone et al. 2004) and very large fractions of these clouds, particularly at low extinctions, remain unmapped (see Figure 2.3). As a result, the CMFs derived from SCUBA Legacy map data (see §4.2 and Figure 4.1) likely do not represent all cores within their respective clouds.

SCUBA-2 will be the successor continuum mapping instrument to SCUBA on the JCMT. With superior sensitivity and efficiency, SCUBA-2 will be able to map nearby clouds with improved flux sensitivity and speed, allowing for more complete samples of their core populations. The SCUBA-2 Gould Belt Legacy Survey (GBLS; Ward-Thompson et al. 2007b) will map all 15 star-forming molecular clouds within 500 pc (observable from Hawaii), a significant improvement in cloud sampling over SCUBA, which only well sampled Ophiuchus and Perseus to a sensitivity of $\sim$ 30 mJy beam^{-1}. These observations will include a $\gtrsim 400$ deg^2 shallow survey (to a depth of 10 mJy beam^{-1} at 850 μm) in regions of $A_V \geq 1$ and an additional $\sim$ 120 deg^2 for smaller clouds and isolated star forming regions positionally associated with the Gould Belt. There will also be a deeper survey in regions of $A_V \geq 3$ (down to $\sim$ 3 mJy beam^{-1} at 850 μm) for $\sim$ 64 deg^2. With these sensitivities, we will be able to well detect core masses within 500 pc down to substellar masses (Ward-Thompson et al. 2007b). These data will allow us to obtain a robust CMF and solidify its possible similarities to the IMF and role in the determination of stellar mass, construct a less ambiguous approach to classifying cores, and constrain the lifetimes associated with star formation.

We can predict what the SCUBA-2 observations could reveal using the SCUBA data analyzed here over certain mass ranges and following certain assumptions. Of course, since SCUBA-2 will have improved sensitivity, lower mass cores will be more easily detected and this regime will be better populated than before. Indeed, since

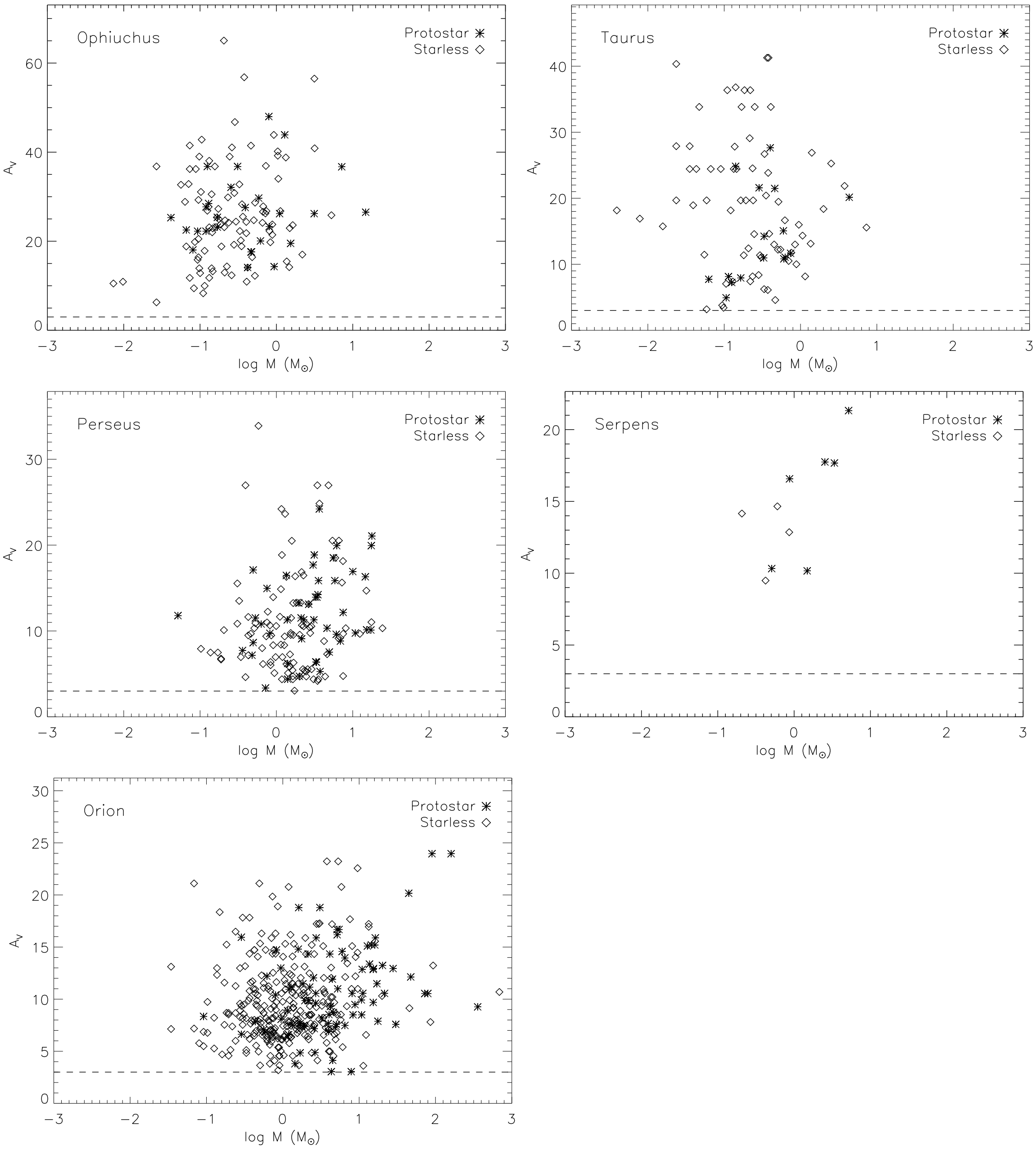

Figure 4.11 Comparing core extinction and mass for starless and protostellar cores. Cores were classified using the technique outlined in §3.2. The dashed line illustrates the $A_V = 3$ limit we imposed on all cores.

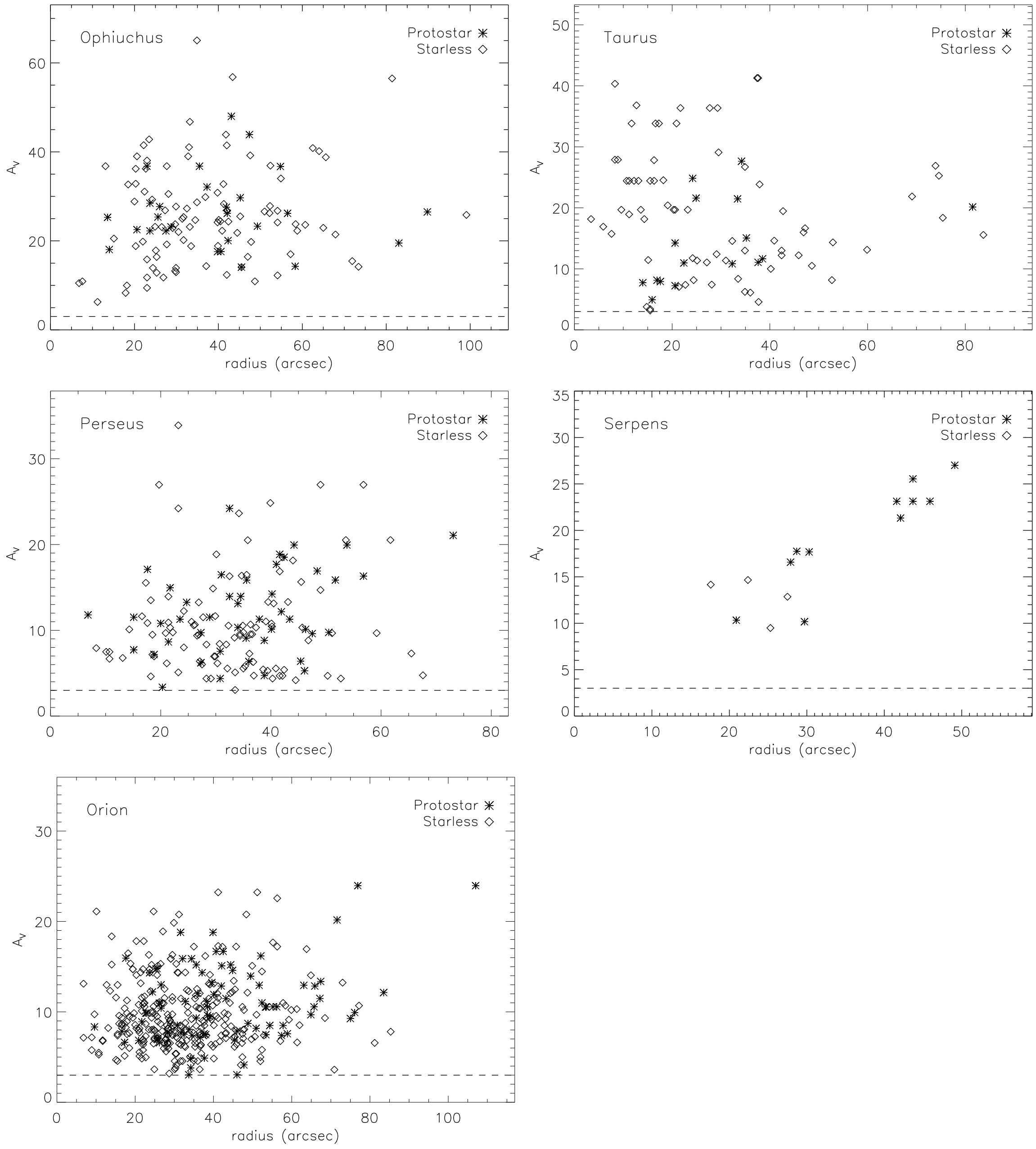

Figure 4.12 Same as Figure 4.11 but comparing core extinction and size.

the low-mass regime cannot be predicted from the SCUBA data alone, we caution that our predicted CMFs are only applicable in the higher mass regime, where our data are more complete.

Predicted CMFs can be created by assuming the observed CMFs trace the incidences of cores for the unobserved regions of each cloud. Using these data, the observed areas and the total areas of the cloud, we can predict whole cloud CMFs. Furthermore, we can explore possible dependencies on core incidence with cloud environment by predicting CMFs that will be compared with future SCUBA-2 data. For example, we can probe if core incidence depends on extinction. If we compile CMFs over small extinction ranges (ie., $\Delta A_V = 4$), we can extrapolate those mass distributions to the unobserved regions of the cloud. We chose $\Delta A_V = 4$ to ensure that the extinction ranges are well populated. For a given A_V range, the predicted number of objects ($N_{A_V,pred}$) is given by the observed number in that range ($N_{A_V,obs}$) multiplied by the ratio of entire cloud area to the observed cloud area at that A_V range.

$$N_{A_V,pred} = N_{A_V,obs} \frac{\Omega_{A_V,cloud}}{\Omega_{A_V,scuba}} \tag{4.5}$$

where $\Omega_{A_V,cloud}$ is the area of the whole given cloud that falls within a given A_V range and $\Omega_{A_V,scuba}$ is the area within the same extinction range actually observed by SCUBA.

4.5.1 Finding the Observed Area

The fraction of each cloud observed by SCUBA was different from cloud to cloud. For example, only one relatively small region of Serpens was observed in contrast to the rather more extensive mapping of Perseus. This puts Perseus at an advantage over Serpens for having a more complete sample (within a given flux sensitivity). Thus, taking into account the area of observations can help us compare the results between these clouds.

To determine the areas of each cloud observed by SCUBA, we counted the number of non-zero pixels in the SLC maps. Each SLC map is $1.2' \times 1.2'$ in extent and several overlap with other maps. To account for this overlap, images that contain duplicated areas were edited to remove sections in common and set an accurate reading of the mapped area. Edits were made by “blanking” the duplicated regions, such as the boxed region in Figure 4.13. Since the location of the overlap is measured by eye, there is some small uncertainty associated with each edit (e.g., < 500 pixels). Given that the maps typically have observed areas on order of $\sim 10^5 - 10^7$ pixels, the uncertainties in editing maps will not have a significant impact.

One additional complication is that the Scorpius and Monoceros clouds have projected locations near Ophiuchus and Orion, respectively. As such, the 2MASS extinction maps of Ophiuchus and Orion contain sections of Upper Scorpius and Monoceros R2. Since we wish to extrapolate the observed regions of each Ophiuchus and Orion to account for unobserved regions using an A_V-dependent technique, we removed contamination from these regions by "blanking" the Scorpius and Monoceros sections from our extinction maps (see cyan regions in Figure 2.3).

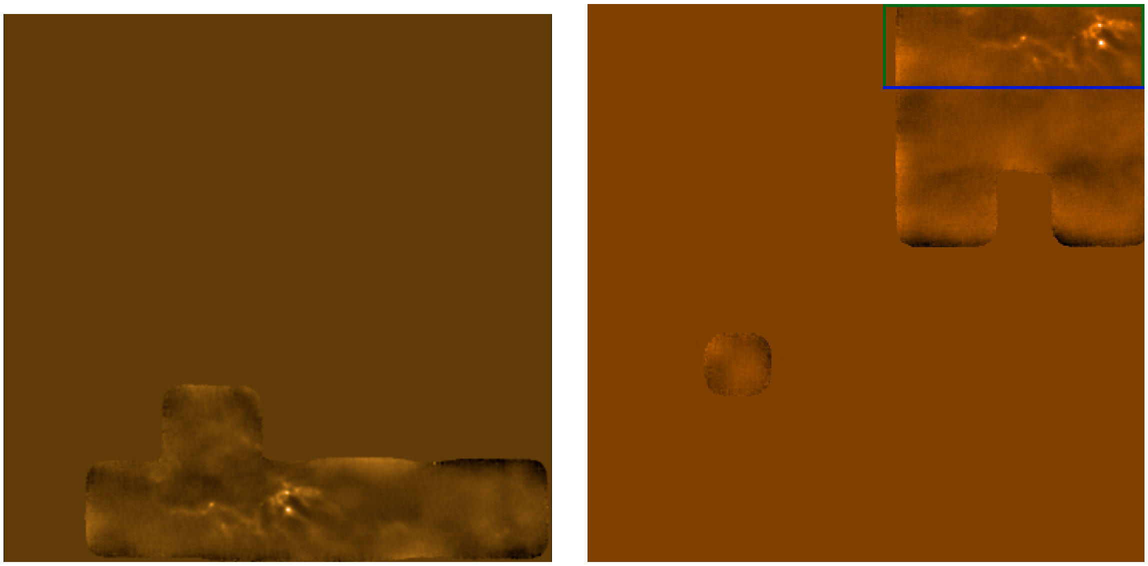

Figure 4.13 Two separate SCUBA maps in Perseus illustrating the overlap in observations. The right image shows a box containing an overlap with the left image. The blue line represents the side of the overlap region that must be determined from the left image. The green lines represent the edge of the map and thus, are independent of the left image.

Another complication was counting the number of pixels that SCUBA observed. The 850 μm maps are not simple square field observations (see Figure 4.13) but quite irregular in shape. The unobserved areas in each SLC map are represented by a default value of zero and appear as flat monochromatic regions. An IDL script was used to determine the number of non-zero pixels for each edited SLC image. Table 2.2 lists the total areas observed by SCUBA for each cloud. Tables 4.4 - 4.8 give the areas observed by SCUBA within a given extinction range for each cloud. Note that these areas refer to SCUBA maps from the Fundamental Catalogue only (see §2.3.1). Tables 4.4 - 4.8 also list the areas of each A_V range in deg^2 associated with each cloud, as derived with the 2MASS data.

Table 4.4 Observed Area for Ophiuchus

Area	A_V Range															
deg^2	3 - 7	7 - 11	11 - 15	15 - 19	19 - 23	23 - 27	27 - 31	31 - 35	35 - 39	39 - 43	43 - 47	47 - 51	51 - 55	55 - 59	59 - 63	63 - 67
SCUBA	1.21	0.525	0.143	0.0787	0.0616	0.0633	0.0339	0.0189	0.0092	0.0080	0.0040	0.0028	0.0012	0.0020	0.0004	0.0008
2MASS	8.89	0.785	0.164	0.0816	0.0628	0.0640	0.0344	0.0188	0.0092	0.0080	0.0040	0.0028	0.0012	0.0020	0.0004	0.0008

Table 4.5 Observed Area for for Taurus

Area	A_V Range									
deg^2	3 - 7	7 - 11	11 - 15	15 - 19	19 - 23	23 - 27	27 - 31	31 - 35	35 - 39	39 - 43
SCUBA	0.4101	0.2413	0.0782	0.0348	0.0341	0.0293	0.0064	0.0028	0.0028	0.0020
2MASS	13.2231	0.9650	0.3762	0.2724	0.1700	0.0853	0.0228	0.0085	0.0071	0.0021

Table 4.6 Observed Area for for Perseus

Area	A_V Range							
deg^2	3 - 7	7 - 11	11 - 15	15 - 19	19 - 23	23 - 27	27 - 31	31 - 35
SCUBA	1.539	0.3613	0.0756	0.0310	0.0252	0.0169	0.0026	0.0018
2MASS	4.289	0.4446	0.0864	0.0396	0.0342	0.0189	0.0063	0.0018

Table 4.7 Observed Area for for Serpens

Area	A_V Range						
deg^2	3 - 7	7 - 11	11 - 15	15 - 19	19 - 23	23 - 27	27 - 31
SCUBA	0.0091	0.0243	0.0070	0.0067	0.0012	0.0009	0.0004
2MASS	8.4253	1.0291	0.1141	0.0321	0.0056	0.0009	0.0013

Table 4.8 Observed Area for Orion

Area	A_V Range					
deg^2	3 - 7	7 - 11	11 - 15	15 - 19	19 - 23	23 - 27
SCUBA	0.6379	0.4164	0.1300	0.0391	0.0119	0.0022
2MASS	12.819	1.5022	0.4144	0.1611	0.0767	0.0300

4.5.2 Predictions

The purpose of this exercise is to build CMFs that will predict the core distributions over an entire cloud with minimum peak fluxes of 150 mJy beam^{-1} and size limits of 90 mJy beam^{-1} following our original criteria for identifying cores (see §2.4). The 2MASS observations (Figure 2.3) show the clouds extend over areas much larger than these observed by SCUBA, and so the CMFs derived from SCUBA data partially represent the true cloud CMFs. The predicted CMFs, however, will be extrapolations of these CMFs over the unobserved regions of each molecular cloud.

For each cloud, Figure 4.14 shows the observed CMF (dotted histogram), predicted CMFs (solid histogram) assuming some dependence of core incidence with extinction (ie., A_V-dependent; see equation 4.5), and the predicted CMFs (dashed histogram) assuming no dependence on extinction (ie., A_V-independent). For the A_V-independent case, we scaled up the observed CMFs according to the ratio of entire cloud area (at $A_V > 3$) to cloud area observed by SCUBA.

Overall, the predicted CMFs are generally similar in shape, but have large differences in number. Table 4.9 lists the numbers of observed starless cores and the numbers of predicted starless cores using the above assumptions. Note again that our analysis is biased in favour of cores that could have been detected by SCUBA. Low-mass objects, particularly diffuse sources, are more difficult to detect and may be removed with our core definition limits. Since we cannot accurately probe the low-mass end of the observed CMFs, our predicted CMFs are also incomplete in this regime and the numbers quoted in Table 4.9 are lower limits to the actual expected core statistics using this method.

Table 4.9 Predicted and Observed Starless Core Numbers

Cloud	Observed	A_V-dependent	A_V-independent
Ophiuchus	97	109	455
Taurus	69	467	1239
Perseus	101	171	242
Serpens	4	91	776
Orion	292	2317	3476
Total	563	3155	6188

There is a significant increase in the number of predicted cores obtained from the A_V-independent extrapolation over the numbers from the A_V-dependent case. This increase suggests that most of the cores exist at higher extinction though the majority

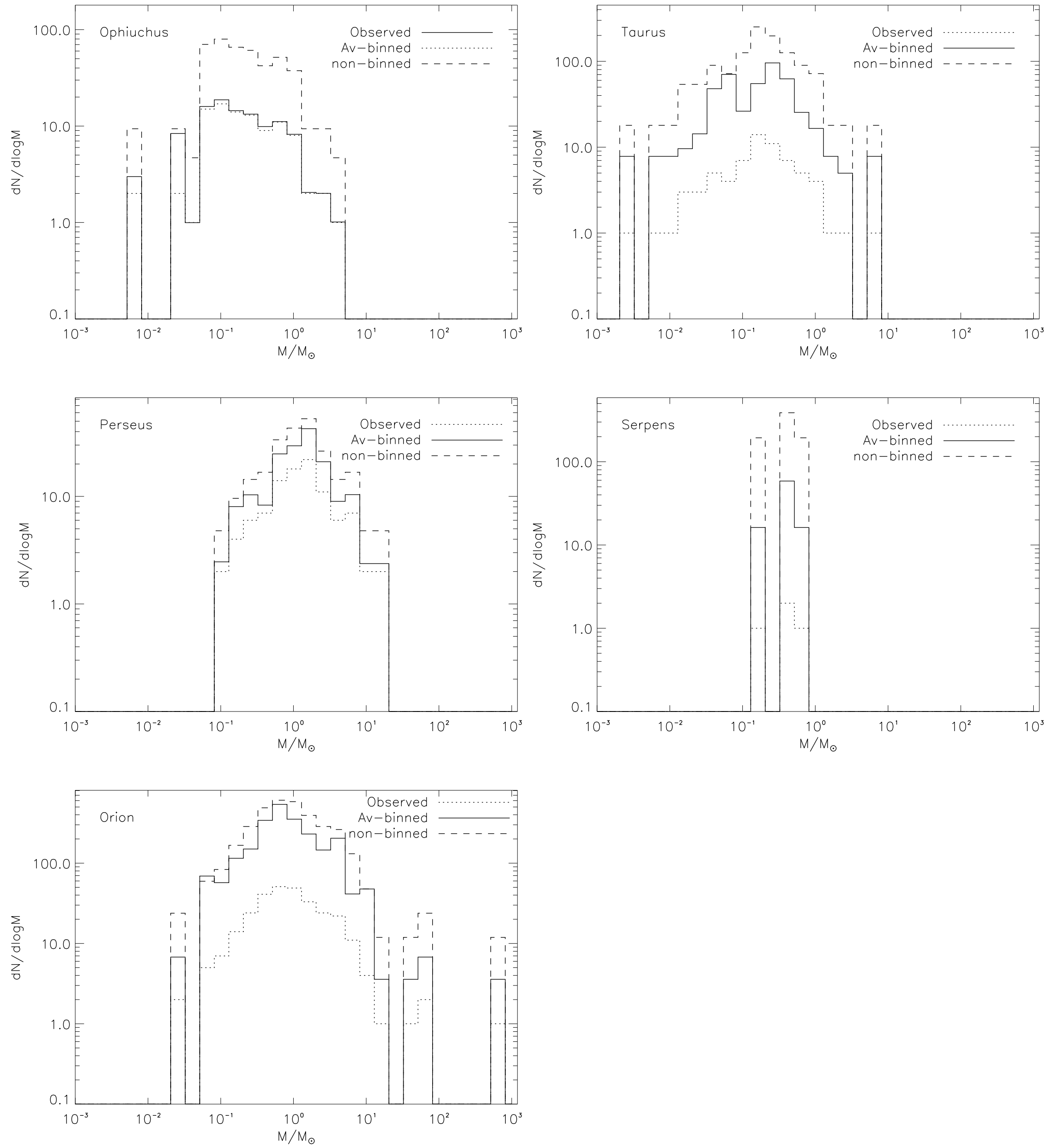

Figure 4.14 Predicted A_V-dependent CMFs are shown in solid histograms for all five clouds with the observed CMFs as dotted histograms and predicted A_V-independent CMFs as dashed histograms. Extinction ranges for the A_V-dependent CMFs of all clouds were $\Delta A_V = 4$.

of the cloud exists at lower extinction. The shapes of the predicted A_V-dependent CMFs look very similar to the observed CMF. The peak mass is identical in all clouds, except Taurus which peaks at the adjacent mass bin.

The predicted CMFs in Figure 4.14 were made assuming we accurately knew the mass of each core based on flux and temperature. This assumption, however, is greatly inaccurate as uncertainties from the instruments, temperature gradients, distance measurements and cloud opacities will all affect the core mass. We attempted to simulate this uncertainty by replacing core populations in every mass bin of the observed CMFs with a Gaussian of the same area, to represent the possibility of a given core populating the wrong bin. We set the FWHM of our Gaussian replacements to be the width of our initial mass bins ($\log M/M_\odot = 0.2$, but note that this makes the FWHM vary with mass bin) and then summed all the Gaussians. With these replacements, we computed predicted CMFs with the previous assumptions that core incidence has some or no dependence on extinction.

Figure 4.15 shows the predicted CMFs assuming an A_V-dependent extrapolation and Figure 4.16 shows the predicted CMFs for the A_V-independent extrapolation. Included in both figures are the cumulative Gaussian replacements for each of the mass bins and the linear least squares best-fit slopes to the cumulative histogram. The grey dot-dashed lines indicate the mass range used to determine the linear regressions for the best-fit slopes. Serpens does not contain enough histogram mass bins to calculate its best-fit slope. The errors in the bin populations were determined by varying the temperature with the observed CMFs as before.

Table 4.10 gives the best-fit slopes for the predicted CMFs using the histograms or cumulative Gaussians over the same mass range. The six linear regression techniques were less consistent than with the observed CMFs, so we caution using these fits to represent the high-mass slope. As well, the best-fit slopes depend significantly on the mass range for the linear regressions and the individual errors can be quite large ($\sim 50\%$). For Orion, these uncertainties are much larger.

Table 4.10 Predicted CMF Slopes

Cloud	A_V-dependent		A_V-independent	
	Histogram	Gaussian	Histogram	Gaussian
Ophiuchus	−1.26	−1.39	−1.30	−1.38
Taurus	−1.27	−1.31	−1.14	−1.21
Perseus	−1.55	−1.20	−1.22	−1.02
Serpens	···	−2.43	···	−1.89
Orion	−1.93	−1.22	−1.57	−1.18

Though the slopes in Table 4.10 were calculated using the same linear regression method and over the same mass range, there are differences between the slopes in the A_V-dependent and A_V-independent cases. In general, the A_V-dependent slopes are steeper than the A_V-independent slopes. The slopes also differ between predicted

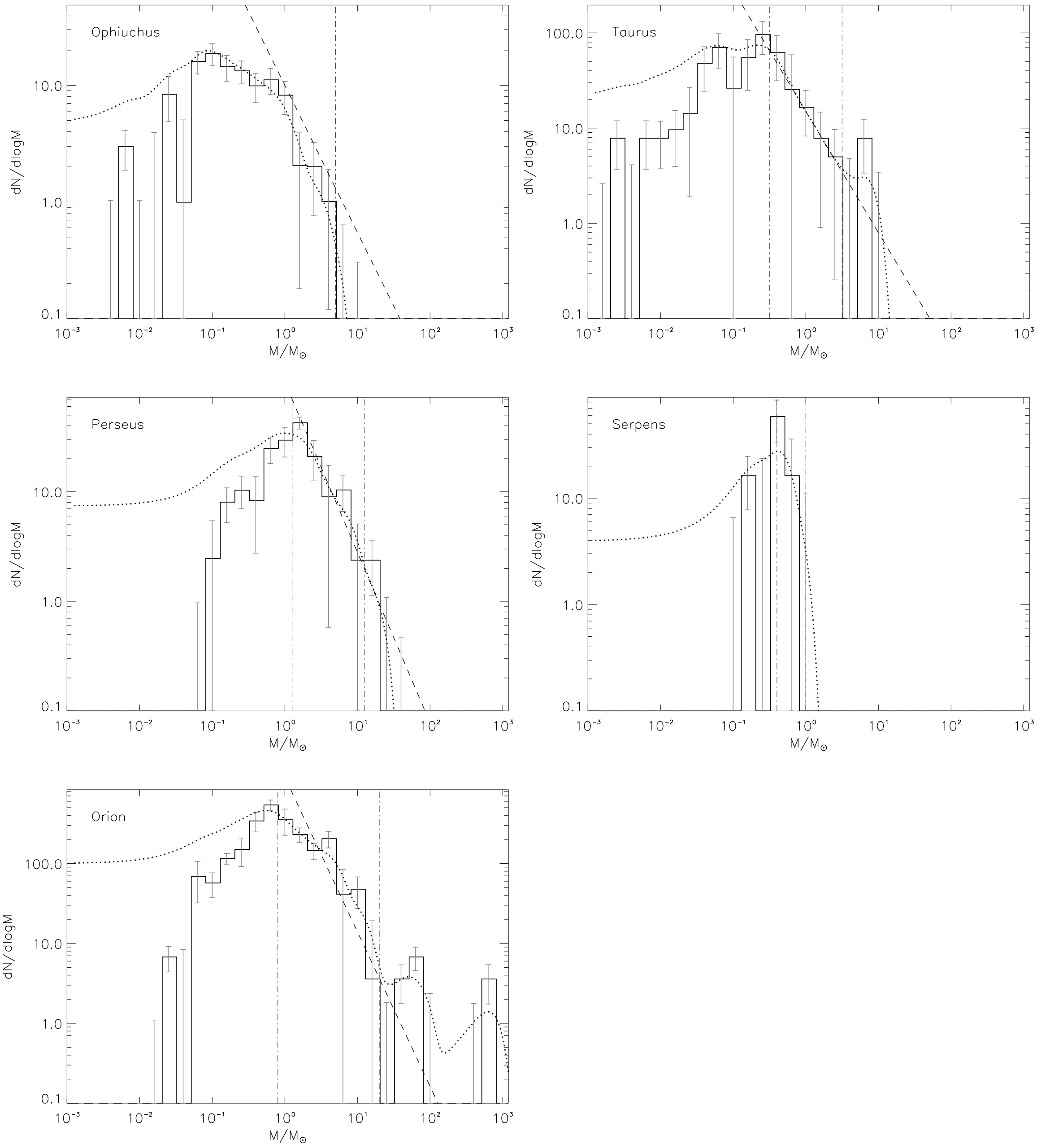

Figure 4.15 Predicted CMFs for all five clouds using the A_V-dependent extrapolation method. The uncertainties were measured by finding the standard deviation from changes in the temperature. The dashed lines represent the linear least squares best-fit using the mass range shown by the dot-dashed lines. Also included is the cumulative Gaussian from replacing the counts in the mass histograms at each A_V range by a Gaussian. See text for more details.

CMFs determined by extrapolating histograms or Gaussian replacements, though neither methods appears to produce consistently steeper slopes. These slopes also show some differences from the observed CMF slopes in Table 4.1. For example,

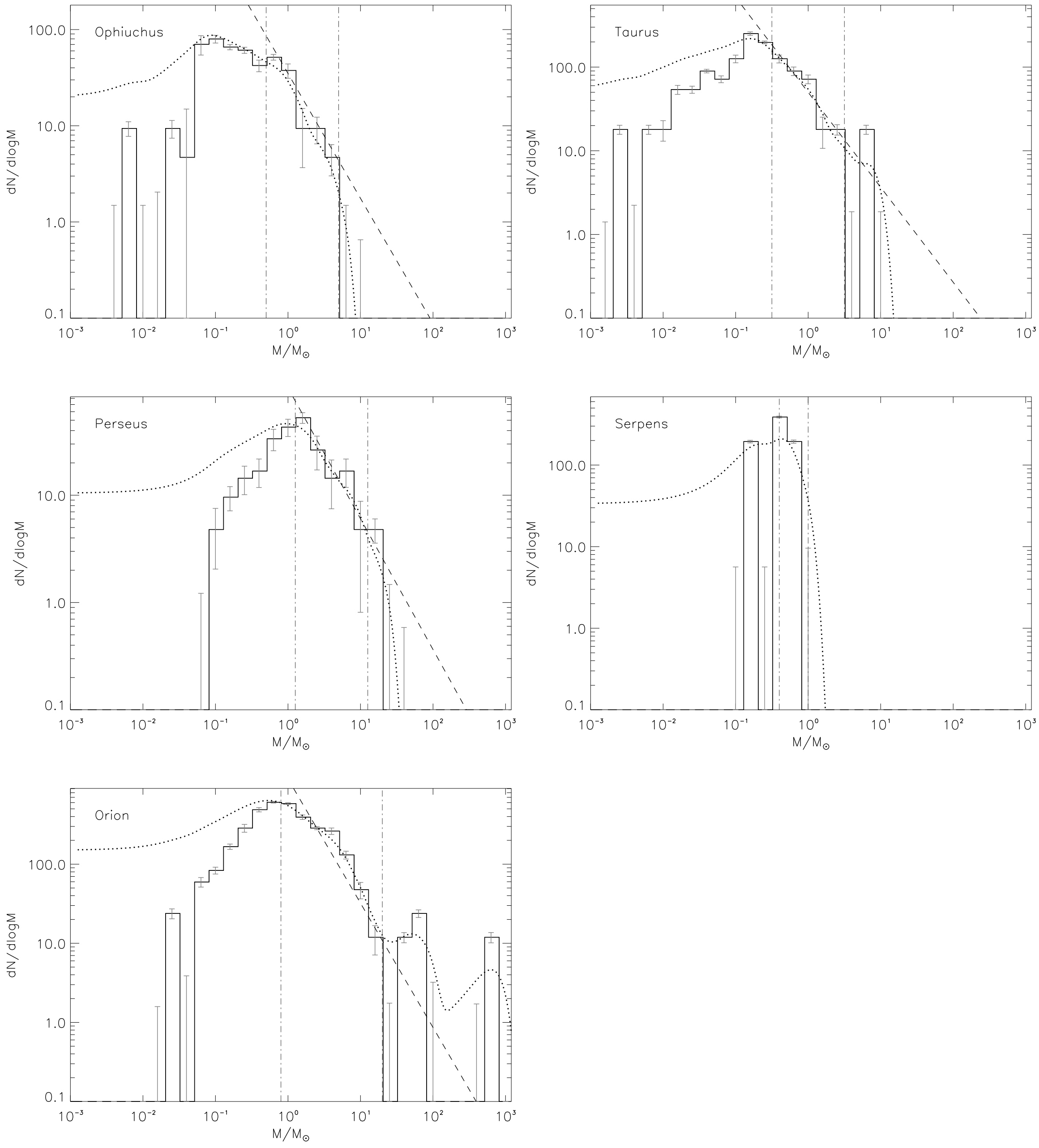

Figure 4.16 Same as Figure 4.15 but for the predicted CMF that does not make any assumptions on core incidence with A_V.

the observed CMF slope in Perseus is much shallower than any of the predicted slopes. Again, the uncertainties associated with these slopes are large. Within these uncertainties, the predicted slopes also appear Salpeter-like. We anticipate comparing these predictions with CMFs derived from actual data over the entirety of these clouds in the very near future.

4.6 Future Work

Comparisons between the CMF and stellar mass distributions have been limited by the small extents and low sensitivities of submillimetre observations (Di Francesco et al. 2008). A much firmer characterization of the relation between starless cores, YSOs, and stellar mass will be achieved with forthcoming instruments. As described above, SCUBA-2, a new camera on the JCMT by early 2010, will be used as part of the JCMT Gould Belt Legacy Survey (Ward-Thompson et al. 2007b) to map submillimetre emission across nearby molecular clouds at greater sensitivities and over wider areas than before to obtain a more robust determination of their CMFs (Holland et al. 2006). SCUBA-2 will also sample roughly twice the clouds that SCUBA surveyed with greater resolution than the SLC data.

In addition, SPIRE and PACS, two far-infrared cameras on the Herschel Space Observatory were launched in May 2009, and like SCUBA-2, they will map clouds in far-infrared and submillimetre wavelengths with good efficiency and more sensitivity than previous cameras. With the high angular resolution of PACS ($8''$ at 110 μm) and SPIRE ($17''$ at 250 μm) these instruments will perform deep surveys of star-forming regions (André and Saraceno 2005).

These three cameras will cover 75 μm - 850 μm with 7 bands. The data can be used to reveal simultaneously the temperature and column density structures of cores by providing constraints to radiative transfer models (André and Saraceno 2005, Ward-Thompson et al. 2007b). In addition, we have developed here a scheme to identify protostellar cores from starless cores. This step is necessary to remain unbiased in our analysis of star formation, and our new method will be applicable to all data from these forthcoming surveys.

Large surveys such as the JCMT GBLS will provide a wealth of data for a number of star-forming regions and allow for better comparisons between these clouds. For example, we can smooth the data to a constant linear resolution or apply appropriate flux limits to analyze each star-forming region with the same mass sensitivity. Using these new instruments and classification techniques such as our own, our understanding of cores and their formation and evolution into stars, will profoundly advance.

Chapter 5

Conclusions

We have used data from the SCUBA Legacy Catalogue, 2MASS, and Spitzer (Legacy, Guest Observer and Guaranteed Time Observations) to produce relatively unbiased starless and protostellar CMFs using a new classification technique. We applied this technique to the Ophiuchus, Taurus, Perseus, Serpens, and Orion molecular clouds. Indeed, this is likely the most extensive study of the starless core populations in nearby molecular clouds to date. For example, we have examined 5 unique clouds in a uniform manner. As well, previous studies of Orion and Taurus have been limited in infrared detections (ie., only IRAC observations, Nutter and Ward-Thompson 2007) or coverage (ie., only TMC-1, Nutter et al. 2008), respectively. We believe our classification method is robust and that our CMFs can be compared to illustrate differences in the clouds. Unlike previous techniques, our classification method considers the core shapes and does not rely on a fixed physical or angular scale. As well, by using the same classification technique, we were able to explore the differences in each CMF, examine trends between clouds, and make predictions for future surveys.

Our starless CMFs agreed with a Salpeter power-law within errors, though there were some differences between the clouds. Assuming a constant dust temperature for all cores in a given cloud, our best-fit slopes were -1.26 ± 0.20, -1.22 ± 0.06, -0.95 ± 0.20, and -1.85 ± 0.53 for the Ophiuchus, Taurus, Perseus, and Orion starless CMFs, respectively. We were unable to calculate a best-fit slope for Serpens due to the small sample size. Serpens aside, our starless CMFs showed similar log-normal shapes, though the range of masses and peak in the distribution varied with each cloud. The starless CMF for Orion also included an unusual population increase at very high masses, which could be attributed to its cores having a more varied temperature than assumed.

Our protostellar CMFs do not have the same log-normal shape and assuming the same dust temperature as the starless cores, the protostellar CMFs are systematically shifted to slightly higher masses. We increased the protostellar core temperatures to fit the width and peak of the protostellar CMFs with their starless CMFs. We found that protostellar core temperatures should increase by a factor of 1.3 in Ophiuchus, Taurus, and Perseus, a factor of ~ 4 in Serpens, and a factor of ~ 2 in Orion over our original dust temperatures. Though these increases are plausible, radiative transfer modeling of protostellar cores is necessary to determine if protostellar heating has such a significant impact on the average core temperature. With these new temperatures, we found that there was no overabundance of high-mass protostellar cores over low-mass cores. As well, we tested our classification scheme against two others (the Jørgensen and Enoch methods) and found that the fraction of high-mass cores identified as protostellar depended on the technique used for classification. Thus, we cannot conclude that high-mass cores evolve more quickly than lower mass cores.

We also examined trends in the starless CMF peak masses or best-fit slopes with cloud properties. Our five clouds represent a variety of environments and distances. We found a potential relationship between best-fit slope and core temperature, suggesting that a single power-law relationship for CMFs is not ideal. As well, we found a weak trend between CMF peak mass and cloud distance, which could be related to our sensitivity cut. We also found an unusual relationship between best-fit slope and number of cores in the sample, where the uncertainties in the slope increase with the sample size. Most of our trends, however, yielded no obvious correlations.

Finally, we used simple assumptions to predict the core populations for the unobserved regions of each cloud. We developed two sets of predicted CMFs, one which assumes that core incidence depends somewhat on A_V (A_V-dependent) and one which assumes that core incidence is independent of A_V (A_V-independent). We generated new predicted CMFs using the scaled histograms and Gaussian replacements at each mass bin. We found that the A_V-dependent slopes were typically steeper than the A_V-independent slopes, though comparisons between best-fit slopes from the histograms or Gaussian replacements were generally inconsistent. For both the A_V-dependent and A_V-independent assumptions, there was substantial increase in the number of cores for all clouds. We hope to compare our predictions to future surveys of entire cloud regions.

Bibliography

Allen, L. E., Calvet, N., D'Alessio, P., Merin, B., Hartmann, L., Megeath, S. T., Gutermuth, R. A., Muzerolle, J., Pipher, J. L., Myers, P. C., and Fazio, G. G.: 2004, *ApJS* **154**, 363

André, P. and Saraceno, P.: 2005, in A. Wilson (ed.), *ESA Special Publication*, Vol. 577 of *ESA Special Publication*, pp 179–184

André, P., Ward-Thompson, D., and Barsony, M.: 2000, *Protostars and Planets IV* pp 59–96

Bok, B. J. and Cordwell, C. S.: 1973, in M. A. Gordon and L. E. Snyder (eds.), *Molecules in the Galactic Environment*, pp 54–92

Bonnell, I. A., Vine, S. G., and Bate, M. R.: 2004, *MNRAS* **349**, 735

Burkert, A. and Alves, J.: 2009, *ApJ* **695**, 1308

Cambrésy, L., Beichman, C. A., Jarrett, T. H., and Cutri, R. M.: 2002, *AJ* **123**, 2559

Cesaroni, R., Churchwell, E., Hofner, P., Walmsley, C. M., and Kurtz, S.: 1994, *A&A* **288**, 903

Chabrier, G.: 2003, *PASP* **115**, 763

de Geus, E. J., Bronfman, L., and Thaddeus, P.: 1990, *A&A* **231**, 137

Di Francesco, J., Evans, II, N. J., Caselli, P., Myers, P. C., Shirley, Y., Aikawa, Y., and Tafalla, M.: 2007, in B. Reipurth, D. Jewitt, and K. Keil (eds.), *Protostars and Planets V*, pp 17–32

Di Francesco, J., Johnstone, D., Kirk, H., MacKenzie, T., and Ledwosinska, E.: 2008, *ApJS* **175**, 277

Dobbs, C. L., Bonnell, I. A., and Clark, P. C.: 2005, *MNRAS* **360**, 2

Elmegreen, B. G.: 2002, *ApJ* **577**, 206

Enoch, M. L., Evans, II, N. J., Sargent, A. I., and Glenn, J.: 2009, *ApJ* **692**, 973

Enoch, M. L., Evans, II, N. J., Sargent, A. I., Glenn, J., Rosolowsky, E., and Myers, P.: 2008, *ApJ* **684**, 1240

Evans, II, N. J., Allen, L. E., Blake, G. A., Boogert, A. C. A., Bourke, T., Harvey, P. M., Kessler, J. E., Koerner, D. W., Lee, C. W., Mundy, L. G., Myers, P. C., Padgett, D. L., Pontoppidan, K., Sargent, A. I., Stapelfeldt, K. R., van Dishoeck, E. F., Young, C. H., and Young, K. E.: 2003, *PASP* **115**, 965

Evans, II, N. J., Dunham, M. M., Jørgensen, J. K., Enoch, M. L., Merín, B., van Dishoeck, E. F., Alcalá, J. M., Myers, P. C., Stapelfeldt, K. R., Huard, T. L., Allen, L. E., Harvey, P. M., van Kempen, T., Blake, G. A., Koerner, D. W., Mundy, L. G., Padgett, D. L., and Sargent, A. I.: 2009, *ApJS* **181**, 321

Evans, II, N. J., Rawlings, J. M. C., Shirley, Y. L., and Mundy, L. G.: 2001, *ApJ* **557**, 193

Friesen, R. K., Di Francesco, J., Shirley, Y. L., and Myers, P. C.: 2009, *ApJ* **697**, 1457

Froebrich, D.: 2005, *ApJS* **156**, 169

Goldsmith, P. F.: 2001, *ApJ* **557**, 736

Goldsmith, P. F., Heyer, M., Narayanan, G., Snell, R., Li, D., and Brunt, C.: 2008, *ApJ* **680**, 428

Gould, B. A.: 1879, *Resultados del Observatorio Nacional Argentino* 1

Gutermuth, R. A., Myers, P. C., Megeath, S. T., Allen, L. E., Pipher, J. L., Muzerolle, J., Porras, A., Winston, E., and Fazio, G.: 2008, *ApJ* **674**, 336

Hartmann, L.: 2000, in F. Favata, A. Kaas, and A. Wilson (eds.), *Star Formation from the Small to the Large Scale*, Vol. 445 of *ESA Special Publication*, pp 107–116

Harvey, P., Merín, B., Huard, T. L., Rebull, L. M., Chapman, N., Evans, II, N. J., and Myers, P. C.: 2007, *ApJ* **663**, 1149

Harvey, P. M., Chapman, N., Lai, S.-P., Evans, II, N. J., Allen, L. E., Jørgensen, J. K., Mundy, L. G., Huard, T. L., Porras, A., Cieza, L., Myers, P. C., Merín, B., van Dishoeck, E. F., Young, K. E., Spiesman, W., Blake, G. A., Koerner, D. W., Padgett, D. L., Sargent, A. I., and Stapelfeldt, K. R.: 2006, *ApJ* **644**, 307

Hatchell, J. and Dunham, M. M.: 2009, *A&A* **502**, 139

Hatchell, J., Fuller, G. A., Richer, J. S., Harries, T. J., and Ladd, E. F.: 2007, *A&A* **468**, 1009

Hatchell, J., Richer, J. S., Fuller, G. A., Qualtrough, C. J., Ladd, E. F., and Chandler, C. J.: 2005, *A&A* **440**, 151

Henning, T., Michel, B., and Stognienko, R.: 1995, *Planet. Space Sci.* **43**, 1333

Herschel, J. F. W. S.: 1847, *Results of astronomical observations made during the years 1834, 5, 6, 7, 8, at the Cape of Good Hope; being the completion of a telescopic survey of the whole surface of the visible heavens, commenced in 1825*, London, Smith, Elder and co.

Holland, W., MacIntosh, M., Fairley, A., Kelly, D., Montgomery, D., Gostick, D., Atad-Ettedgui, E., Ellis, M., Robson, I., Hollister, M., Woodcraft, A., Ade, P., Walker, I., Irwin, K., Hilton, G., Duncan, W., Reintsema, C., Walton, A., Parkes, W., Dunare, C., Fich, M., Kycia, J., Halpern, M., Scott, D., Gibb, A., Molnar, J., Chapin, E., Bintley, D., Craig, S., Chylek, T., Jenness, T., Economou, F., and Davis, G.: 2006, in *Society of Photo-Optical Instrumentation Engineers (SPIE) Conference Series*, Vol. 6275 of *Society of Photo-Optical Instrumentation Engineers (SPIE) Conference Series*

Isobe, T., Feigelson, E. D., Akritas, M. G., and Babu, G. J.: 1990, *ApJ* **364**, 104

Johnstone, D., Di Francesco, J., and Kirk, H.: 2004, *ApJ* **611**, L45

Johnstone, D., Fich, M., Mitchell, G. F., and Moriarty-Schieven, G.: 2001, *ApJ* **559**, 307

Johnstone, D., Wilson, C. D., Moriarty-Schieven, G., Joncas, G., Smith, G., Gregersen, E., and Fich, M.: 2000, *ApJ* **545**, 327

Jørgensen, J. K., Harvey, P. M., Evans, II, N. J., Huard, T. L., Allen, L. E., Porras, A., Blake, G. A., Bourke, T. L., Chapman, N., Cieza, L., Koerner, D. W., Lai, S.-P., Mundy, L. G., Myers, P. C., Padgett, D. L., Rebull, L., Sargent, A. I., Spiesman, W., Stapelfeldt, K. R., van Dishoeck, E. F., Wahhaj, Z., and Young, K. E.: 2006, *ApJ* **645**, 1246

Jørgensen, J. K., Johnstone, D., Kirk, H., and Myers, P. C.: 2007, *ApJ* **656**, 293

Jørgensen, J. K., Johnstone, D., Kirk, H., Myers, P. C., Allen, L. E., and Shirley, Y. L.: 2008, *ApJ* **683**, 822

Kirk, H., Johnstone, D., and Di Francesco, J.: 2006, *ApJ* **646**, 1009

Kirk, H., Johnstone, D., and Tafalla, M.: 2007, *ApJ* **668**, 1042

Kirk, J. M., Ward-Thompson, D., Di Francesco, J., Bourke, T. L., Evans, II, N. J., Merín, B., Allen, L. E., Cieza, L. A., Dunham, M. H., Harvey, P., Huard, T., Jørgensen, J. K., Miller, J. F., Noriega-Crespo, A., Peterson, D., Ray, T. P., and Rebull, L. M.: 2009, *ArXiv astro-ph/0903.4063*

Knee, L. B. G. and Sandell, G.: 2000, *A&A* **361**, 671

Kroupa, P.: 2002, *Science* **295**, 82

Kurtz, S., Cesaroni, R., Churchwell, E., Hofner, P., and Walmsley, C. M.: 2000, *Protostars and Planets IV* pp 299–326

Lada, C. J., Lada, E. A., Clemens, D. P., and Bally, J.: 1994, *ApJ* **429**, 694

Lada, C. J. and Wilking, B. A.: 1984, *ApJ* **287**, 610

Lombardi, M. and Alves, J.: 2001, *A&A* **377**, 1023

Lombardi, M., Alves, J., and Lada, C. J.: 2006, *A&A* **454**, 781

Maddalena, R. J., Morris, M., Moscowitz, J., and Thaddeus, P.: 1986, *ApJ* **303**, 375

Megeath, S. T., Allgaier, E., Young, E., Allen, T., Pipher, J. L., and Wilson, T. L.: 2009, *AJ* **137**, 4072

Miller, G. E. and Scalo, J. M.: 1979, *ApJS* **41**, 513

Motte, F., Andre, P., and Neri, R.: 1998, *A&A* **336**, 150

Myers, P. C.: 2008, *ApJ* **687**, 340

Nishiyama, S., Tamura, M., Hatano, H., Kato, D., Tanabé, T., Sugitani, K., and Nagata, T.: 2009, *ApJ* **696**, 1407

Nutter, D., Kirk, J. M., Stamatellos, D., and Ward-Thompson, D.: 2008, *MNRAS* **384**, 755

Nutter, D. and Ward-Thompson, D.: 2007, *MNRAS* **374**, 1413

Offner, S. S. R., Klein, R. I., McKee, C. F., and Krumholz, M. R.: 2009, *ArXiv astro-ph/0904.2004*

Padgett, D. L., Rebull, L. M., Stapelfeldt, K. R., Chapman, N. L., Lai, S.-P., Mundy, L. G., Evans, II, N. J., Brooke, T. Y., Cieza, L. A., Spiesman, W. J., Noriega-Crespo, A., McCabe, C.-E., Allen, L. E., Blake, G. A., Harvey, P. M., Huard, T. L., Jørgensen, J. K., Koerner, D. W., Myers, P. C., Sargent, A. I., Teuben, P., van Dishoeck, E. F., Wahhaj, Z., and Young, K. E.: 2008, *ApJ* **672**, 1013

Peterson, D. E. and Megeath, S. T.: 2008, *The Orion Molecular Cloud 2/3 and NGC 1977 Regions*, Handbook of Star Forming Regions, Volume I: The Northern Sky ASP Monograph Publications, Vol. 4. Edited by Bo Reipurth, p.590-620

Porras, A., Jørgensen, J. K., Allen, L. E., Evans, II, N. J., Bourke, T. L., Alcalá, J. M., Dunham, M. M., Blake, G. A., Chapman, N., Cieza, L., Harvey, P. M., Huard, T. L., Koerner, D. W., Mundy, L. G., Myers, P. C., Padgett, D. L., Sargent, A. I., Stapelfeldt, K. R., Teuben, P., van Dishoeck, E. F., Wahhaj, Z., and Young, K. E.: 2007, *ApJ* **656**, 493

Reach, W. T., Megeath, S. T., Cohen, M., Hora, J., Carey, S., Surace, J., Willner, S. P., Barmby, P., Wilson, G., Glaccum, W., Lowrance, P., Marengo, M., and Fazio, G. G.: 2005, *PASP* **117**, 978

Ridge, N. A., Di Francesco, J., Kirk, H., Li, D., Goodman, A. A., Alves, J. F., Arce, H. G., Borkin, M. A., Caselli, P., Foster, J. B., Heyer, M. H., Johnstone, D., Kosslyn, D. A., Lombardi, M., Pineda, J. E., Schnee, S. L., and Tafalla, M.: 2006, *AJ* **131**, 2921

Robin, A. C., Reylé, C., Derrière, S., and Picaud, S.: 2003, *A&A* **409**, 523

Rosolowsky, E. W., Pineda, J. E., Foster, J. B., Borkin, M. A., Kauffmann, J., Caselli, P., Myers, P. C., and Goodman, A. A.: 2008, *ApJS* **175**, 509

Salpeter, E. E.: 1955, *ApJ* **121**, 161

Schnee, S. L., Ridge, N. A., Goodman, A. A., and Li, J. G.: 2005, *ApJ* **634**, 442

Shu, F. H., Li, Z.-Y., and Allen, A.: 2004, *ApJ* **601**, 930

Stahler, S. W. and Palla, F.: 2005, *The Formation of Stars*, by Steven W. Stahler, Francesco Palla, pp. 865. ISBN 3-527-40559-3. Wiley-VCH , January 2005.

Swift, J. J. and Williams, J. P.: 2008, *ApJ* **679**, 552

Tatematsu, K., Kandori, R., Umemoto, T., and Sekimoto, Y.: 2008, *PASJ* **60**, 407

Tatematsu, K., Umemoto, T., Kandori, R., and Sekimoto, Y.: 2004, *ApJ* **606**, 333

Ungerechts, H. and Thaddeus, P.: 1987, *ApJS* **63**, 645

Ward-Thompson, D., André, P., Crutcher, R., Johnstone, D., Onishi, T., and Wilson, C.: 2007a, in B. Reipurth, D. Jewitt, and K. Keil (eds.), *Protostars and Planets V*, pp 33–46

Ward-Thompson, D., Di Francesco, J., Hatchell, J., Hogerheijde, M. R., Nutter, D., Bastien, P., Basu, S., Bonnell, I., Bowey, J., Brunt, C., Buckle, J., Butner, H., Cavanagh, B., Chrysostomou, A., Curtis, E., Davis, C. J., Dent, W. R. F., van Dishoeck, E., Edmunds, M. G., Fich, M., Fiege, J., Fissel, L., Friberg, P., Friesen, R., Frieswijk, W., Fuller, G. A., Gosling, A., Graves, S., Greaves, J. S., Helmich, F., Hills, R. E., Holland, W. S., Houde, M., Jayawardhana, R., Johnstone, D., Joncas, G., Kirk, H., Kirk, J. M., Knee, L. B. G., Matthews, B., Matthews, H., Matzner, C., Moriarty-Schieven, G. H., Naylor, D., Padman, R., Plume, R., Rawlings, J. M. C., Redman, R. O., Reid, M., Richer, J. S., Shipman, R., Simpson, R. J., Spaans, M., Stamatellos, D., Tsamis, Y. G., Viti, S., Weferling, B., White, G. J., Whitworth, A. P., Wouterloot, J., Yates, J., and Zhu, M.: 2007b, *PASP* **119**, 855

Warner, B.: 1961, *PASP* **73**, 439

White, G. J., Casali, M. M., and Eiroa, C.: 1995, *A&A* **298**, 594

White, R. J., Greene, T. P., Doppmann, G. W., Covey, K. R., and Hillenbrand, L. A.: 2007, in B. Reipurth, D. Jewitt, and K. Keil (eds.), *Protostars and Planets V*, pp 117–132

Williams, J. P., Blitz, L., and McKee, C. F.: 2000, *Protostars and Planets IV* pp 97–120

Williams, J. P., de Geus, E. J., and Blitz, L.: 1994, *ApJ* **428**, 693

Williams, J. P. and Myers, P. C.: 1999, *ApJ* **518**, L37

Young, C. H., Jørgensen, J. K., Shirley, Y. L., Kauffmann, J., Huard, T., Lai, S.-P., Lee, C. W., Crapsi, A., Bourke, T. L., Dullemond, C. P., Brooke, T. Y., Porras, A., Spiesman, W., Allen, L. E., Blake, G. A., Evans, II, N. J., Harvey, P. M., Koerner, D. W., Mundy, L. G., Myers, P. C., Padgett, D. L., Sargent, A. I., Stapelfeldt, K. R., van Dishoeck, E. F., Bertoldi, F., Chapman, N., Cieza, L., DeVries, C. H., Ridge, N. A., and Wahhaj, Z.: 2004, *ApJS* **154**, 396

Young, K. E., Harvey, P. M., Brooke, T. Y., Chapman, N., Kauffmann, J., Bertoldi, F., Lai, S.-P., Alcalá, J., Bourke, T. L., Spiesman, W., Allen, L. E., Blake, G. A., Evans, II, N. J., Koerner, D. W., Mundy, L. G., Myers, P. C., Padgett, D. L., Salinas, A., Sargent, A. I., Stapelfeldt, K. R., Teuben, P., van Dishoeck, E. F., and Wahhaj, Z.: 2005, *ApJ* **628**, 283